1982

An NMR study of hydrogen diffusion in metal hydrides containing paramagnetic impurities

Tan-Tee Phua
Iowa State University

INFORMATION TO USERS

This reproduction was made from a copy of a document sent to us for microfilming. While the most advanced technology has been used to photograph and reproduce this document, the quality of the reproduction is heavily dependent upon the quality of the material submitted.

The following explanation of techniques is provided to help clarify markings or notations which may appear on this reproduction.

1. The sign or "target" for pages apparently lacking from the document photographed is "Missing Page(s)". If it was possible to obtain the missing page(s) or section, they are spliced into the film along with adjacent pages. This may have necessitated cutting through an image and duplicating adjacent pages to assure complete continuity.

2. When an image on the film is obliterated with a round black mark, it is an indication of either blurred copy because of movement during exposure, duplicate copy, or copyrighted materials that should not have been filmed. For blurred pages, a good image of the page can be found in the adjacent frame. If copyrighted materials were deleted, a target note will appear listing the pages in the adjacent frame.

3. When a map, drawing or chart, etc., is part of the material being photographed, a definite method of "sectioning" the material has been followed. It is customary to begin filming at the upper left hand corner of a large sheet and to continue from left to right in equal sections with small overlaps. If necessary, sectioning is continued again–beginning below the first row and continuing on until complete.

4. For illustrations that cannot be satisfactorily reproduced by xerographic means, photographic prints can be purchased at additional cost and inserted into your xerographic copy. These prints are available upon request from the Dissertations Customer Services Department.

5. Some pages in any document may have indistinct print. In all cases the best available copy has been filmed.

University Microfilms International
300 N. Zeeb Road
Ann Arbor, MI 48106

Phua, Tan-Tee

AN NMR STUDY OF HYDROGEN DIFFUSION IN METAL HYDRIDES CONTAINING PARAMAGNETIC IMPURITIES

Iowa State University PH.D. 1982

An NMR study of hydrogen diffusion in metal hydrides containing paramagnetic impurities

by

Tan-Tee Phua

A Dissertation Submitted to the
Graduate Faculty in Partial Fulfillment of the
Requirements for the Degree of
DOCTOR OF PHILOSOPHY

Department: Physics
Major: Solid State Physics

Approved:

Signature was redacted for privacy.

In Charge of Major Work

Signature was redacted for privacy.

For the Major Department

Signature was redacted for privacy.

For the Graduate College

Iowa State University
Ames, Iowa

1982

TABLE OF CONTENTS

I. INTRODUCTION

Combinations of hydrogen with metals have provided a widely divergent group of materials that have, both from purely scientific and technological points of view, very interesting and rewarding properties. The embrittlement that is caused by the introduction of hydrogen into the interstitial sites of host materials poses a well-known problem in the construction industry. It creates difficulties and problems in aircraft, steel industry, and reactor vessel wall construction.

On the other side of the coin, metal-hydrogen systems, practically, do have many important applications (1,2,3,4). The possibilities which hydrogen technology offers in connection with hydrogen storage using hydrides are in:

a. thermal engineering,

b. the reactor industry, and

c. the power generating and transmitting industry.

In order to push the level of understanding of the problems caused by metal-hydrogen systems further and to expand the usefulness of these systems in the industrial area, much greater effort needs to be applied to the study of the internal hydrogen motion (diffusion), the structures and phase transitions of the hydrogen sub-lattice, and the electronic properties of metal-hydrogen systems.

A few established facts about Nuclear Magnetic Resonance which show this to be an especially appropriate method for the study of metal hydrides are:

a. samples need not be single phase in the metallurgical sense;

b. samples can be in powder form; single crystals are not required;

c. investigations can be made over a wide temperature range;

d. information on crystal structure, electronic structure, atom locations, and property changes at phase transitions can be obtained.

Among the essential desirable characteristics of hydrogen-storing metal hydrides are fast hydrogen absorption and desorption kinetics. The diffusion of hydrogen within the metallic lattice is one of the principal factors that determines these two properties. The Nuclear Magnetic Resonance (NMR) technique has been used for many years to investigate hydrogen motion and locations in metal-hydrogen systems, as has recently been reviewed by Barnes (5) and Cotts (6,7,8). NMR is an effective technique for obtaining information about hydrogen motion since it is sensitive to the atomic diffusion via the effects which such motion has on the spin relaxation rates. The spin relaxation rates are functions of the power spectra of the randomly varying dipolar fields resulting from the atomic diffusive jumps and depend on the strength of the dipolar interaction between protons and on the diffusive jump frequency. Hence, measurements of the proton spin-lattice relaxation time T_1 can be used to determine the temperature dependence of the hydrogen jump frequency and the associated activation energy.

In most cases, the spin-lattice relaxation time is measured as a function of temperature. A traditional plot of proton spin-lattice relaxation in a metal hydride is shown in Figure 1-1. The measured spin relaxation rate $(T_1)^{-1}$ is the sum of the diffusion controlled rate $(T_{1d})^{-1}$, the conduction electron contribution $(T_{1e})^{-1}$ which dominates at low temperature, and a contribution from paramagnetic impurity ions $(T_{1p})^{-1}$ which may only be effective at low temperatures or over the entire temperature range, depending on the type of ions present in the sample. The net spin-lattice relaxation rate may be written as

$$(T_1)^{-1} = (T_{1d})^{-1} + (T_{1e})^{-1} + (T_{1p})^{-1}. \qquad (1\text{-}1)$$

Typically, for a "pure" hydride, the proton spin-lattice relaxation time as a function of inverse temperature passes through a minimum when the diffusion jump frequency equals (approximately) the nuclear Larmor precession frequency in the applied magnetic field. This procedure has been used to deduce the temperature dependence of the correlation time τ_C which is half the mean dwell time τ_D for proton-proton interactions. The correlation time τ_C is then fitted to an Arrhenius relation to deduce the activation energy E_{act}. If the paramagnetic impurity content is small enough, one can ignore the impurity contribution to the nuclear relaxation rate and make use of the low temperature relaxation rates to estimate the electronic density of states at the Fermi level which is proportional to the inverse square-root of the Korringa product, $T_{1e}T$.

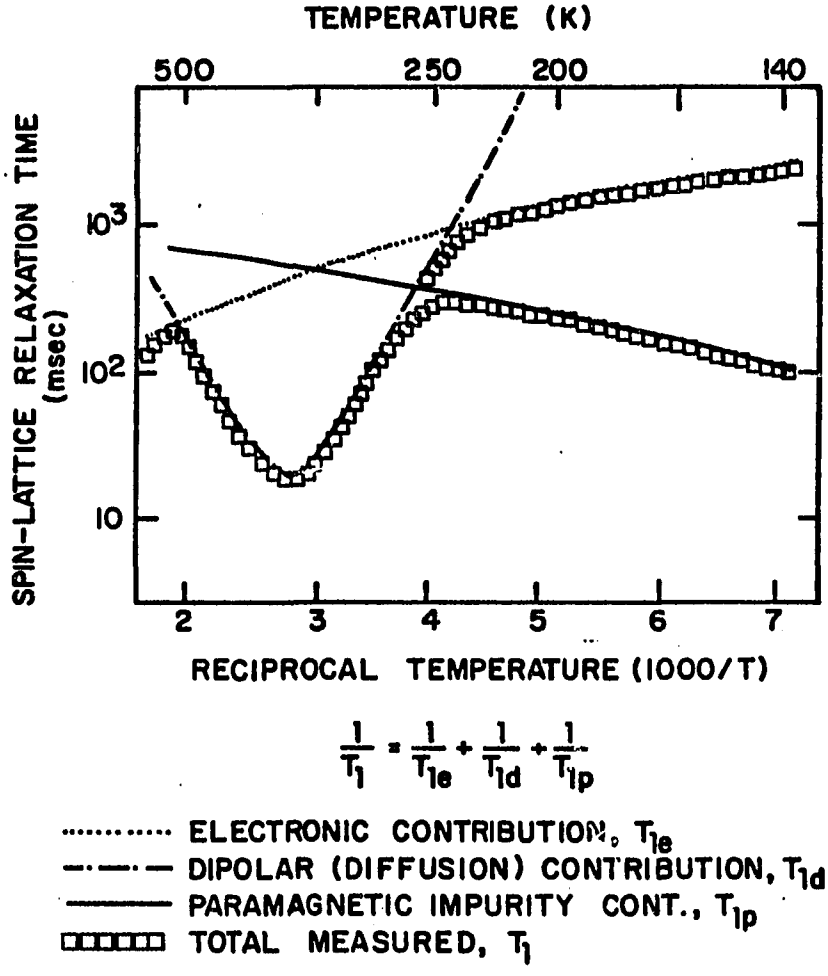

Figure 1-1. Schematic plot of logarithm of proton spin-lattice relaxation time T_1 versus reciprocal temperature in a typical transition metal hydride. The paramagnetic impurity contribution T_{1p} was traditionally assumed to be most effective at low temperatures and less effective at high temperatures. The upper (lower) □ curve for T < 250K represents the resultant relaxation time T_1 without (with) paramagnetic impurity.

For a "pure" metal hydride, $(T_1)^{-1} = (T_{1d})^{-1} + (T_{1e})^{-1}$. At low temperature, $(T_{1d})^{-1} << (T_{1e})^{-1}$, so that $T_1 = T_{1e}$. By using the Korringa relation, $T_{1e}T = K$, one can then deduce T_{1e} values at higher temperatures. Consequently, the diffusion relaxation rate $(T_{1d})^{-1}$ can be obtained by subtraction. Information regarding the activation energy, jump frequency, and diffusivity can then be extracted from the $(T_{1d})^{-1}$ values. If the assumption of the "pure" hydride is adopted before knowing the actual purity of the sample, one may run the risk of neglecting the existence of the impurity ions' contribution to the nuclear relaxation rate. That can lead to an incorrect estimation of the conduction electron contribution $(T_{1e})^{-1}$; hence, the values of the activation energy and jump frequency are also affected.

It is a well-known fact that paramagnetic impurity ions play an important role in the nuclear spin relaxation process in insulating solids (e.g., CaF_2) at concentrations as low as several hundred parts per million. Any excess energy in the nuclear spin system diffuses via the mutual spin-exchange process towards the large electronic magnetic moments of the impurity ions. However, no attempt had heretofore been made to study systematically the effects that paramagnetic impurities have on the proton spin-lattice relaxation rate in hydrides even though careful scrutiny of reported T_1 measurements suggests that significant effects may occur (see below).

There exist in the literature many examples of an asymmetric minimum in the proton spin-lattice relaxation time $T_1(T)$, with a

shallower low-temperature slope interpreted as indicating a change to a diffusion mechanism with a lower activation energy. In several cases, a discontinuous change in the activation energy E_{act} has been reported (9,10), as seen in Figures 1-2(a) and 1-2(b), often occurring on the low temperature side of the T_1 minimum. Figures 1-2(c) and 1-2(d) show an additional minimum (11), perhaps only partially resolved (12,13). These cases have been interpreted in terms of two coexisting but independent motions of the hydrogen. Korn and Zamir (14) had measured the proton spin-lattice relaxation time on a series of TiH_x samples as a function of temperature. They reported that significant double-minimum character was not observed. However, a very weak irregularity in the data, which could possibly indicate a small secondary minimum, was detected. The double-minimum phenomenon was observed for an oxidized $TiH_{1.70}$ sample.

All these different observations have prompted theorists to develop more sophisticated relaxation models to match the experimental observations and to interpret the detailed $T_1(T)$ data in terms of different diffusion mechanisms. Several attempts have been made to explain the difference in apparent activation energies on the high and low temperature sides of the T_1 minimum, as well as the discontinuous change of activation energy sometimes found on the low temperature side of the minimum. These attempts include improvement in the basic theory of relaxation by lattice diffusion (15,16) on the one hand, and hypotheses concerning changes in diffusion mechanisms (17). Confusion and some loss of confidence in the NMR method have also resulted from these observations.

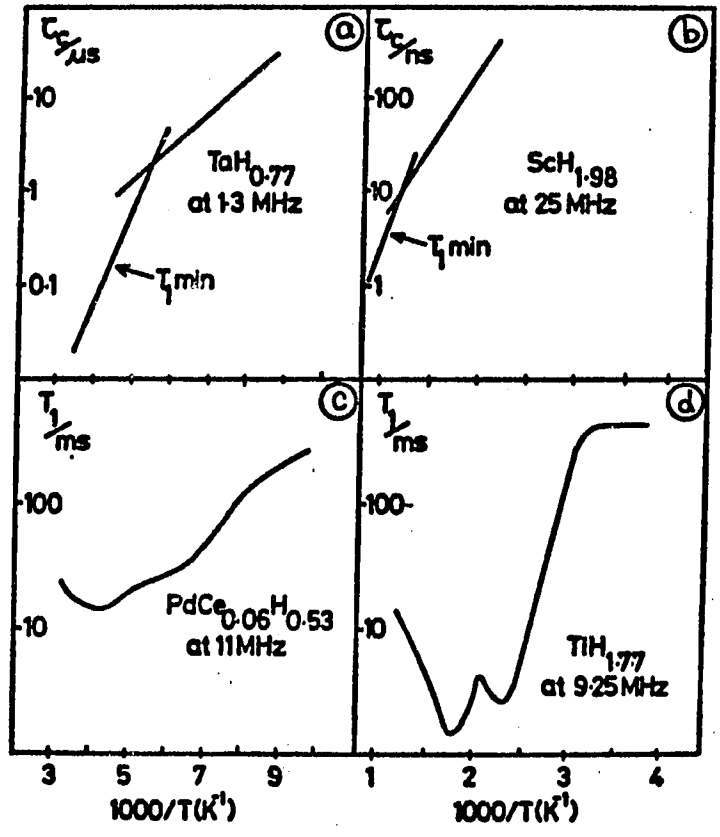

Figure 1-2. Variations of correlation time τ_c and proton spin-lattice relaxation time T_1 with temperature in some metal hydrides. (a) and (b) are taken from references (9) and (10), respectively; both show discontinuous changes in activation energy. (c) and (d) are taken from references (18) and (11), respectively; secondary minima are clearly shown

No explanation was provided by Korn for the disappearance of the double minimum. However, by comparing Torrey's and Korn's results, the spin-lattice relaxation times in the low temperature region are seen to be much longer for the latter's, and the T_1 value increases as the temperature decreases. In contrast, Torrey's low temperature T_1 values are shorter than Korn's and flatten out and become temperature independent. These observations indicate that Korn had much purer samples than Torrey. Korn's observation on the oxidized $TiH_{1.70}$ sample also supports this view. The above short discussion leads us to the speculation that slope changes and double-minima behavior may instead be due to the interaction of the mobile protons with small amounts of paramagnetic impurity ions present in the host metal.

As a consequence, existing NMR data for many metal-hydrogen systems may require reinterpretation. However, the levels of residual impurities in the specimens were generally unknown; a complete and satisfactory interpretation is impossible to achieve at this time. This study, therefore, has embarked on an entirely new series of measurements on a few hydride systems using starting materials of controlled impurity content and type of impurity.

In this investigation, the two major hydride systems that have been studied are those of yttrium and lanthanum. Both yttrium and lanthanum metals react with hydrogen to form nonstoichiometric hydrides with a maximum hydrogen-to-metal ratio of three. The β-phase lanthanum hydride, LaH_x, exists from $x \geq 1.8$ to $x = 3$ and has the fcc (CaF_2)

structure shown in Figure 1-3. But for yttrium hydride, YH_x, the β-phase exists only over the approximate composition range $1.8 \leq x \leq 2.05$ in the temperature range of interest (77K to 800K), as seen in Figure 1-4. At lower hydrogen concentrations, $x \leq 1.80$, co-existence of the α and β-phases occurs for both of these hydrides. At the other extreme, the structure of yttrium hydride changes from cubic (CaF_2) to hexagonal (HoD_3) as the trihydride composition is approached. Both the cubic and hexagonal phases exist in the region from $x \geq 2.05$ to $x \leq 2.80$. The hexagonal trihydride phase probably occurs as a single phase at concentrations $x \geq 2.80$. Both yttrium and lanthanum hydrides studied in this investigation are in the cubic phase (CaF_2 structure) with the metal atoms located on an fcc lattice. Hydrogen occupies predominantly the interstitial sites with tetrahedral symmetry (T-sites). A second type of interstitial site exists with octahedral symmetry (O-sites), but the tetrahedral site lies lower in energy and, consequently, is preferentially filled. However, premature occupancy of octahedral interstitial sites before the tetrahedral sites were totally filled had been detected by NMR (19) and neutron scattering (20) techniques for the yttrium dihydrides.

The main objective of this investigation has been to study the effects of the presence of paramagnetic impurities in the yttrium and lanthanum dihydrides. These dihydrides were doped with different types of rare-earth impurity (Ce, Nd, Gd, Dy, Er) and at various concentrations.

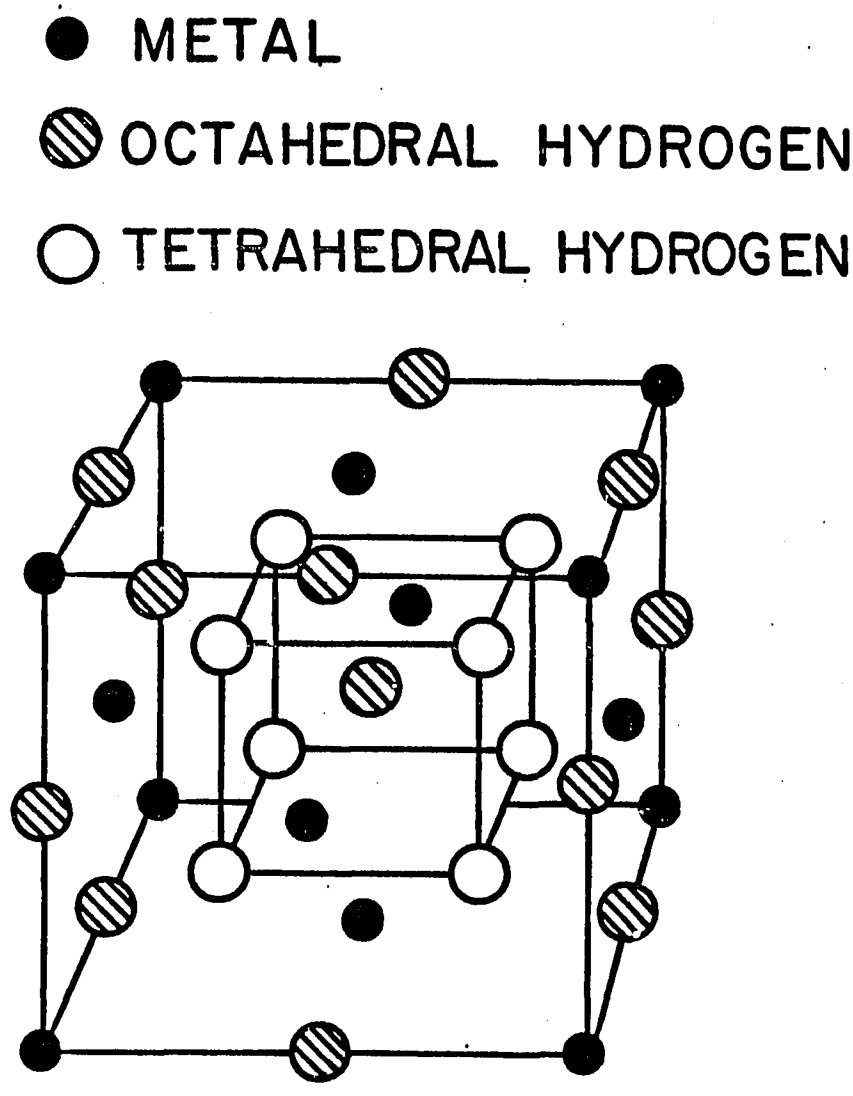

Figure 1-3. The conventional fcc unit cell shows the positions of host metal (La or Y) atoms and tetrahedral (T) and octahedral (O) hydrogen sites. The tetrahedral hydrogen is located at the center of a tetrahedron formed by its four nearest host atoms. Octahedral sites have six neighbor host atoms forming a regular octahedron. There are two T-sites and one O-site for each host atom

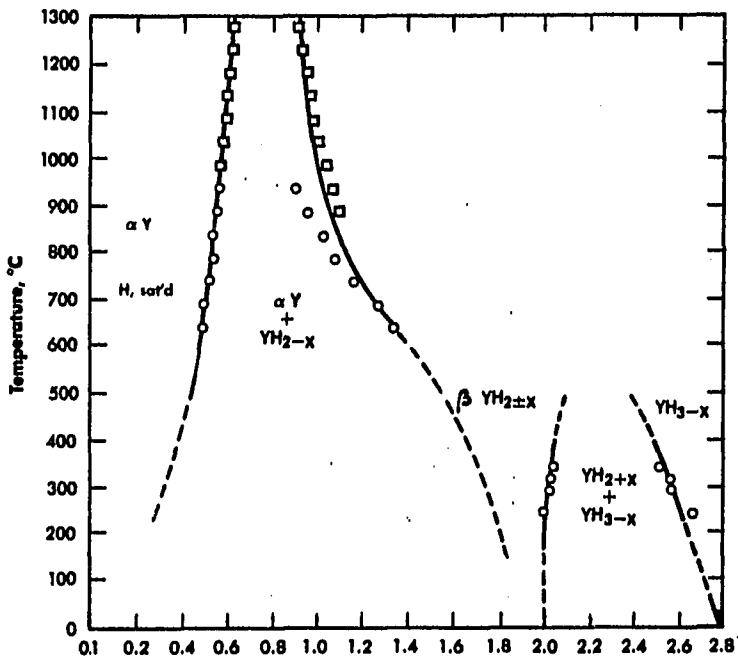

Figure 1-4. Phase diagram of the yttrium-hydrogen system (after Mueller et al., (18))

Samples included in this study are tabulated in Tables 1-1 and 1-2. The spark source mass spectrometric analyses for various batches of yttrium and lanthanum metals used for making the hydrides are included in the Appendix.

A brief review of the theoretical background of the various relaxation mechanisms, including the newly recognized effects that paramagnetic impurities can have in metal hydrides, is given in Chapter II. A short description of the apparatus used in this project and of sample preparation methods is presented in Chapter III. Chapter IV describes the experimental method used, and the results and interpretation of the experimental data are presented in the following chapter.

Table 1-1. Lanthanum hydrides, $La_{1-y}(RE)_yH_x$, investigated in this study, showing the type and concentration (in ppm) of RE dopant

X = H/La	Impurity	Concentration of dopant, y, in ppm	La-metal used (Ames Laboratory)
1.80	RE's[a]	2[b]	La-112078
2.00	Mainly Gd[a]	7[b]	La-8679
2.15	RE's[a]	2[b]	La-102877
2.27	RE's[a]	2[b]	La-102877
2.38	Mainly Gd[a]	7[b]	La-8679
2.46	RE's[a]	2[b]	La-102877
2.26	Mainly Fe, Gd, Ce[a]	80Fe, 15Gd, 10Ce[b]	La-72280
2.25	Ce	100	La-72280
2.25	Ce	198	La-72280
2.25	Ce	481	La-72280
2.25	Ce	908	La-72280
2.27	Mainly Ce[a]	4[b]	La-8681
2.24	Gd	50	La-8681
2.26	Gd	100	La-8681
2.25	Gd	200	La-8681
2.24	Gd	500	La-8681

[a]Concentration not controlled.

[b]Spark-source mass spectrometric determination.

Table 1-2. Yttrium hydrides, $Y_{1-y}(RE)_yH_x$, investigated in this study, showing the type and concentration (in ppm) of RE dopant

X = H/Y	Impurity	Concentration of dopant, y, in ppm	Y-metal used (Ames Laboratory)
1.81	Mainly Gd[a]	20[b]	Y-12979-W
1.91	Mainly Gd[a]	20[b]	Y-12979-W
1.98	Mainly Gd[a]	20[b]	Y-12979-W
2.03	Mainly Gd[a]	20[b]	Y-12979-W
1.98	Partly Gd[a]	2[b]	Y-12381B[c]
2.00	Gd	50	Y-12381B
1.98	Gd	100	Y-12381B
1.96	Gd	200	Y-12381B
1.99	Gd	475	Y-12381B
1.98	Gd	915	Y-12381B
2.01	Ce	98	Y-12381B
1.97	Ce	444	Y-12381B
1.97	Er	100	Y-12381B
1.95	Er	476	Y-12381B
1.99	Dy	100	Y-12381B
1.98	Dy	478	Y-12381B
2.02	Nd	100	Y-12381B
2.03	Nd	452	Y-12381B

[a]Concentration not controlled.

[b]Spark source mass spectroscopic determination.

[c]Y-12381B also contains 4 ppm Tb, 2 ppm Ce, 4 ppm Pr.

II. NUCLEAR SPIN-LATTICE RELAXATION

A. Origins of the Relaxation

Nuclear Magnetic Resonance is possible because many nuclei possess nonzero magnetic moments $\vec{\mu}$ and angular momenta $I\hbar$, where I is the spin of the nucleus and $\hbar$ is Planck's constant. The magnetic moment is proportional to the angular momentum, $\vec{\mu} = \gamma\vec{I}\hbar$, where γ is the gyromagnetic ratio. Nuclei interact with a static magnetic field $\vec{H}_0$ when it is turned on. Hence, the magnetic moment $\vec{\mu}$ will tend to line up along the applied field's direction, in a manner exactly similar to the lining up of a compass needle with the earth's magnetic field. Because of the presence of the angular momentum, the torque due to the field acting on the moment causes it to precess around the magnetic field with an angular frequency of precession (Larmor frequency) ω_0 proportional to the strength of the applied field H_0. This frequency is given by the relation, $\omega_0 = \gamma H_0$.

Classically, the equation of motion for a magnetic moment $\vec{\mu}$ in a magnetic field $\vec{H}_0$ follows from the change of angular momentum with respect to time,

$$\frac{d(\vec{I}\hbar)}{dt} = \vec{\mu} \times \vec{H}_0 \qquad (2\text{-}1)$$

This equation describes the precession of the spin around the field $\vec{H}_0$ under the influence of the torque, $\vec{\mu} \times \vec{H}_0$. Since the magnetic moment $\vec{\mu} = \gamma\hbar\vec{I}$, Equation (2-1) gives,

$$\frac{d\vec{\mu}}{dt} = \vec{\mu} \times \gamma\vec{H}_0. \tag{2-2}$$

For a system of spins, then,

$$\frac{\Sigma_i d\vec{\mu}_i}{dt} = \Sigma_i \vec{\mu}_i \times \gamma\vec{H}_0. \tag{2-3}$$

But the macroscopic magnetization $\vec{M}$ is defined as the vector sum of all magnetic moments $\vec{\mu}_i$,

$$\vec{M} = \Sigma_i \vec{\mu}_i. \tag{2-4}$$

Thus, the magnetization satisfies the same equation of motion as do the individual moments,

$$\frac{d\vec{M}}{dt} = \gamma\vec{M} \times \vec{H}_0. \tag{2-5}$$

Quantum mechanically, the orientation of a precessing magnetic moment with respect to the magnetic field is quantized, the number of allowed orientation being $2I + 1$. In this study, protons with spin $I = \frac{1}{2}$ are investigated, so the allowed orientations are only two, one "parallel" and the other "antiparallel" to the applied field $\vec{H}_0$.

It is well-known from introductory physics (21) that the energy of a magnetic moment $\vec{\mu}$ in a magnetic field $\vec{H}_0$ is $-\vec{\mu}\cdot\vec{H}_0$. Thus, a positive moment will always tend to align itself with the field to occupy the

lower energy state. Each of these magnetic moments can undergo a transition to the higher or the lower energy state by receiving or emitting an appropriate amount of energy, $\hbar\omega$, where ω is the angular frequency of an applied radiofrequency (rf) field. The transition will occur only when the frequency ω equals the Larmor frequency ω_0. Before the rf field is turned on, the population ratio of the two states depends on the sample's absolute temperature T and the strength of the field $\vec{H}_0$ by the Boltzmann factor $\exp(-\mu H_0/k_B T)$ where k_B is Boltzmann's constant. As a result, there will be more spins in the lower than in the higher energy state. The population difference between the lower and higher energy states gives rise to a net thermal equilibrium magnetization,

$$\vec{M}_0 = \frac{N\gamma^2\hbar I(I+1)}{3k_B T}\vec{H}_0, \qquad (2\text{-}6)$$

where N is the number of spins. Thus, for a sample in zero applied magnetic field, there should be no macroscopic magnetization, $M_0 \simeq 0$, since the earth's field is very weak in comparison to typical laboratory magnetic fields ($\sim$1T). When the static magnetic field $\vec{H}_0$ is turned on, the magnetization $\vec{M}$ grows exponentially towards the equilibrium value. At some characteristic time T_1, the magnetization will have grown to within a factor $(1-e^{-1})$ = 63% of the equilibrium value M_0. T_1 is called the spin-lattice relaxation time. The reason the magnetization grows exponentially and not instantaneously is governed by the principle of

energy conservation. When the magnetic field $\vec{H}_0$ is applied, the degeneracy is lifted and the energy between the higher and lower energy states becomes $2\mu H_0$. Initially, the nuclear moments will be equally distributed between the two states. The moments which are initially in the higher energy state have to surrender $2\mu H_0$ of energy in order to make the transition to the lower energy state in which the moments are parallel to the field. This excess energy has to be transferred to the other thermal energy reservoirs which are collectively called the lattice. This energy can be given up and transferred to the lattice by spontaneous or stimulated emission of a photon or by radiationless processes. The probability of spontaneous emission is directly proportional to the third power of the operating frequency. But at radiofrequencies, this is very small; thus, this probability is essentially negligible. So the transition between the two states is governed by stimulated emission and radiationless processes. Stimulated emission occurs when the spin experiences magnetic or electric fields fluctuating at its Larmor frequency. There are three main sources that cause these fields to fluctuate in solids.

1. Relaxation by unpaired electron spins and paramagnetic impurity ions. An unpaired electron has a magnetic moment which is about 2000 times larger than that of a proton. If it changes its orientation randomly, it will cause the magnetic field around the site to vary in time. If it is a conduction electron, the fluctuation arises from its translational motion.

2. Diffusion of the nuclear spin. When a nucleus moves randomly from one place to another, it experiences a changing local magnetic field due to other nuclei or unpaired electrons.
3. Presence of an electric field gradient (EFG). An electric field gradient can interact with the electric quadrupole moment of the nucleus if the spin of the nucleus $I > \frac{1}{2}$. Throughout this study, the proton is the only nuclear probe utilized. The proton has no electric quadrupole moment, so this mechanism is not relevant to the present work.

Before discussing the various spin relaxation mechanisms in the remainder of this chapter, an important function, the spectral density function, $J(\omega)$, will be introduced.

B. The Spectral Density Function $J(\omega)$

As a pair of spins, $\vec{\mu}_1$ and $\vec{\mu}_2$, are brought closer to one another from far apart to normal intermolecular distance, they will interact more strongly as they approach each other. The mutual energy of interaction Hamiltonian is

$$H_d = \frac{\vec{\mu}_1 \cdot \vec{\mu}_2}{r_{12}^3} - \frac{3(\vec{\mu}_1 \cdot \vec{r}_1)(\vec{\mu}_2 \cdot \vec{r}_2)}{r_{12}^5} \qquad (2\text{-}7)$$

where r_{12} is the distance between the spins, and $\vec{r}_1$ and $\vec{r}_2$ are the position vectors of the two spins. The interaction energy is constant for a particular atomic arrangement. Now, let these two spins move

randomly with respect to each other. The separation distance and position vectors will be functions of time, $\vec{r}(t)$, the interaction becomes time dependent, and the energy will no longer be constant. The frequency dependent power spectrum of this interaction is the spectral density function $J(\omega,\tau)$. The relaxation rate T_1^{-1} is directly related to the spectral density $J(\omega,\tau)$ evaluated at the Larmor precession frequency of the nucleus (and related frequencies, depending whether the spins are identical or different).

Since the atomic motions are not exactly random, and are extremely complicated, the spectral density appropriate to actual atomic motion has been determined in very few cases. If one assumes, however, that the atomic motion is completely random, then one can express the spectral density function $J(\omega,\tau)$ in terms of a correlation time τ_c which is the characteristic time of the exponentially decaying dipolar field correlation function defined by

$$G(t) = \langle h(t') \cdot h(t'+t) \rangle = G(0) \exp(-t/\tau_c) \qquad (2\text{-}8)$$

where $h(t')$ is a component of the local dipolar field. The correlation time τ_c is also a measure of the mean time between the individual events causing the field fluctuations, such as atomic diffusional jumps. In this case it can often be expressed as a function of temperature, such as,

$$\tau_c = \tau_0 \exp(E_{act}/k_B T), \qquad (2\text{-}9)$$

where τ_0 and E_{act} are constants.

Thus, in the case of completely random motion, the spectral density function $J(\omega,\tau_c)$ which is the Fourier transform of G(t) can be expressed as,

$$J(\omega,\tau_c) \propto \frac{\tau_c}{1+\omega^2\tau_c^2} \tag{2-10}$$

The value of $J(\omega,\tau_c)$ at small frequency ω is almost constant, and falls off as ω^{-2} for large ω. The area under the curve corresponds to the mean square interaction energy which is being modulated by the atomic motions and which is a constant (provided that, e.g., the type of site populated does not change). Thus,

$$\int_0^\infty J(\omega,\tau_c)d\omega = \text{constant}.$$

The spectral density $J(\omega, \tau_c)$ will be bunched at low frequencies at low temperature and spread-out over a larger frequency range at higher temperatures as a consequence of the temperature dependence of τ_c. But the area under it is always a constant even though the shape changes. If measurements are made at a fixed Larmor frequency ω_0, the spectral density $J(\omega_0, \tau_c)$ first increases as the temperature increases (see Figure 2-1). It will continue to increase to a maximum value (at $\tau_c \simeq \frac{1}{\omega_0}$) after which it decreases as the temperature increases further.

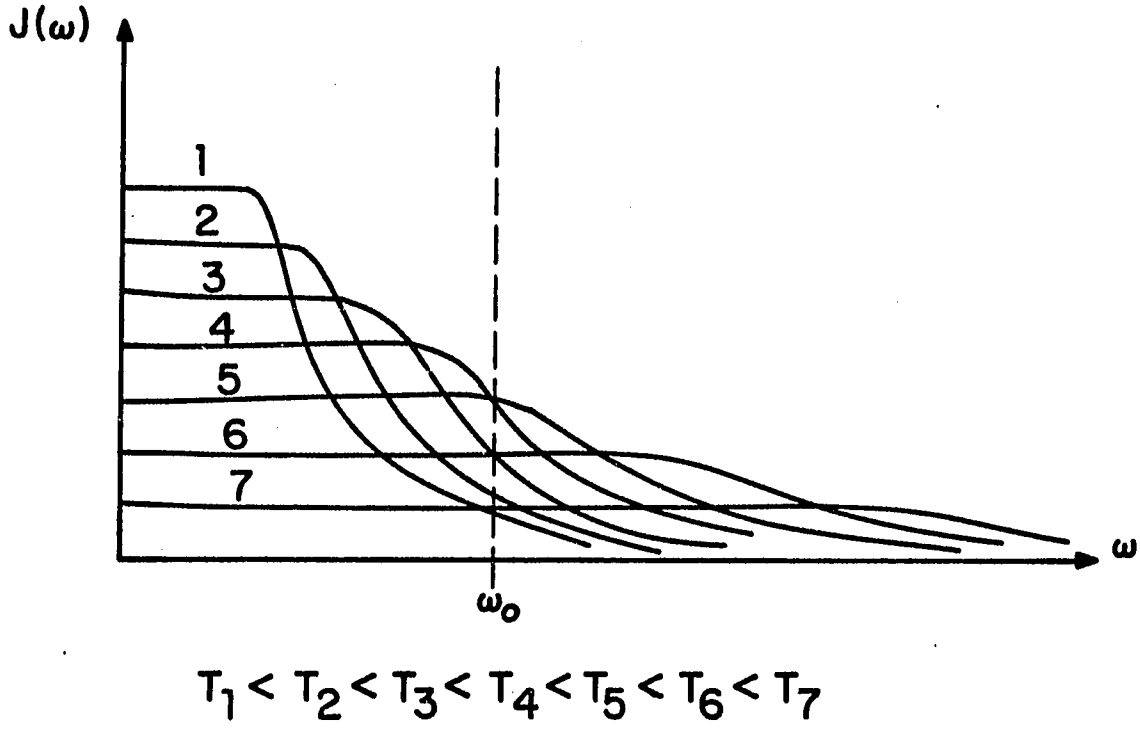

Figure 2-1. A composite plot of the spectral density function $J(\omega)$ versus frequency ω for various temperatures T. Curves 1 to 7 correspond to temperatures T_1 to T_7, respectively, the area under $J(\omega)$ is always a constant even though the shape changes. At a fixed Larmor frequency ω_0, the value of $J(\omega_0)$ first increases with increasing temperature, then decreases after a maximum is reached near $\tau_c = \frac{1}{\omega_0}$

C. Spin-lattice Relaxation Mechanisms

Several well-known texts are available which describe the various magnetic relaxation mechanisms in detail (22,23,24). Only the relaxation mechanisms important to this investigation are to be briefly described in the following subsections.

1. Relaxation due to atomic diffusion

Atomic diffusion can change the magnitude and orientation of the vector $\vec{r}_{ij}$ joining two nuclei and therefore modulate the dipolar interaction between them; in what follows it is assumed that the diffusional motion is random and isotropic. Hence, it will create a randomly time varying magnetic field at the site occupied by the nucleus in which one is interested. The transverse component of this fluctuating magnetic field at the nuclear precession frequency will be effective in causing spin transitions to occur. The random motion is related to an autocorrelation function G(t) which is a measure of the change in time of the magnitude and direction of the local field.

Let h(t') be a local field component at time t' and h(t'+t) that at some later time t'+t. Then the correlation function G(t) is defined as the average over all t' of the scalar product of those two local fields,

$$G(t) = \langle h(t') \cdot h(t'+t) \rangle .$$

As already mentioned, the autocorrelation function G(t) is related to the spectral density function $J(\omega, \tau_c)$ by a Fourier transformation. Therefore, the spectral density function $J(\omega, \tau_c)$ can be written as,

$$J^{(q)}(\omega) = \int_{-\infty}^{\infty} G^{(q)}(t)\exp(-i\omega t)dt, \tag{2-11}$$

where $$G^{(q)}(t) = \sum_j \langle F_{ij}{}^{(q)}(t')F_{ij}{}^{(q)*}(t'+t)\rangle, \tag{2-12}$$

$$F_{ij}{}^{(q)}(t) = \frac{d_q Y_{2,q}(\Omega_{ij})}{r_{ij}^3}, \tag{2-13}$$

$$d_0{}^2 = \frac{16\pi}{5}, \quad d_1{}^2 = \frac{8\pi}{15}, \quad d_2{}^2 = \frac{32\pi}{15}.$$

The local field components are closely related to the spatial part of the interaction Hamiltonian, Equation 2-7, represented by the functions $F_{ij}{}^{(q)}$. The summation adds the effects of all surrounding dipoles. The $Y_{2,q}$ are normalized spherical harmonics with coordinates $(\Theta, \phi)_{ij}$ made time dependent by the atomic diffusion. The simplest form of the $G^{(q)}(t)$ was suggested by Bloembergen, Purcell and Pound (BPP) (25). It is assumed that the magnetic field fluctuations due to the atomic motions are truly random. Then the dipolar field correlations decay exponentially as $\exp(-t/\tau_c)$. The BPP model then expresses,

$$G^{(q)}(t) = G^{(q)}(0)\ \exp(-t/\tau_c),$$

for any solid or liquid. The spectral density functions become,

$$J^{(q)}(\omega, \tau_c) = G^{(q)}(0) \cdot \frac{2\tau_c}{1+\omega^2\tau_c^2}\ .$$

By averaging $G^{(q)}(0)$ over all crystal orientations, one obtains for powder samples

$$G^{(0)}(0) : G^{(1)}(0) : G^{(2)}(0) = 6 : 1 : 4$$

Thus, the spectral density functions corresponding to no spin flip, one spin flip and two spin flips, $J^{(0)}(\omega, \tau_c)$, $J^{(1)}(\omega, \tau_c)$ and $J^{(2)}(\omega, \tau_c)$, respectively, are as follows,

$$J^{(0)}(\omega, \tau_c) = \frac{24}{15}\sum_j r_j^{-6}\left(\frac{\tau_c}{1+\omega^2\tau_c^2}\right) \qquad (2\text{-}14)$$

$$J^{(1)}(\omega, \tau_c) = \frac{1}{6}J^{(0)}(\omega, \tau_c) \qquad (2\text{-}15)$$

$$J^{(2)}(\omega, \tau_c) = \frac{2}{3}J^{(0)}(\omega, \tau_c) \qquad (2\text{-}16)$$

where r_j is the separation between interacting dipoles. If only a fraction of the available sites is randomly occupied, the required sum over r_j^{-6} is equal to that fraction times the sum over all available sites. For a polycrystalline sample containing only like nuclei of any spin I, the BPP model gives (23),

$$T_{1d}^{-1} = \frac{2}{3}\gamma^4\hbar^2 I(I+1)\ [J^{(1)}(\omega_0, \tau_c) + J^{(2)}(2\omega_0, \tau_c)]. \qquad (2\text{-}17)$$

Since this relaxation is caused by the atomic motion which in turn causes the local magnetic field to vary in time, much information regarding the atomic motion can be obtained from the measured relaxation time, i.e., the atomic jumping frequency, the activation energy for diffusion, the diffusion coefficient, and in some cases the actual jump distance.

2. Conduction electron contributions to relaxation

Nuclear spins can also relax in the absence of atomic motion. The most common situation of this sort is created by the presence of conduction electrons. They have large magnetic moments just as paramagnetic ions, so they can promote relaxation as well. This is always true for metals. (It is also true for semiconductors, but the temperature dependence of the relaxation is different (26).) Most metals contain approximately one conduction electron per atom, and thus, on the average, about one conduction electron in the vicinity of each nucleus, that is to say, within a distance of the order of the crystal-lattice

spacing. When a conduction electron from the host metal passes close to a nucleus, the nucleus experiences a relatively strong time-varying local magnetic field. This may induce transitions between the magnetic sub-levels of the nucleus, provided the electron is close to the Fermi level. Korringa (27) first studied the interaction between conduction electrons and the nuclear spins by taking account of the Fermi contact interaction. Narath (28) has given the contribution from the conduction electrons to the nuclear spin-lattice relaxation rate in a transition metal as,

$$(T_{1e})^{-1} = 4\pi\gamma^2\hbar k_B T\{[H_{hf}^{(s)}N_s(E_F)]^2 + [H_{hf}^{(d)}N_d(E_F)]^2 q + [H_{hf}^{(0)}N_d(E_F)]^2 P\}, \quad (2\text{-}18)$$

where $H_{hf}^{(s)}$, $H_{hf}^{(d)}$, and $H_{hf}^{(0)}$ are the hyperfine fields at the nucleus due to the contact interaction from s conduction-band electrons, the core polarization from d-band electrons, and the orbital paramagnetic contribution of the d-electrons, respectively. The $N(E_F)$ are the electronic density of states at the Fermi level for these various categories of electrons. The P and q are the band reduction factors related to wavefunction symmetries (28). Korn (29) has suggested that the primary interaction responsible for the proton spin-lattice relaxation in transition metal hydrides may be the orbital contribution, so that,

$$(T_{1e}T)^{-1/2} \simeq (4\pi\gamma^2\hbar k_B)^{1/2} P^{1/2} H_{hf}^{(0)} N_d(E_F). \quad (2\text{-}19)$$

Or, $T_{1e}T = K$, where K is the so-called Korringa constant.

In the rigid-lattice regime (low temperatures), hydrogen diffuses very slowly. For a pure metal-hydride system, the only contribution to the relaxation rate would then come from the conduction electrons. Hence, by measuring T_1 in the rigid-lattice regime where the motional-narrowing effects are negligible, one should obtain a relation, $T_1T = K$. Consequently, the density of states at the Fermi level $N(E_F)$ can be studied since it is related by $(T_{1e}T)^{-1/2} \alpha N(E_F)$.

However, there is yet another relaxation mechanism which always competes with conduction-electron-relaxation; that is relaxation by paramagnetic impurity ions. Uncertainty as to the presence of impurity ions may lead one to an incorrect estimate of the density of states at the Fermi level.

3. Paramagnetic impurity contribution to relaxation

As in the case of the relaxation mechanism due to conduction electrons, it has been known for a long time that a paramagnetic impurity may also be very effective in relaxing the nuclear spins at low temperatures. Paramagnetic impurities have been deliberately doped into the metal hydrides in this study, and these two mechanisms will obviously compete with each other in the low temperature range.

Already in 1949, Bloembergen (30) had investigated the importance of paramagnetic impurities in measuring the relaxation time in insulating solids. For a very dilute inpurity concentration, on the order of one thousand nuclear spins per impurity ion, the nuclear spins

are located at different distances from the impurity ion. The dipolar magnetic field created by the paramagnetic ion drops off as r^{-3}. But all the spins can still relax together since they maintain communication among themselves via the nuclear dipole-dipole coupling (i.e., $T_2 << T_1$). Nuclear magnetization diffuses among the spins to the impurity ion. This process is not the actual diffusion of nuclei but just of their polarization, and is therefore called spin-diffusion.

If one divides the entire sample into many small spherical regions with each sphere having a single impurity ion at its center, the number of nuclear spins enclosed by each sphere is inversely proportional to the impurity concentration. Those spins which are close to the ion will quickly interact directly with the ion, losing their excess energy and cooling down their spin-temperatures. Spins which are farther away from the impurity ion relaxation center have to interact with the ion indirectly by passing their energies to the spins that were already cooled since the direct relaxation rate falls off as r^{-6}. It follows that the relaxation time T_{1p} is directly proportional to the number of spins per impurity ion. In other words, the relaxation rate is proportional to the impurity concentration. The time required for the spins to cool down must also depend on how quickly a spin close to an impurity ion passes its excess energy to that ion.

It is convenient to introduce a quantity, C, which measures the "interaction strength" between an ion and a nucleus at a distance r from the ion, through the relation

$$\tau^{-1}(r) = Cr^{-6} \tag{2-20}$$

where $\tau^{-1}(r)$ is the relaxation rate a single nucleus would have if held at distance r from the ion. C is given by (30),

$$C = \frac{3}{2\pi}(\gamma_p \gamma_n \hbar)^2 \; J(J+1) \; \sin^2\Theta \cos^2\Theta \; \frac{2\pi\tau_i}{1+\omega_0^2\tau_i^2} \tag{2-21}$$

where Θ = the angle between the vector joining the nucleus and the impurity ion, with angular momentum J, and the static magnetic field direction,

τ_i = spin-lattice relaxation time of the impurity ion.

γ_p and γ_n are the gyromagnetic ratios of the paramagnetic ion and the nucleus, respectively. If one averages the angular dependence of C by averaging over the angle Θ, one obtains,

$$\text{Ave } (\sin^2\Theta\cos^2\Theta) = \frac{2}{15} \tag{2-22}$$

Thus, C can be rewritten as,

$$C = \frac{2}{5}(\gamma_p \gamma_n \hbar)^2 \; J(J+1)\frac{\tau_i}{1+\omega_0^2\tau_i^2} \tag{2-23}$$

(Additional terms involving $(\omega_e \pm \omega_0)^2\tau_i^2$ are certainly negligible at low temperatures, and indeed at most temperatures of interest. ω_e is the Larmor frequency of the ion's spin.)

When nuclear spins are close together, the dipolar interaction between them is strong, which implies that the spin-spin relaxation time T_2 is short. Bloembergen (30) derived an approximate relation for the nuclear spin diffusivity,

$$D_s \approx \frac{a^2}{50T_2}. \tag{2-24}$$

This is analogous to the more familiar equation for atomic diffusion by random walk, $D = \frac{a^2}{6\tau_D}$ where τ_D is the mean time between jumps. Here the time for a spin orientation change to traverse a distance, a, is on the order of the nuclear spin-spin relaxation time T_2; in fact, this time is somewhat larger that T_2 partly because T_2^{-1} contains also the effect of local Z-components of the dipolar field which are irrelevant here. The quantity a in Equation (2-24) is the internuclear spacing. The relaxation rate due to the impurity ions is also a function of this spin-diffusion coefficient for the case of dilute impurity concentration.

The theory of the spin-diffusion relaxation process has been developed further by several workers after Bloembergen (30), namely Blumberg (31), Khutsishvili (32), de Gennes (33), and Rorschach (34). Two important limiting regimes arise: the slow diffusion limit and the rapid diffusion limit. In the slow diffusion limit, the bottleneck in the process is the rate at which spins can diffuse to the paramagnetic impurity ion. Khutsishvili (32) and de Gennes (33) have

obtained the spin-lattice relaxation time T_{1p} in this limit as

$$T_{1p} = \frac{3}{8\pi N D_s \beta} = \frac{3}{8\pi N C^{1/4} D_s^{3/4}} \qquad (2\text{-}25)$$

where $\beta = (C/D_s)^{1/4}$

= "Pseudo-potential" radius, essentially the distance at which the times for direct relaxation in Equation (2-20) and for spin diffusion, $\sim r^2/D_s$, are equal,

$N = 4x/a_0^3$ for the fcc case,

= The impurity concentration in number per unit volume, where x is the impurity concentration expressed as a fraction of the number of host metal atoms,

a_0 = Lattice constant.

In the rapid diffusion limit, the bottleneck is the rate at which the impurity can equilibrate spins in its immediate neighborhood. Blumberg (31) has calculated an expression for the spin-lattice relaxation time in this limit,

$$T_{1p} = \frac{3}{8\pi N D_s \beta} \left(\frac{2b^3}{\beta^3}\right) = \frac{6b^3}{8\pi N C} \qquad (2\text{-}26)$$

where b = the diffusion barrier radius inside of which spin-diffusion cannot occur because the local field in the direction of H_0 due to the impurity ion changes so much from site to site that

spin-exchange no longer conserves energy.

Finally, Rorschach (34) generalized the theory and obtained an expression for the spin-lattice relaxation time of a system of nuclei having spin $I = \frac{1}{2}$,

$$T_{1p} = \frac{1}{8\pi N D_s \beta} \frac{\Gamma(\frac{1}{4})}{\Gamma(\frac{3}{4})} \frac{I_{-3/4}(\delta)}{I_{3/4}(\delta)} \tag{2-27}$$

where $I_m(\delta)$ = the modified Bessel Function (35),

$$b = \left[\frac{3\langle\mu_p\rangle}{\mu_n}\right]^{1/4} \left(\frac{a_0}{2}\right), \tag{2-28}$$

$$\delta = \frac{\beta^2}{2b^2}, \tag{2-29}$$

$$\langle\mu_p\rangle = g\mu_0 J\left[B^2(x) + \frac{\partial B(x)}{\partial x} \frac{2}{\pi} \tan^{-1} \frac{2\pi\tau_i}{T_2}\right]^{1/2}, \tag{2-30}$$

$$B(x) = \left(\frac{2J+1}{2J}\right) \coth \left(\frac{2J+1}{2J}\right)x - \frac{1}{2J} \coth \frac{x}{2J}, \tag{2-31}$$

$$x = \frac{gJ\mu_0 H_0}{k_B T}. \tag{2-32}$$

According to Rorschach, the value of δ determines the two limits; $\delta << 1$ for the rapid diffusion limit, and $\delta >> 1$ for the slow diffusion limit. Rorschach's general equation correctly yields the Khutsishvili (32) and Blumberg (31) equations depending upon these values of δ. For $\delta << 1$, the modified Bessel function $I_m(\delta)$ becomes $[\frac{1}{\Gamma(m+1)}](\frac{\delta}{2})^m$, and Equation (2-27) reduces to

$$T_{1p} = \frac{3}{8\pi N D_s \beta} (\frac{2b^3}{\beta^3}), \tag{2-33}$$

in agreement with Blumberg's Equation (2-26) for the rapid diffusion limit. For $\delta >> 1$, the modified Bessel function $I_m(\delta) = I_{-m}(\delta)$, giving

$$T_{1p} = \frac{3}{8\pi N D_s \beta} \tag{2-34}$$

which is the Khutsishvili expression, Equation (2-25). Rorschach has also shown that the transition from the rapid diffusion limit to the slow diffusion limit is essentially accomplished over a small change of δ near $\delta = 1$, i.e., $0.3 \lesssim \delta \lesssim 2$.

The general expression for T_{1p} discussed above holds for the paramagnetic impurity ion induced relaxation in the temperature range where the atomic motions are very slow and negligible as compare to the spin-diffusion. As the temperature increases, atomic diffusion becomes significant and will reinforce the interaction between the impurity ions and the spins which are far away from the impurity relaxation

center. Shen (36) first suggested replacing the coefficient of diffusion for spin-diffusion D_s by the atomic diffusion coefficient D_A in the temperature range where atomic diffusion is effective, that is, in the motional-narrowing region ($\tau_D \lesssim T_2$). Shen prcposed that the expression for the slow diffusion limit in the higher temperature range be,

$$T_{1p} = \frac{3}{8\pi N D_A \beta} \tag{2-35}$$

where now $D_A = D_0 \exp(-E_{act}/k_B T)$, (2-36)

$$\beta = (C/D_A)^{1/4}. \tag{2-37}$$

Richards (37) showed that this replacement of spin diffusion by atomic diffusion could be extended to Rorschach's general Equation (2-27):

$$T_{1p} = \frac{1}{8\pi N D_A \beta} \frac{\Gamma(\frac{1}{4})}{\Gamma(\frac{3}{4})} \frac{I_{-3/4}(\delta_a)}{I_{3/4}(\delta_a)} \tag{2-38}$$

with $$\delta_a = \frac{\beta^2}{2a_1^2} \text{ and } a_1 = \frac{\sqrt{3}a_0}{4} \tag{2-39}$$

Richards also treated the case, important over a small temperature range, where D_A and D_s are comparable. It is also important to note that, when atomic diffusion is not negligible, τ_i in Equation (2-23) must be replaced by τ_i^* where $\tau_i^{*-1} = \tau_i^{-1} + \tau_D^{-1}$.

Finally, it should be mentioned that, besides the dipolar interaction, there will also be an indirect ("RKKY") interaction between protons and paramagnetic centers through the conduction electrons. It has recently been found by Lu (38) for the case of ScH_x containing Gd^{3+} impurity that this interaction is unable to account for the behavior of the proton relaxation, which was essentially similar to the present results. In view of this, and the fact that the dipolar interaction will be shown to account for the bulk of our observed effects, at least in the case of Gd^{3+} impurities, this interaction will be neglected when interpreting the present results.

4. Other relaxation mechanisms

There are also other relaxation mechanisms which involve the random motions of the atoms or molecules. These include quadrupolar relaxation, chemical shift anisotropy relaxation, and spin-rotation relaxation. These relaxation mechanisms are not important in this investigation, and we shall not discuss them further.

III. SAMPLES AND APPARATUS

A. Sample Preparation

All the hydride samples studied in this investigation were prepared in the laboratories of B. J. Beaudry and D. T. Peterson in the Materials Sciences Division of the Ames Laboratory from the highest purity Ames Laboratory lanthanum and yttrium metals. The starting pure metals were analyzed by spark source mass spectrometry. The analyses listed in the Appendix show that they contained very small amounts of paramagnetic impurities, on the order of 2 to 3 parts per million (ppm) before they were deliberately doped with other rare-earth impurities (Ce, Nd, Gd, Dy, Er) to form the metallic alloys. These alloys were prepared in a two-step process in the Materials Sciences Division of the Ames Laboratory.

Beginning with the pure metal, an arc-melted sample which contained one atomic percent solute was prepared. This alloy was then used to introduce the solute at the lower levels (50 ppm to 900 ppm) which were used in all the NMR measurements. After careful calculating and weighing in order to achieve alloys as close to the desired concentration as possible, the correct alloy concentrations were obtained. Pure yttrium metal and yttrium doped with various rare-earth impurities (Ce, Nd, Gd, Dy, Er) were then sent to Dr. D. T. Peterson for hydriding. The pure lanthanum metal and rare-earth doped (Ce, Gd) lanthanum-based alloys remained in Mr. Beaudry's laboratory for hydriding.

A piece of solid lanthanum metal or alloy was placed in a platinum boat after it had been carefully electropolished. The hydriding

reaction was carried out in a standard high-pressure and high-vacuum system by using MMH_3 (MM = mischmetal) as the hydrogen gas source. The system was pumped down to 2×10^{-7} torr before heating the alloy. After the temperature of the alloy had reached about 400°C (∿673K) in vacuum, hydrogen was admitted to the system for reaction. To further check the pressure-composition equilibrium, samples were heated up to 500°C (∿773K). It was then observed that the equilibrium partial pressure of the hydrogen over the sample was greater than zero at these temperatures. This ensures the complete homogenization of the samples. After hydriding, the system was backfilled with argon gas. The sample was then transferred to a helium filled drybox (<0.1 ppm water vapor) and was crushed in a mortar. The resulting fine powder was sealed in a quartz tube (under helium), ready for NMR measurements. The hydrogen concentrations were determined from the pressure change in a calibrated volume of gas and from the weight increase of the samples on hydriding.

The yttrium metal and yttrium alloys were electropolished carefully in $HClO_4$-methanol. Since tantalum-foil can act as a semi-membrane for hydrogen at high temperature, a 50 μm thick tantalum-foil was used to wrap the metal (∿3 grams). Tantalum-foil allows hydrogen to diffuse through to the metal easily at the high temperature, but prevents all other gases from penetrating (O_2, N_2, CO, H_2O, etc.). It also protects the yttrium metal from SiO_2 or stainless steel.

The metal was first degassed at 1000°C under vacuum for about twenty minutes, and was then charged with hydrogen gas, obtained from the

decomposition of uranium hydride (UH_3), at 1.34 atm pressure and 850°C (1123K) temperature. To allow the sample to homogenize, it was held at 850°C for approximately 24 hours. Hence, equilibrium was reached, and the hydrogen had diffused throughout the sample. The sample was then removed from the furnace, so that it could cool down rapidly (33°C/min). This rapid cooling prevents the formation of yttrium trihydride during cooling. A small piece (~20 mg) of the hydride sample was cut for the determination of the exact hydrogen concentration by hot vacuum extraction. This piece was heated to about 950°C in vacuum, and the boiled-off hydrogen was collected and measured. Exact hydrogen concentration can be determined from the pressure change and the volume of the hydrogen. The accuracy of the hydrogen concentration determination is approximately $\pm$2%.

The yttrium hydride was then ground in a diamond mortar by impact grinding. A small magnet was used to remove any remaining iron particles from the powder. The resulting fine powder was then sealed in a fused quartz tube for NMR measurements.

B. Pulsed NMR Spectrometer

The pulsed NMR Spectrometer used in the measurements for this investigation was constructed by D. R. Torgeson, P. A. Hornung, and D. Adduci in the Ames Laboratory. It has been described in detail elsewhere (39,40,41). A simplified block diagram of this spectrometer is shown in Figure 3-1. Essentially, it contains seven interconnected electronic units. These will be briefly described in the remainder of this section.

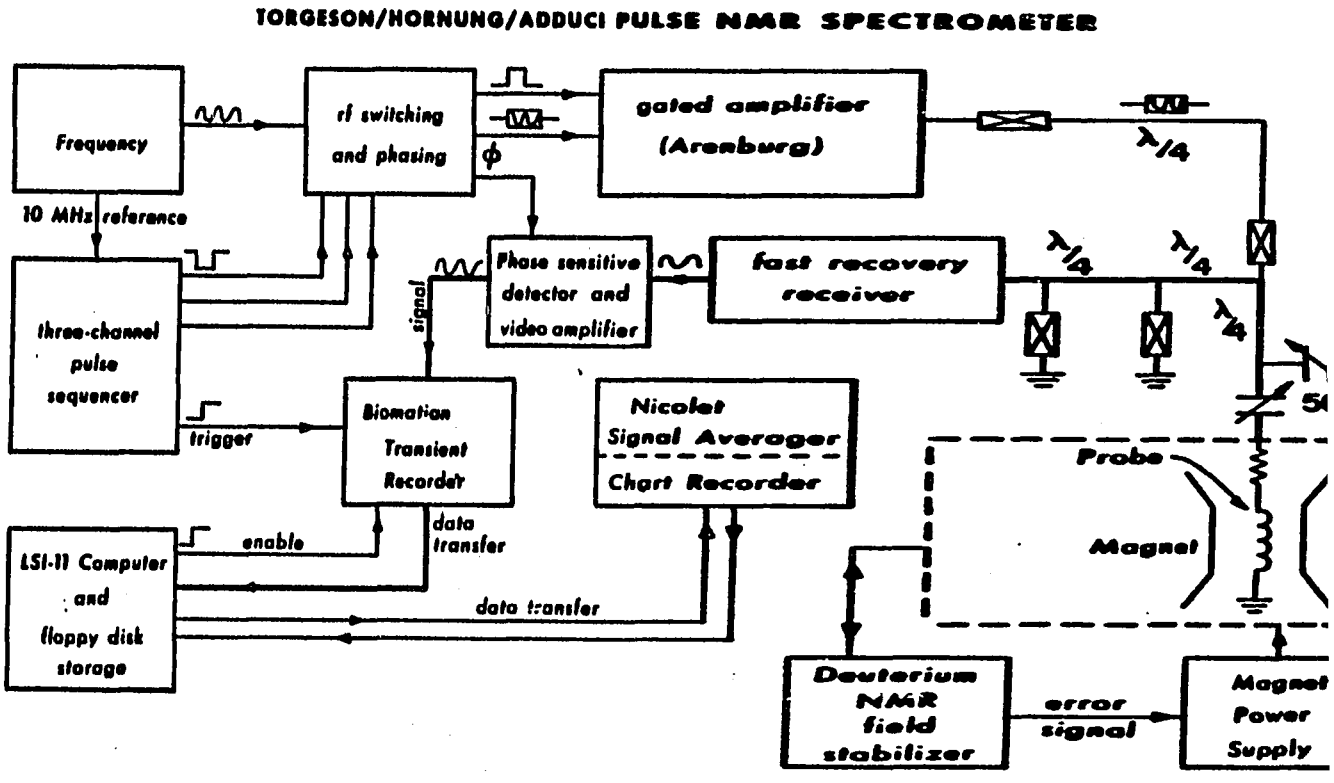

Figure 3-1. The block diagram of the pulsed NMR spectrometer used in this study. The heavy line indicates the path of the NMR signal

1. Magnet

A Varian electromagnet, model V-4012A, provided the required strong laboratory magnetic field throughout the course of these measurements. For the resonance frequency of 40MHz, as in this study, the static magnetic field was set to the value, H_0 = 9.3950 kOe. Generally speaking, the magnet system provided a field that was stable within acceptable experimental limits. However, an NMR field stabilizer was used to prevent residual field drift. A small sample container of D_2O plus 0.25 moles/l of $MnSO_4 \cdot H_2O$ was used, and the field was locked at the ^2D resonance frequency of ν = 6.1402MHz which corresponds to the resonance frequency of 40MHz for the proton, ^1H, in the same field (9.3950 kOe). The field can be stabilized in this way for months without serious drifting. All the proton spin-lattice relaxation times at 77K were measured at 35MHz instead of 40MHz by using a similar but different apparatus because of the geometry of a finger dewar filled with liquid nitrogen. The field at 35MHz was produced by a Harvey-Wells 12-inch electromagnet, providing a static field of H_0 = 8.2206 kOe. Another NMR field stabilizer tuned at 5.3727MHz for ^2D was used to stabilize this magnet.

2. Pulse programmer

The pulse programmer used in the spectrometer system is a modification of the Conway-Cotts design (40). A detailed description can be found in (41). The programmer is the major control for the spectrometer; it creates the appropriate pulse sequences for the measurements. Each

of the sequences produced can be started and repeated by manual control or can be completely controlled by a clock module which has digitally selectable rates ranging from 1 μs to 999 sec. These sequences can be repeated at a fixed rate that is set by the clock module. Each of the channel modules can produce 1 to 999 pulses with selected intervals between them, provided all the pulses have the same phase and width. The width of each pulse is set by a continuously adjustable control. There is a selectable delayed start pulse available to start the next channel after the previous one is triggered. An auto-increment module (41) in the programmer has a selectable range of increments to increase the time interval τ between the two channels. The increments increase by either 1, 2, 4, or 8 times the time base selected. In other words, this auto-increment module can advance the start delays for successive clock cycles. It allows τ to be varied automatically in a π, T, $\pi/2$ sequence (see Chapter IV), thereby tracing a magnetization recovery curve into the Nicolet signal averager for data storage.

3. Transmitter

A crystal oscillator at 40MHz was used as a radiofrequency (rf) source throughout the investigation. The rf output is amplified and split into three separate paths in the rf switching module. One of these goes to the phase sensitive detector, and the remaining two paths provide two possible rf phases to the transmitter. Each channel module delivers its output logic pulses to the rf switch module at which the phase of the rf pulse is selected. The rf switch module has a variable

rf amplitude path A and a variable rf phase path B. The important criteria for the stability of multiple pulse measurements and phase sensitive detection are that all pulses be coherent with each other and also time coherent. These criteria can be achieved by switching the rf to the selected path and switching again at the summing point, thereby doubly isolating the C.W. rf source from the transmitter. An Arenburg Ultrasonics PG-650C gated power amplifier is used to amplify the rf pulses to a power level of approximately 800 watts. The rf pulses are then output to the sample from the Arenburg. This transmitter is capable of producing sufficiently strong rf pulses to meet the requirement of the experiment.

4. The probe system

A good probe system must not only be capable of delivering high power rf pulses to the sample coil, it must also have the capability of detecting the very low power signal induced by the nuclear moments about a microsecond after the pulse. The sample probe consists of two major parts, the matching system and the sample coil. Figure 3-2 shows the block diagram of the probe. The probe can be operated at high voltages since the matching capacitors are independent mechanical units which have external tunability. The probe is tuned with a Hewlett Packard 4815A RF vector impedance meter. The power from the transmitter is most efficiently coupled to the coil and sample when the probe is tuned to 50Ω and 0^{o} phase. This can be done by adjusting the two capacitors to achieve a match to the characteristic impedance of the coaxial cable

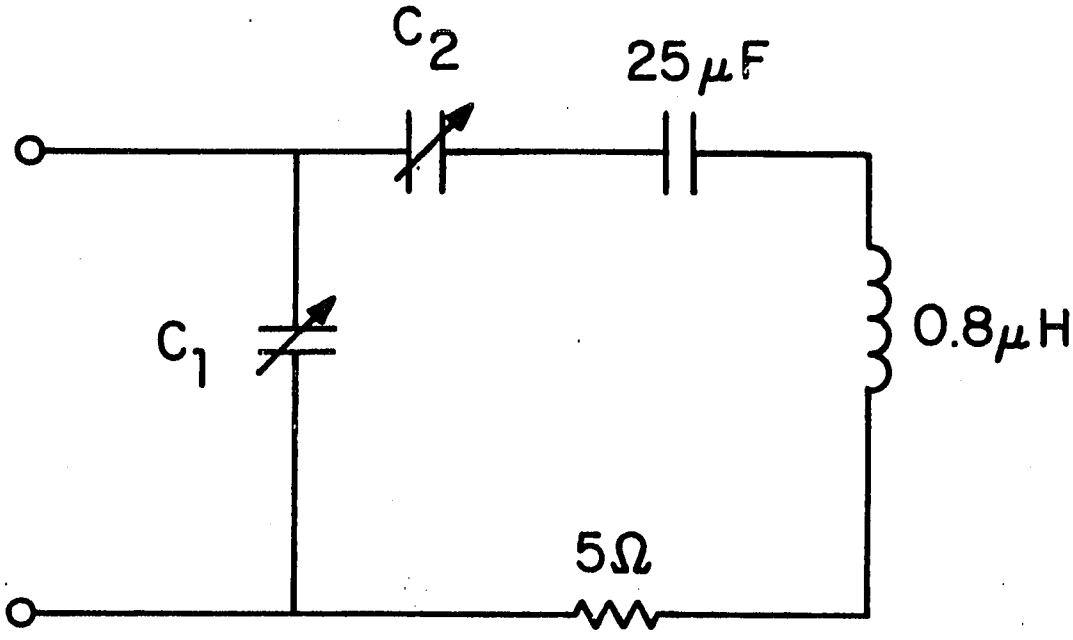

Figure 3-2. The probe used in this study at the frequency of 40MHz. It has a Q-value of about 40

from the duplexer at 40MHz.

The sample coil used was made of No. 15 copper wire. The Nyclad insulation was burned off before making the 18 turn coil with radius of 6 mm for each turn, yielding an inductance of about 0.8 μH. With the combination of a 5Ω resistor and 0.8 μH sample coil, a Q-value of about 40 is obtained for the frequency of 40MHz:

$$Q = \frac{\omega L}{R}$$

$$= \frac{2\pi \times 40 \times 10^{6} \times 0.8 \times 10^{-6}}{5}$$

$$\simeq 40.$$

5. Receiver

In order to deliver the high voltage rf pulses from the transmitter to the sample probe and transfer the very low-level signal induced by the sample to the receiver, the circuitry of the duplexer which is taken from that of Lowe and Tarr (42) was employed. The function of the duplexer is to connect the transmitter to the probe during transmission of the rf pulse while disconnecting the receiver from the probe. Alternatively, it turns on the receiver during detection of the induced signal from the probe, at the same time disconnecting the transmitter from the probe.

This is achieved by using three one-quarter wavelength cables, two series diodes (SD) and two diode shorts (DS) in the arrangement as seen in Figure 3-1. The function of the series diodes is to pass the high voltage rf pulses and block the low amplitude (<1 volt) induced signal from the sample probe. Such an arrangement prevents reflections

returning to the transmitter from a mismatched load and eliminates any reflection noise from the receiver. In contrast, the diode shorts pass the low amplitude induced signals and disconnect the high voltage rf pulses. The high voltage rf pulses from the transmitter may break into two branches at the junction. One of the branches has one-quarter wavelength cables and diode shorts; hence, the high voltage rf pulse is disconnected by seeing a high impedance resonant circuit which dissipates no energy. The other branch contains the matching system which is tuned to the characteristic impedance at 40MHz. Since the induced signal from the sample is blocked from going to the transmitter, the only path it can follow is the one that leads to the receiver. The only power dissipated in the diode shorts is the one-volt offset that is required for the diodes to conduct, since the high voltage rf pulses are shorted at the diode shorts following the one-quarter wavelength cable. The next one-quarter wavelength cable and diode short reduce the high voltage rf pulse further, so that the input to the receiver is then about one volt peak-to-peak from the rf pulse plus an unattenuated induced signal from the sample probe.

The main rf receiver consists of three Spectrum Microwave Wideband Limiting amplifiers, Model SML-D (39). These are connected by low Q series filters which are tuned at the operating frequency 40MHz. This enables parasitic oscillations to be eliminated. The recovery time to full gain varies with respect to the width of the rf pulse; the typical recovery time is about 400 ns. Amplification of the signal in the

rf portion is about 60 db. At the end of the rf chain, the output of the receiver is phase-sensitively detected by a reference signal from the rf switch module. The output video signal is then amplified further. This video amplifier has a range of selectable gain levels and variable filter settings and has a gain-bandwidth product of about 50MHz with selectable gains of 35, 40, 45, 50, 55 db. The signal is then displayed on an oscilloscope and is input to the Nicolet 1072 Signal Averager from the LSI-11 computer.

6. Data storage

For simplicity, data can be stored in the Nicolet 1072 signal averager so that they can be accessed directly. In the case of rapid free induction decays, a Biomation 610B transient recorder was used to obtain better short time resolution. In order to allow the entire magnetization recovery to be recorded, the Nicolet 1072 signal averager was usually triggered in an external address advance mode. The address advance pulse from the NMR pulse programmer fed to the Biomation's input which in turn initiates a new Biomation sweep for each pulse spacing between the π and $\pi/2$ pulses when the autoincrement technique is employed. The information at a fixed location (average of several points) of the free induction decay is transferred from the Biomation transient recorder to the Nicolet signal averager and stored in its memory after the external advance trigger pulse is sent. The signal averager then advances its storage address. The pulse sequence can be successively repeated and averaged over several complete recovery curves

by using another trigger to reset the channel address. The data can be read from the spectrometer's oscilloscope, the chart recorder, or directly from the Nicolet by digital readout. Throughout the course of the study, an interface built by the Ames Laboratory Instrumentation Group was employed to allow data to be transferred to and from the Nicolet signal averager to a Digital Equipment Corporation LSI-11 computer for direct data reduction. A least squares fit program is used to extract the proton spin-lattice relaxation time from the magnetization recovery data. The values of the magnetization as a function of time, the fitting parameters and the quality of fit are then printed out by a printer (Loonam Associates Inc. model 43). The data and the line of the least squares fit are also transferred from the LSI-11 memory buffer to the Nicolet memory for inspection. The chart recorder is used here to plot the magnetization recovery curve and fitting line on graph paper for record. The same information was also stored on floppy disk by the LSI-11 computer.

7. Temperature control system

The investigation required a wide range of stable temperatures in the sample environment. Therefore, a nitrogen gas-flow sample chamber was used (designed and constructed by D. R. Torgeson). This gas-flow sample chamber allows the temperature to vary between 100K and 800K with reliable accuracy. Figure 3-3 shows the detailed structure of the chamber. The vacuum between the double brass walls is used to insulate

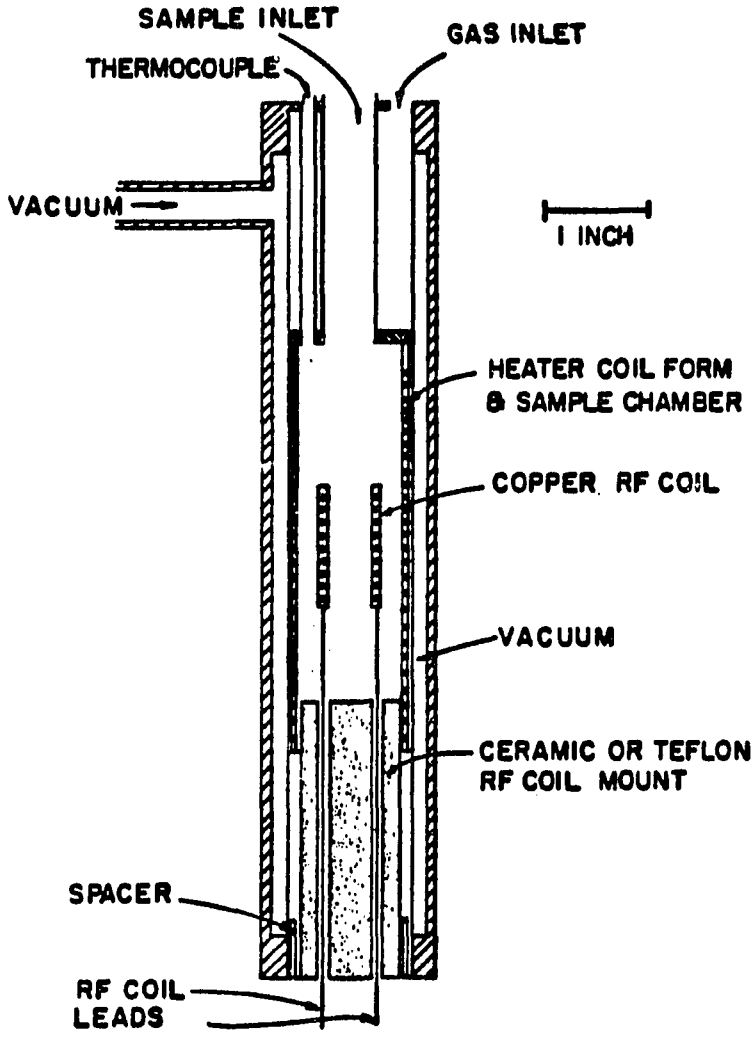

Figure 3-3. Gas-flow variable temperature chamber used for temperatures between 100K and 800K

the assembly and reduce the temperature gradient around the sample area. Double cotton insulated heater wire (0.583 Ω/ft) was used to form the heater coil on the outside of the inner-tube, with a resistance of approximately 15 Ω. The sample and sample coil are placed inside the inner tube. The heater wire is then connected to a power supply and temperature control unit which allows fine adjustments to the sample temperature. A thermocouple is placed next to the sample and connected to a Leeds and Northrup 7553-5 Type K-3 potentiometer. The potentiometer balance is monitored by a 845 AR High Impedance voltmeter-null detector. There are two temperature ranges in the experiment, namely, temperatures below room temperature and temperatures above room temperature. A copper-constantan thermocouple (Omega Engineering Inc.) was used for temperatures between 666K and 100K; it is replaced by a Pt-PtRh thermocouple for temperatures higher than 666K.

Cold nitrogen gas obtained by controlled boiling of liquid nitrogen with two 66Ω, 150W heaters in a 50 liter dewar is passed across the sample to obtain temperatures below room temperature. The temperature in this range is controlled by the flow rate of the cold nitrogen gas and the 15Ω heater-coil that is wired on the inner tube. For temperatures above room temperature, the dry nitrogen gas from the gas inlet is heated by the 15Ω heater-coil and then passed across the sample. The temperature is again regulated by the temperature control unit (potentiometer, null detector and power supply).

IV. EXPERIMENTAL METHOD

The proton spin-lattice relaxation time (T_1) measurements were taken with the previously described pulsed NMR spectrometer. The details of pulsed NMR experiments and techniques have been described in several well-known texts (43,44,45). Basically, pulsed NMR methods are used to study the behavior of the nuclear magnetization after it has been disturbed from equilibrium. The basic experiment traces the response of the magnetization to a sequence of radiofrequency pulses and follows its recovery towards the equilibrium state. This is done by tipping the magnetization away from equilibrium by an appropriate rf pulse, and by using another rf pulse to monitor the recovery of the magnetization. It is difficult to visualize the motion of the magnetization in a static reference frame because all the motions are superimposed on the rapid Larmor precession. This difficulty can be eliminated by working in a coordinate system that rotates about the static field at the applied radiofrequency.

Let the laboratory Cartesian axes be X, Y, Z and the rotating frame be X', Y', Z'. Consider the laboratory frame placed in the corner of the laboratory room with its Z-axis pointing up and X and Y axes lying on the floor. Then imagine a turntable in the room with its spindle denoting the Z'-axis and two mutually perpendicular lines on the turntable floor representing the X' and Y' axes. The Z and Z' axes continue to point in the same direction (towards the ceiling) no matter

how fast the table turns, but the X' and Y' axes rotate with respect to the X and Y axes. If a magnetization vector rotates at the Larmor precession frequency about the Z-axis as viewed in the laboratory frame, it will appear to be stationary as the observer views it from the turntable rotating at the Larmor frequency. Therefore, the effect of the static magnetic field disappears from the equations of motion of the magnetization due to the transformation from the laboratory frame to a frame rotating at the Larmor frequency. This transformation simplifies the understanding of NMR experiments.

The axis of the rf coil and sample is placed perpendicular to the direction of the applied static magnetic field; see Figure 4-1(a). The strength of the static magnetic field is approximately 9.4 kOe in this study, and the magnetization induced by the static field points in the Z direction (as well as the Z'direction). When the rf transmitter is turned on, the sinusoidal rf current in the coil generates a linearly polarized magnetic field $2H_1 \cos\omega t$ in the direction parallel to the axis of the coil. This field can be divided into two rotating fields, see Figure 4-1(b), each having magnitude H_1 and rotating in opposite directions. One of the rotating fields will have the correct sense of precession to be stationary in the rotating frame which rotates at the Larmor frequency ω_o. The other one has very little effect on the magnetization since its direction of rotation places it $2\omega_o$ away from the resonance condition. In addition, the relative direction of the magnetic field pulse can be varied in the rotating-frame by choosing

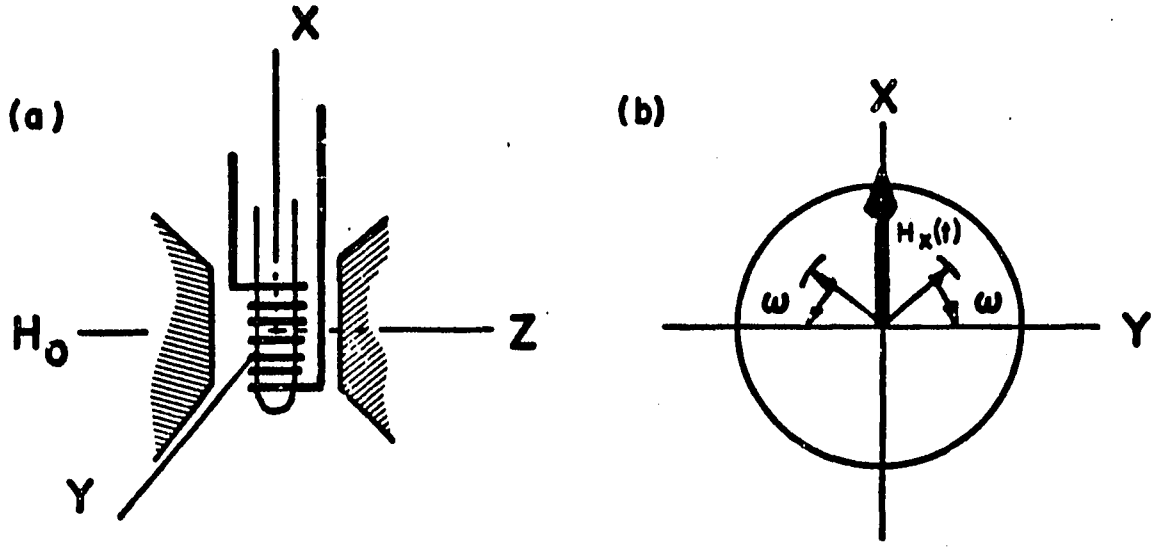

Figure 4-1. Arrangement of stationary and rotating magnetic fields in NMR experiments: (a) the axis of the rf coil and sample is perpendicular to the direction of the static magnetic field; (b) decomposition of the linearly polarized magnetic field $2H_1\cos\omega t$, which is in the direction parallel to the axis of the rf coil, into two counter-rotating fields each of magnitude H_1

the appropriate phase for the rf current that is applied to the coil. Similarly, by varying the reference phase to the phase sensitive-detector, the in-phase and quadrature signal components in the X'Y' rotating plane can be detected separately. As mentioned earlier, the rf field component that fulfills the resonance condition is stationary in the rotating frame.

Classically, the time rate of change of the magnetization $\vec{M}$ in the magnetic field $\vec{H}_o$ is described by the equation,

$$\frac{d\vec{M}}{dt} = \vec{M} \times \gamma\vec{H}_o \tag{4-1}$$

where γ is the gyromagnetic ratio for a given nucleus. The direction of the change is perpendicular to both the magnetization $\vec{M}$ and the field $\vec{H}_o$. The solution of the above equation is a precession of $\vec{M}$ about $\vec{H}_o$ at the Larmor frequency $\vec{\omega}_o = -\gamma\vec{H}_o$ without any change in the magnitude $\vec{M}$. Now, from classical mechanics (46), the time derivative $\frac{\delta\vec{M}}{\delta t}$ of a vector $\vec{M}$ in the frame rotating with angular velocity $\vec{\Omega}$ is

$$\frac{\delta\vec{M}}{\delta t} = \frac{d\vec{M}}{dt} - (\vec{\Omega}\times\vec{M}). \tag{4-2}$$

Thus,
$$\frac{\delta\vec{M}}{\delta t} = \vec{M} \times \gamma\vec{H}_o - \vec{\Omega} \times\vec{M}$$

$$= \vec{M} \times \gamma(\vec{H}_o + \frac{\vec{\Omega}}{\gamma})$$

$$= \vec{M} \times \gamma\vec{H}_e \tag{4-3}$$

Hence, the time derivative of $\vec{M}$ viewed from the reference frame rotating at $\vec{\Omega}$ is the same as that in the laboratory frame of reference except for the substitution of an effective field in place of the applied field $\vec{H}_o$,

$$\vec{H}_e = \vec{H}_o + \frac{\vec{\Omega}}{\gamma}. \tag{4-4}$$

If the angular velocity of the rotating frame is set equal to the Larmor frequency, $-\gamma\vec{H}_o$, the effective field $\vec{H}_e = 0$, and the magnetization becomes stationary in the rotating frame. If the phase relationship between the rotating magnetic field and the rotating frame is properly selected, the rf field will be fixed along the rotating X'-axis. At the resonance condition, the effective field $\vec{H}_e = H_1\hat{i}$ where $\hat{i}$ is the unit vector along X' and H_1 is the magnitude of the rf field. Thus, in the rotating-frame,

$$\frac{\delta\vec{M}}{\delta t} = \gamma\vec{M} \times \vec{H}_1. \tag{4-5}$$

By choosing $\vec{M} = M_o\hat{k}$ and $\vec{H}_1 = H_1\hat{i}$, the solution to Equation (4-5) is:

$$M_{z'} = M_o \cos \gamma H_1 t = M_z \tag{4-6}$$

$$M_{y'} = M_o \sin \gamma H_1 t \tag{4-7}$$

Because the rf field $\vec{H}_1$ does work on the magnetization $\vec{M}$, the magnetization changes its orientation with respect to the static field $\vec{H}_o$. Therefore, an appropriate combination of the strength and duration of the rf pulse can tip the magnetization away from the static field direction through any desired angle. The usual rotating field strength is about a thousand times smaller than the strength of the steady field. Thus, the magnetization is turned through an angle $\Theta = \gamma H_1 t$ when the pulse is applied for a time t. Consequently, a short pulse of radiofrequency field can create a nonequilibrium situation, changing the energy of the spin system. The magnetization can be forced into the plane perpendicular to the static magnetic field by applying an rf pulse of duration, $t = (\pi/2)/\gamma H_1$. Viewed in the rotating-frame, the magnetization $\vec{M}$ is turned $\pi/2$ away from $\vec{H}_o$ into the X'Y' plane as shown in Figure 4-2(a).

After the rf field $\vec{H}_1$ is turned off, the magnetization will precess freely in the XY plane in the laboratory frame, and the precessing magnetization will return to its equilibrium position. As the system returns to equilibrium, two mechanisms are responsible for the recovery of the magnetization in time. Due to the inhomogeneity of the local field distribution, some nuclei will experience slightly higher resonance fields (and some slightly lower) and will precess faster (slower) than others. These nuclei cause the magnetization $\vec{M}$ to fan out from the Y'-axis in the rotating frame, resulting in the dephasing of the magnetization in the X'Y' plane, as seen in Figure 4-2(b).

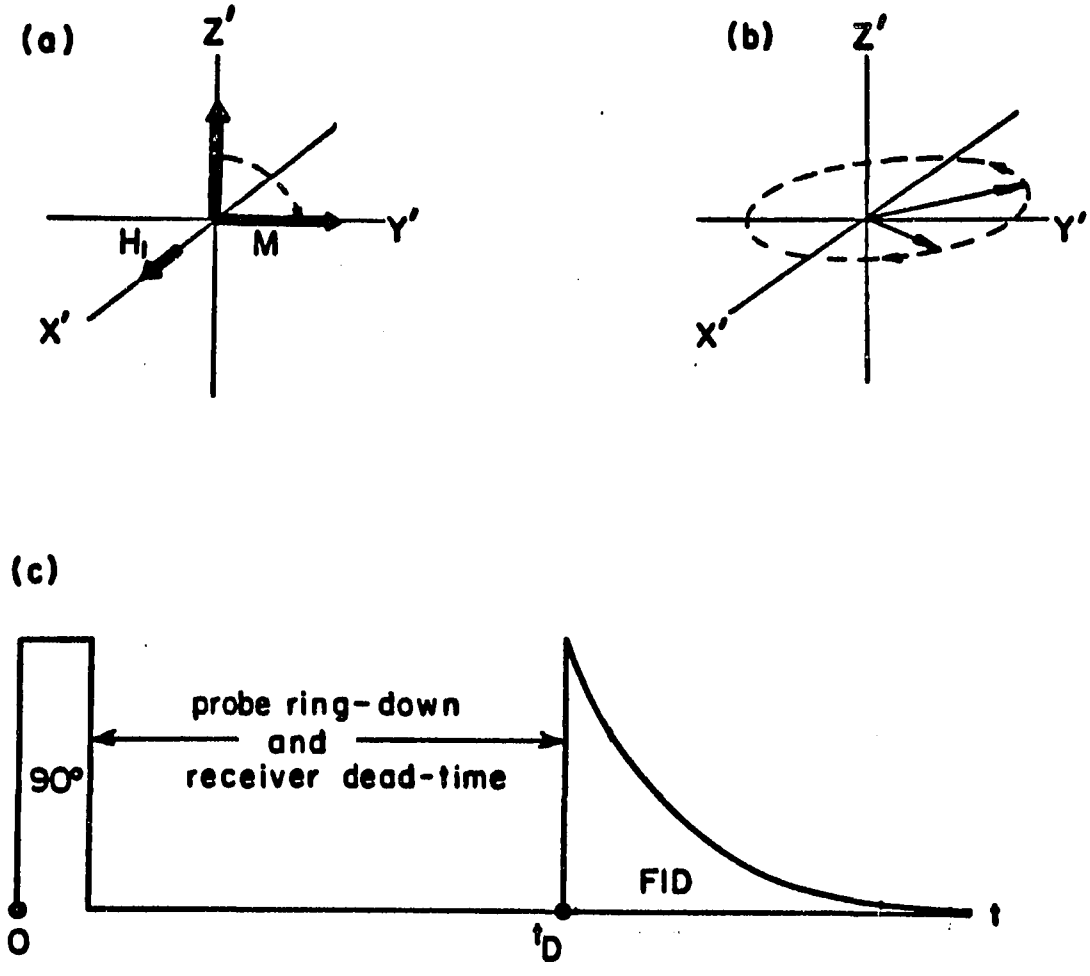

Figure 4-2. A $\pi/2$ pulse and the resulting behavior of the nuclear magnetizations: (a) a $\pi/2$ rf pulse along the X'-axis rotates the magnetization M from the equilibrium position (along Z-axis) to the Y'-axis; (b) after $\vec{H}_1$ is turned off, the inhomogeneity of the local field distribution causes the magnetization in the X'Y'-plane to dephase; (c) exponential free induction decay (FID) after the $\pi/2$ rf pulse is turned off

Because thermal equilibrium begins to be re-established after the pulse is turned off, the magnetization also tends to recover along the Z = Z' direction. In the rf coil with its axis perpendicular to the static magnetic field, the rotation and dephasing of the magnetization in the XY-plane induces a decaying sinusoidal rf current at the Larmor frequency. This induced signal is a free precession signal and is called the free induction decay (FID), shown in Figure 4-2(c). For a single Lorentian line, the decay of M_{xy} is exponential in time with a time constant T_2^*, and the output of the coil will be a sinusoidal wave whose amplitude decays at the rate exp $(-t/T_2^*)$. Eventually, the magnetization will re-establish itself along the Z-direction in equilibrium with the applied field; the time constant characteristic of this recovery is the spin-lattice relaxation time, T_1. The recovery of the Z-component of the magnetization is expressed by the equation,

$$M_z = M_o[1-\exp(-\tau/T_1)] \tag{4-8}$$

It is important to note that in solids T_1 is usually much longer (several orders of magnitude) than T_2^*, so that the M_z recovery is a much slower process than the time duration of the FID. In the case of the hydrides studied in this work, T_2^* is on the order of 10 μs whereas the T_1 values range from about 10 ms to 4 s.

Since the sample coil is arranged in such a way that it is sensitive only to the component of the magnetization in the XY-plane, the recovery of the magnetization along the Z = Z' axis due to the T_1 process is not

detectable unless it is also rotated away from the Z'-axis. A second pulse is required to measure this recovery and thereby the spin-lattice relaxation time T_1. Many different pulse-sequences may be employed to measure T_1 (44). To mention a few, these include the saturating comb sequence, the progressive saturation with inversion recovery sequence, the steady state sequence, and double pulse sequences (inversion and saturation recovery). Out of all these, one of the most accurate and commonly used is the last in the form of a π, τ, $\pi/2$ pulse sequence. This method has been used throughout this study. The initial π pulse inverts the magnetization so that $M_z(0) = -M_o$, reversing the populations of the spin levels and raising the energy of the spin system; see Figure 4-3(a). Since only the component of the magnetization in the XY-plane can be detected, a $\pi/2$ pulse is applied after a variable delay time τ. This $\pi/2$ pulse tips the growing Z-component of the recovering magnetization into the XY-plane, as shown in Figure 4-3(b), where it induces a signal in the rf coil. Basically, the $\pi/2$ pulse is used to examine the recovery of the magnetization along the $Z = Z'$ axis after a delay, as seen in Figure 4-3(c). The equation for the recovery of the magnetization in this pulse sequence is,

$$M_z = M_o[1-2\ \exp(-\tau/T_1)] \qquad (4-9)$$

Therefore, by varying the delay time τ between the π and $\pi/2$ pulses (see Figure 4-3(d)) one is able to trace out the recovery of the

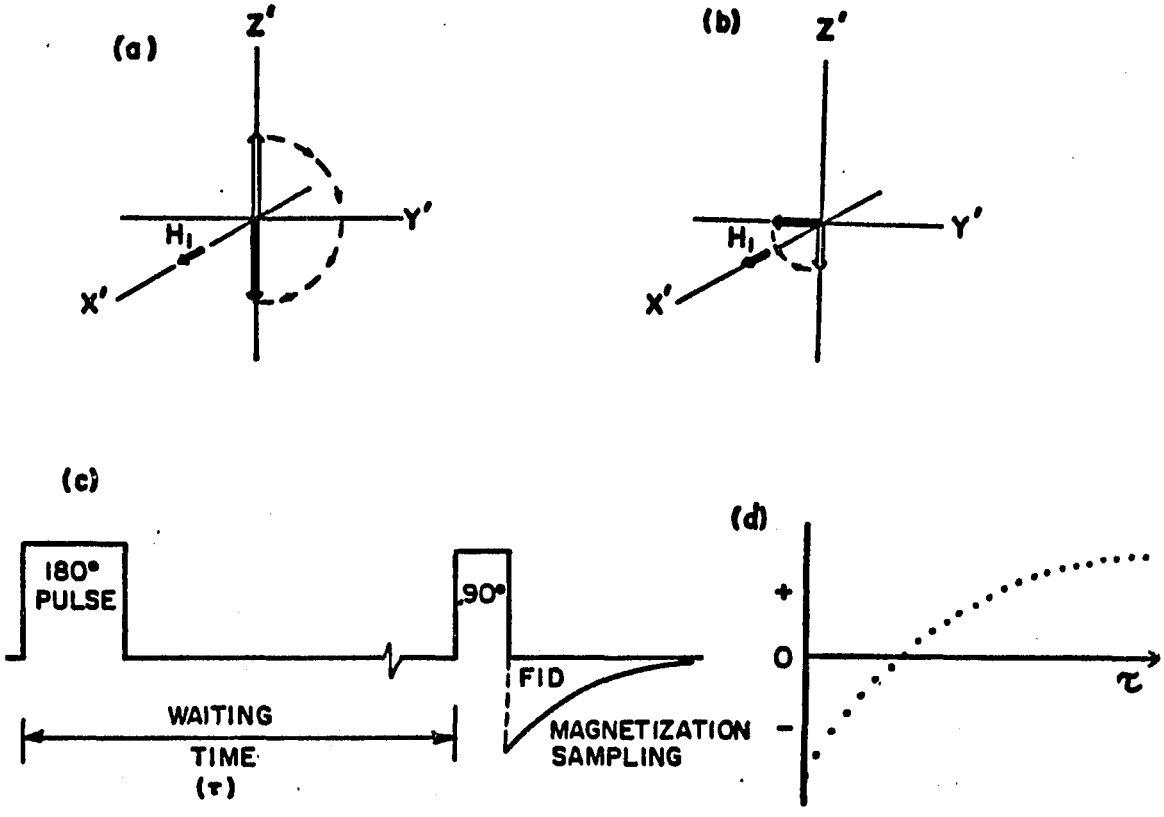

Figure 4-3. Determination of T_1 by π, τ, $\pi/2$ sequence: (a) the π pulse inverts the magnetization $\vec{M}$ so that $M_z(0) = -M_o$; (b) after a variable delay time τ, the growing Z-component of the recovering magnetization is tipped into the XY-plane by a $\pi/2$ pulse; (c) a schematic of the π, τ, $\pi/2$ pulse sequence that constitutes the inversion recovery T_1 measurement technique; (d) the initial amplitude of the FID after the π, τ, $\pi/2$ pulse sequence, which is proportional to the value of magnetization M at time τ, is plotted as a function of τ

magnetization in time and thereby measure the spin-lattice relaxation time T_1 accurately.

In the remainder of this chapter, a brief description of the actual measurement procedure is presented. First of all, the desired sample temperature is set. As described in the preceding chapter, the sample temperature is set and regulated by the temperature control unit consisting of potentiometer, null detector, power supply for the 15Ω heater coil and the cold or hot nitrogen gas flow rate. After the indicator of the null detector shows the desired sample temperature has been reached, another fifteen to thirty minutes is usually allowed to elapse in order to ensure that thermal equilibrium is achieved throughout the entire sample.

By using the Hewlett Packard 4815-A RF vector impedance meter, the probe is tuned to 50Ω and 0^{o} phase so that power from the transmitter is most efficiently coupled to the sample coil and to maximize the signal output from the sample coil. This is done by adjusting the two adjustable capacitors to achieve a match to the characteristic impedance of the coaxial cable from the duplexer at 40MHz. After the probe is tuned at the required sample temperature, the next step is to examine the pulse widths for π and $\pi/2$ pulses.

The π and $\pi/2$ pulses are applied in channel one and channel two, respectively, of the pulse programming unit. The pulse widths are obtained by setting the continuously adjustable controls on the respective channels. Typical values for the pulse widths in this

investigation of lanthanum and yttrium dihydrides are approximately 2.8 μs and 5.5 μs for π/2 and π pulses, respectively. The actual value of the pulse width varies from sample to sample, but it is temperature independent over most of the temperature range. However, for very high temperature, T>650K, the pulse widths do increase slightly with increasing temperature.

To select an appropriate value for the time interval τ between the π and π/2 pulses, and a suitable repetition time between successive pulse sequence, the proton spin-lattice relaxation time, T_1, must first be estimated. This estimation can be carried out by noting the time required for the Z-component of magnetization M_z to recover from its initial value of $-M_o$ to zero. Recalling Equation (4-9),

$M_z = M_o[1-2\ \exp(-\tau/T_1)]$, we see that for zero magnetization, $M_z \overset{\sim}{=} 0$ and $\tau = \tau_o$, one obtains

$$1-2\ \exp(-\tau_o/T_1) \overset{\sim}{=} 0,$$

$$\exp\ (-\tau_o/T_1) \overset{\sim}{=} \frac{1}{2}.$$

Hence, $$T_1 \overset{\sim}{=} \frac{\tau_o}{\ln 2}.$$

where τ_o is the time at which zero magnetization occurs.

After this estimate of T_1 is obtained, the time interval τ is set equal to approximately $T_1/100$. The repetition time between successive pulse sequences is set equal to $10T_1$ to ensure that full recovery of

the magnetization occurs before inversion by the next pulse sequence. By using the autoincrement module in the programmer, an appropriate time interval τ is chosen such that the condition $70\tau \leq T_1 \leq 120\tau$ is satisfied. There are then one hundred M_z values as a function of the time interval τ in each pass so that the τ value between π and $\pi/2$ pulses for the hundredth point satisfies the condition $0.8T_1 < \tau_{100} < 1.6T_1$. The main objective here is to ensure that the initial part of the magnetization recovery is enclosed in the one hundred point range. This is done because most of the relaxation information is contained in the early part of the recovery and to prevent the "near-equilibrium" region of magnetization recovery being included in the recovery data.

The number of complete passes of the magnetization recovery as a function of time that are required in order to obtain an accurate T_1 value is weakly temperature dependent. Usually, four passes suffice for each T_1 value at intermediate and low temperatures due to the greater Boltzmann factor, $\exp(2\mu H_o/k_B T)$. At elevated temperatures, $T > 660K$, sixteen or more passes of the magnetization recovery curve for a single T_1 value are not unusual because of the decreasing Boltzmann factor, weaker signals from the sample coil because of greater losses and hence smaller Q values, and increased thermal noise.

In order to extract the spin-lattice relaxation time T_1 from Equation (4-9), the M_o value must also be correctly measured. By setting the pulse width in channel one to a minimum value (corresponding to a 0^o pulse) so that the magnetization M_z will not be disturbed and

retaining the $\pi/2$ pulse in channel two, the M_o value can be measured. A single pass of one hundred points of M_o values is usually very adequate. The average of these one hundred M_o values is then substituted into Equation (4-9) to calculate the spin-lattice relaxation time T_1.

As described in the preceding chapter, T_1 was determined by using a Digital Equipment Corporation LSI-11 computer to make a least-squares fit of the data to Equation (4-9) in the form

$$\log\left(\frac{M_o - M_z(t)}{2M_o}\right) = -\frac{\tau}{T_1} .$$

Figure (4-4) shows a typical record plot made with the chart recorder and the data printed by the printer. It includes the magnetization recovery curve, the M_o value, the logarithm of $(M_o - M_z(t))$ and the least-squares fit. The slope of the fit gives the T_1 value.

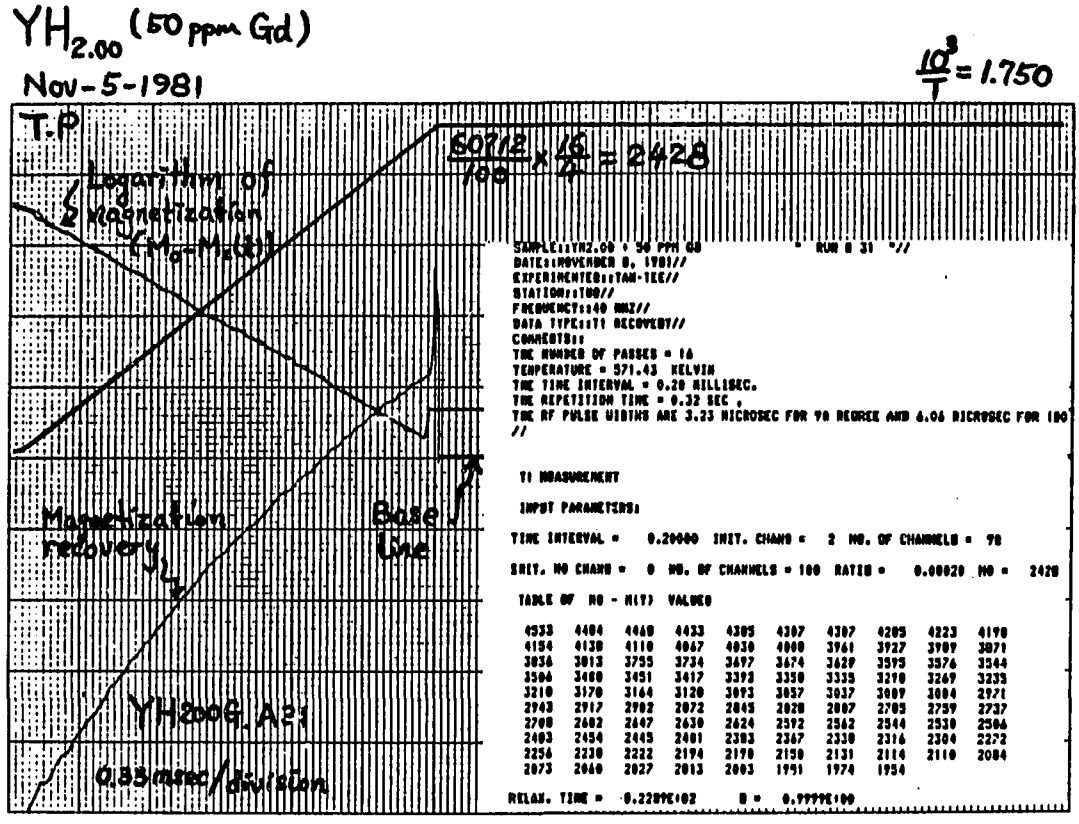

Figure 4-4. A typical plot made with the chart recorder, it consists of the magnetization recovery curve as a function of time interval τ, the M_o value, the logarithm of $(M_o-M_z(t))$ and the least-squares fit

V. RESULTS AND DISCUSSION

When this investigation of lanthanum and yttrium hydrides was begun the objective was to determine the effects of octahedral interstitial site occupancy on hydrogen diffusion via the temperature dependence of the proton T_1. In lanthanum hydride, LaH_x, with $1.9 \leq x \leq 2.5$, O-site occupancy must certainly occur. In the case of yttrium dihydride, YH_x, with $1.8 \leq x \leq 2.05$, both wide-line NMR and neutron scattering measurements made on Ames Laboratory samples showed that significant O-site occupancy occurs even before the $x = 2$ hydrogen concentration is reached. Indeed, at $x = 2.0$, about 12% of the O-sites are occupied at $T = 200K$. Thus, it was anticipated that evidence of O-site occupancy would be found in the T_1 behavior, particularly if starting materials (i.e., La and Y metal) of high purity were used. The presence of substantial levels of paramagnetic impurities was recognized by Schreiber and Cotts (47) in their original study of the lanthanum hydrides (e.g., in the depression of T_1 at low temperatures). It was felt that with pure materials an indication of a secondary (subsidiary) minimum in T_1 would be revealed, corresponding to hydrogen motion on the octahedral sublattice. Such behavior had indeed been found recently in the layered structure hydrides $ZrClH_{0.5}$ and $ZrBrH_{0.5}$ (48) in which hydrogen occupies predominantly the T-sites within the Zr metal bilayers, with some ($\sim$5%) occupancy of the O-sites.

However, as will become evident in the following presentation of

experimental results, the effects of paramagnetic impurities are, in fact, more pervasive and insidious than had been appreciated. The scope of the investigation, therefore expanded in an attempt to gain an understanding of (or at least to delineate) these effects as well as to determine the role of O-site occupancy (if any).

Accordingly, data sets of proton spin-lattice relaxation times were obtained for several series of lanthanum and yttrium hydrides, both with and without controlled levels of paramagnetic impurity ion content. These measurements were carried out using the pulsed NMR spectrometer that has been described in Chapter III. Spark source mass spectrometric analyses of the La and Y metals used in these hydrides are given in the Appendix. Summaries of the hydride systems studied are given in Tables 1-1 and 1-2. The relaxation times were determined in the temperature range from 77K to 800K at a frequency of 40MHz throughout the entire investigation. In the following sections, the experimental results and discussion have been organized into sections according to the categories in Tables 1-1 and 1-2.

A. "Pure" Lanthanum Hydrides LaH_x, $1.8 \leq x \leq 2.46$

Measurements of the proton spin-lattice relaxation time on a series of "pure" lanthanum hydrides LaH_x with $x = 1.80$, 2.00, 2.15, 2.27, 2.38 and 2.46, are presented and discussed in this section. These lanthanum hydrides were made from several different batches of lanthanum metal as follows: La-102877 was used for $x = 2.15$, 2.27, 2.46; La-8679 for $x = 2.00$ and 2.38; and La-112078 for $x = 1.80$ (see Appendix).

A summary plot of the proton T_1 values on a logarithmic scale versus reciprocal temperature for these hydrides is shown in Figure 5-1. Over the entire temperature range, from 77K to 800K, the values of the proton T_1 are much higher than those reported by Schreiber and Cotts (47) on comparable lanthanum hydride compositions. More significantly, the values of T_1 increase as the temperature decreases in the low temperature region, in contrast to Schreiber and Cotts' data which show T_1 decreasing with decreasing temperature. This observation shows that the Ames Laboratory samples have not been contaminated by high levels of paramagnetic impurities, in good agreement with the spark source mass spectrometric analyses. In Figure 5-1, it is seen that the results for $LaH_{1.80}$ and $LaH_{2.00}$ are very close to each other, suggesting that these two samples have, in fact, nearly identical hydrogen concentrations. The same observation applies to the cases of $LaH_{2.38}$ and $LaH_{2.46}$.

As the temperature increases, the thermally activated diffusive motion of the hydrogen becomes more rapid. As has been outlined in Chapter II, the spin-lattice relaxation rate is directly related to the spectral density function, $J(\omega_0, \tau)$, of the dipolar field fluctuations so that a minimum spin-lattice relaxation time occurs when the hydrogen jumping frequency approximately equals the Larmor precession frequency. Figure 5-1 shows that the temperature of the minimum spin-lattice relaxation time, $T_{1,min}$, decreases as the concentration of hydrogen increases. This at once implies that hydrogen diffuses

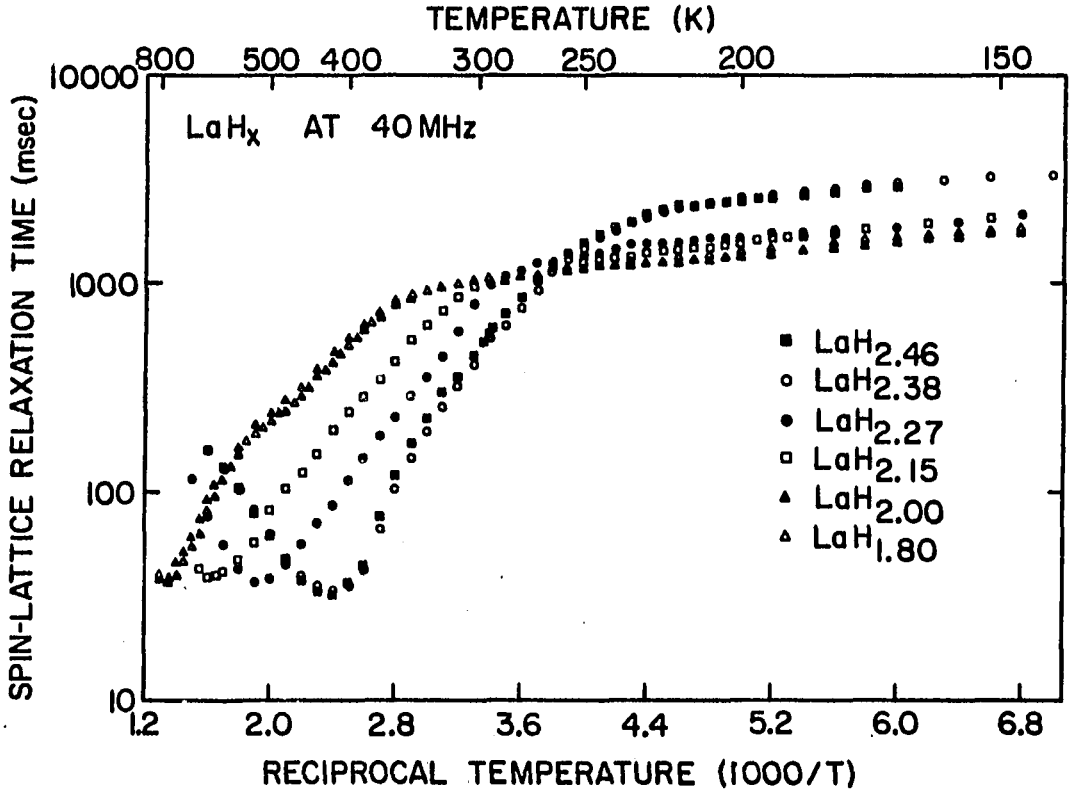

Figure 5-1. The logarithm of the proton spin-lattice relaxation time T_1 at 40MHz versus reciprocal temperature (1000/T) for various hydrogen concentrations of LaH_x

faster (at a fixed temperature) as the concentration of hydrogen increases. Such behavior is very different from that in the majority of other metal-hydrides reported, e.g., TiH_x (14), ZrH_x (49), HfH_x (50), and TaH_x (51), in which hydrogen diffusion decreases with increasing hydrogen content. In addition, the value of $T_{1,min}$ in LaH_x decreases as the hydrogen concentration increases, as expected from Equation (2-17).

In the cases of $LaH_{1.8}$ and $LaH_{2.00}$, the curves of T_1 vs $10^3/T$ show an obvious although very weak subsidiary minimum or "slope-change" on the low temperature side of the principal diffusion minimum. Similar behavior had been reported and interpreted as due to a change in the hydrogen diffusion mechanism by other workers in the cases of ScH_x (10) and ZrH_x (49). It will be shown later in this study that such an interpretation may very well be in jeopardy. A clear and convincing "slope-change" was not observed for the $LaH_{2.15}$ and $LaH_{2.27}$ samples; however, a straight line slope on the low temperature side of the main diffusion minimum was not obtained, and a slight residual curvature could be detected. The disappearance of the "slope-change" for the latter two samples may be due to the fact that different batches of lanthanum were used for the formation of these hydrides. An abrupt drop in the value of the proton T_1 within the temperature range $330K \leq T \leq 390K$, before the main T_1 minimum occurs, was observed for $LaH_{2.38}$ and $LaH_{2.46}$. Such behavior may be a different manifestation of the "slope-change" phenomenon seen in the $LaH_{1.80}$ and $LaH_{2.00}$ samples.

In the low temperature region, the thermally activated motion of the hydrogen slows down; thus, the proton spin-lattice relaxation rate T_1^{-1} is sharply decreased. This region is called the rigid-lattice regime. Here, the contribution to the spin-lattice relaxation rate from the dipole-dipole interaction due to the hydrogen diffusion becomes negligible, and the contributions from conduction electrons and paramagnetic impurity ions begin to dominate and compete with each other. The spark source mass spectrometric analyses show that these hydride samples are very "pure". Hence, the contribution from paramagnetic impurity ions must be weak and can be temporarily deferred for consideration later. The relaxation mechanism due to the conduction electrons is the major contributor in this regime, whereas in the work of Schreiber and Cotts, paramagnetic impurity relaxation dominated.

Figure 5-2 shows a plot of the low temperature T_1 values on a linear scale versus reciprocal temperature for the $LaH_{2.15}$ sample. As expected, Korringa behavior is observed with a Korringa product, $K = T_1T = 311$ sec-K. The value of the Korringa product is constant in the temperature range shown ($160K \leq T \leq 300K$). This result stands in marked contrast to the temperature dependent Korringa product reported for TiH_x (52,53), and for ZrH_x (49). All indications point in the direction that the conduction electron contribution to relaxation dominates in the temperature range shown, and there is no sign that paramagnetic impurity ions are effective in this temperature range.

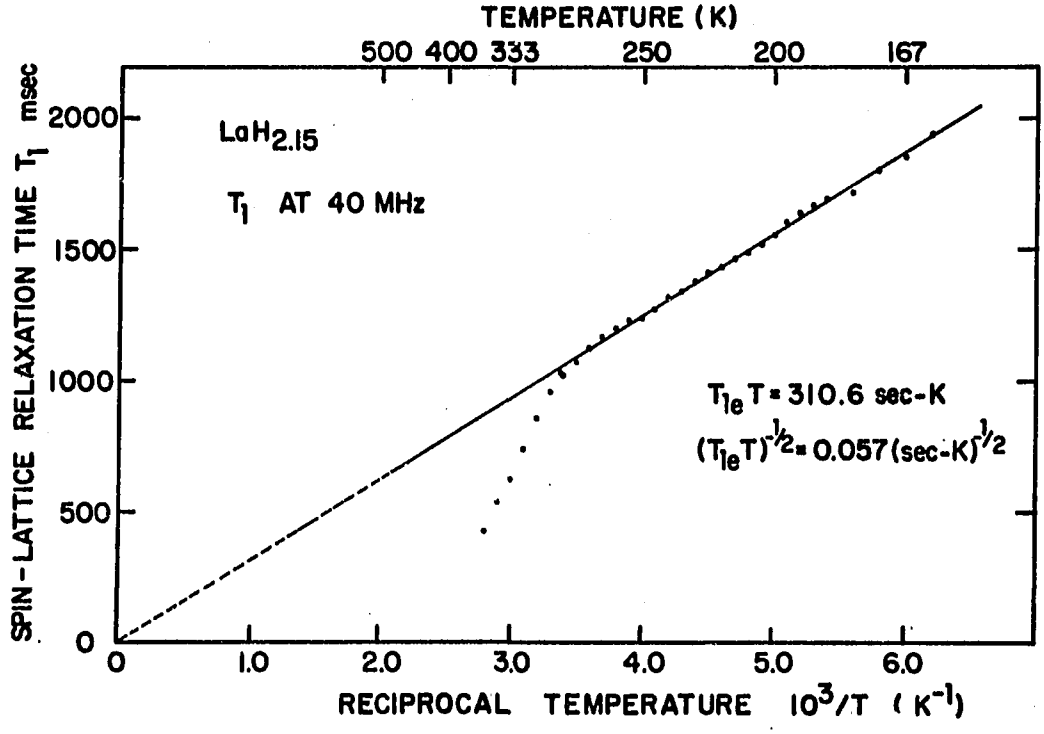

Figure 5-2. Proton spin-lattice relaxation time T_1 versus reciprocal temperature (1000/T) for $LaH_{2.15}$. The solid line is a linear least-squares fit to the data below 280K. The slope of the line gives Korringa constant K = 310.6 sec-K

For the remainder of the hydride samples in this series, slightly different Korringa products were obtained. For each sample, the Korringa product increases with decreasing temperature before reaching a maximum value. After the occurrence of the maximum, the product decreases with further decreasing temperature. It is worth noting that the value of T_1 itself continues to increase with decreasing temperature, so that a graph of T_1 versus T shows no obvious indication of any contribution from paramagnetic impurity ions in this temperature region. However, the occurrence of a maximum Korringa product as a function of temperature for the remaining hydride samples definitely indicates the presence of some residual paramagnetic impurities (perhaps 1 ppm or less), as will become evident later. For these hydrides, the average Korringa product within an appropriate temperature range in the vicinity of the maximum product is tabulated in Table 5-1. These Korringa products can be used to estimate the electronic density of states at the Fermi level, since as outlined in Chapter II the Korringa product is directly related to the electronic density of states at the Fermi level $N(E_F)$ by the relation $N(E_F) \propto (T_{1e}T)^{-1/2}$. Clearly, the values of $N(E_F)$ decrease slightly with increasing hydrogen concentration for $1.8 \leq x \leq 2.27$; however, as seen in Figure 5-3, $N(E_F)$ shows an abrupt turndown for $LaH_{2.38}$ and $LaH_{2.46}$. In simple terms, the behavior of $(T_{1e}T)^{-1/2}$ versus x implies that $N(E_F)$ decreases with increasing hydrogen concentration for LaH_x with values of $x \leq 2.46$.

Table 5-1. The Korringa products for lanthanum hydrides LaH_x. The values are averages over temperature ranges in the vicinity of the maximum products

X	K (sec-K)[a]	$(T_{1e}T)^{-1/2}$ (sec-K)$^{-1/2}$[b]
1.80	290	0.059
2.00	305	0.058
2.15	310	0.057
2.27	325	0.056
2.38	505	0.045
2.46	495	0.045

[a]Typical uncertainty is about ±3%.

[b]Typical uncertainty is about ±2%.

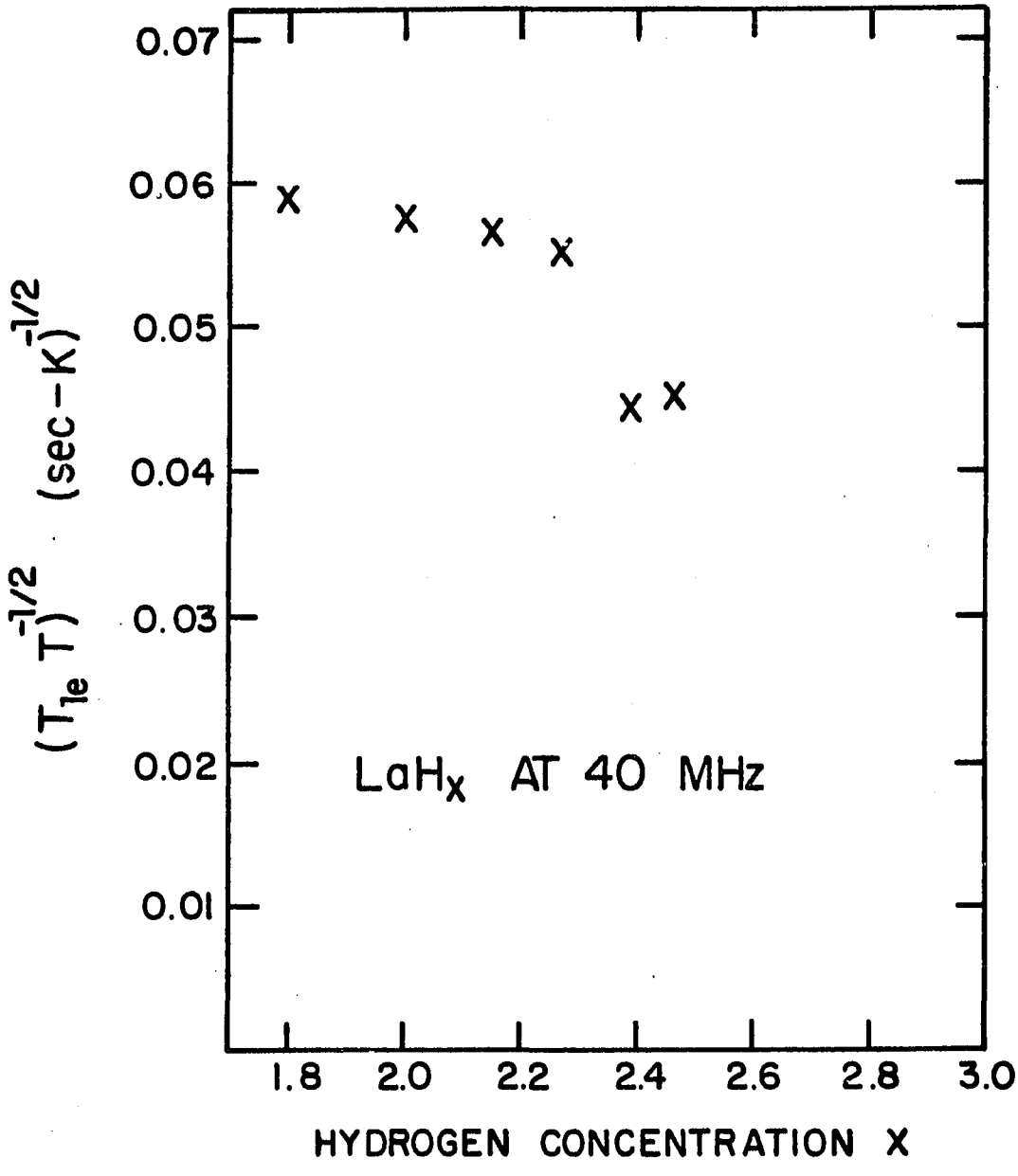

Figure 5-3. Plot of $(T_{1e}T)^{-1/2}$ as a function of hydrogen concentration for LaH_x with $x < 2.50$. The values of $T_{1e}T$ are the averages of Korringa products in the vicinity of the maximum for each hydride

The simple BPP model described in Chapter II was adopted to interpret the experimental spin-lattice relaxation rate due to hydrogen diffusion. Together with the Korringa rate, T/K, and by using Equation (2-17) with Equations (2-14) to (2-16), one obtains,

$$\frac{1}{T_1} = \frac{1}{1.425\ T_{1,min}} \left[\frac{\omega_0\tau_C}{1+(\omega_0\tau_C)^2} + \frac{4\omega_0\tau_C}{1+4(\omega_0\tau_C)^2}\right] + \frac{T}{K}\ , \qquad (5\text{-}1)$$

and $\tau_C = \frac{1}{2}\tau_D$,

where $\tau_D = \tau_{D,0}\ \exp(E_{act}/k_B T)$.

This accounts for the proton-proton interaction and neglects the lanthanum-proton interaction which is relatively smaller. The values of activation energy, E_{act}, the attempt frequency, $\nu_0 = \tau_{D,0}^{-1}$ and the hydrogen jump frequency as function of temperature, $\nu(T) = \tau_D^{-1}(T)$, were determined by a least-squares fit of Equation (5-1) to the measured T_1 values. The results are tabulated in Table 5-2. Because of the features of the $T_1(T)$ curves already mentioned, not too much reliance should be placed on the precise values of E_{act} and ν_0, and attention is directed instead to the values of the jump frequency ν at a fixed temperature. The table shows that at 300K, ν increases as hydrogen concentration increases (a point already noted on the basis of the temperature of $T_{1,min}$). This observation had already been reported for lanthanum

Table 5-2. Diffusion parameters : activation energy E_{act}, attempt frequency ν_0, jump frequency at 300K ν(300K), for hydrogen in LaH_x obtained using a single BPP function

X	E_{act} (eV/atom)	ν_0 $(sec)^{-1}$	ν (300K) $(sec)^{-1}$
1.80	0.45	4.5×10^{10}	1.4×10^{3}
2.00	0.40	1.4×10^{10}	2.8×10^{3}
2.15	0.31	1.5×10^{10}	1.1×10^{5}
2.27	0.34	1.2×10^{11}	2.4×10^{5}
2.38	0.35	7.7×10^{11}	9.1×10^{5}
2.46	0.37	1.1×10^{12}	7.1×10^{5}

hydrides by Schreiber and Cotts almost 20 years ago. This result is surprising as one might expect hydrogen diffusion to slow down as more hydrogen is introduced, due to a simple site-blocking effect. However, this view contradicts what is observed.

In order to aid in understanding this striking observation, the sizes of octahedral (O) and tetrahedral (T) interstitial sites, and the spacing between O and T sites for some of the transition metal dihydrides are tabulated in Table 5-3. The trihydride phase MH_3 has never been obtained for transition metals for which the spacing between T-sites and O-sites, d_{T-O}, in the metal is shorter than 2.10Å. Regarding such hydrides, the octahedral interstitial sites are evidently not energetically accessible for hydrogen occupancy. The O-sites become available only in those metals in which d_{T-O} is larger than 2.10Å. Hence, an effective repulsive force between two hydrogens plays an important role in the accessibility of the O-sites. As the distance between O and T sites decreases, the repulsive force becomes stronger with the result that the O-sites cannot be occupied when d_{T-O} is shorter than 2.10Å. The trihydrides MH_3 have been obtained for those metals in which $d_{T-O} >$ 2.10Å, i.e., La, Ce, Pr, Nd, Lu and Y; however, while LaH_3, CeH_3, PrH_3 and NdH_3 retain the fcc structure, LuH_3 and YH_3, for which d_{T-O} is not much larger than the "critical" value, do not.

The proton spin-lattice relaxation times for TiH_x as a function of temperature were studied by Korn and Zamir (14), who reported that hydrogen diffusion slowed down (at a constant temperature) with

Table 5-3. Interstitial hole sizes and spacings in the metal dihydride phase (MH_2) for some transition metals

M	a_0 (Å)	Diameter		T-O distance
		T-site (Å)	O-site (Å)	d_{T-O} (Å)
Sc	4.738	0.75	1.39	2.05
Ti	4.447	0.70	1.30	1.92
Y	5.204	0.82	1.53	2.25
Zr	4.603	0.73	1.35	1.99
La	5.661	0.89	1.66	2.45
Ce	5.580	0.88	1.64	2.42
Pr	5.515	0.87	1.62	2.39
Nd	5.469	0.86	1.60	2.37
Lu	5.033	0.80	1.47	2.18
Hf	4.710	0.74	1.38	2.04

increasing hydrogen concentration as x increases towards the value 2. Similar behavior had also been reported in ScH_x (38) and ZrH_x (49). In these hydrides the distance d_{T-O} is less than the critical value 2.10Å, and these metals do not form a trihydride phase. In other words, the O-sites are not accessible for hydrogen occupancy. In contrast, the opposite behavior was observed in this study of lanthanum hydrides and of lutetium hydrides (54) in another study.

If for $x \leq 2$ only T-sites were occupied, then diffusion would become very slow as $x = 2$ is approached because of a blocking factor $(2-x)$. The availability of O-sites clearly avoids this. But further, it appears that O-sites become more readily accessible for jumps as more hydrogen is introduced beyond $x = 2$, since the jump frequency continues to increase. Perhaps the increase in lattice constant and/or change in the screening due to the change in electron density as x is increased greatly reduce the proton-proton repulsion. An analogous situation may exist in bct β-VH_x (17) where the diffusion rate increases (and activation energy decreases) as x increases. In this case, it seems that adding hydrogen encourages occupation of "minority" O_{z_2} sites and lowers the barrier to diffusion among the "majority" O_{z_1} sites.

These observations imply that accessibility of O-sites enhances hydrogen diffusion in fcc phases. Since for yttrium metal the distance d_{T-O} is greater than the critical value, and a trihydride phase is formed (although not cubic), we may anticipate that results similar to those in LaH_x will be obtained for yttrium dihydrides, YH_x.

B. "Pure" Yttrium Hydrides YH_x, $1.81 \leq x \leq 2.03$

Unlike the lanthanum hydrides described in the preceding section, a series of yttrium hydrides, YH_x, with increasing hydrogen concentration ($x = 1.81, 1.91, 1.98, 2.03$) were prepared from a single piece of yttrium metal, Y-12979-W. The proton spin-lattice relaxation times for these hydrides were also measured over the temperature range from 77K to 800K. A composite plot of log T_1 against reciprocal temperature is shown in Figure 5-4. Basically, the behavior of the $T_1(T)$ curves is similar to that in the lanthanum hydrides. Compared to the results reported by Kashaev et al. (12), the values of the proton T_1 obtained in this study are much longer in the low temperature range (rigid-lattice regime). This observation shows that considerable levels of paramagnetic impurities were present in the samples studied by Kashaev et al. (12).

At higher temperatures (motional-narrowing region), the spin-lattice relaxation mechanism results mainly from the dipole-dipole interaction between protons as hydrogen diffusion becomes increasingly rapid. Yttrium-hydrogen dipolar interactions are negligible. All of these hydrides show a definite subsidiary minimum on the low temperature side of the principal T_1 minimum which is due to hydrogen diffusion. The temperature at which the subsidiary minimum occurs decreases with increasing hydrogen concentration. However, the strengths of the subsidiary minima (i.e., T_1^{-1}) are almost independent of hydrogen concentration. It is important to note that the strength (depth) of

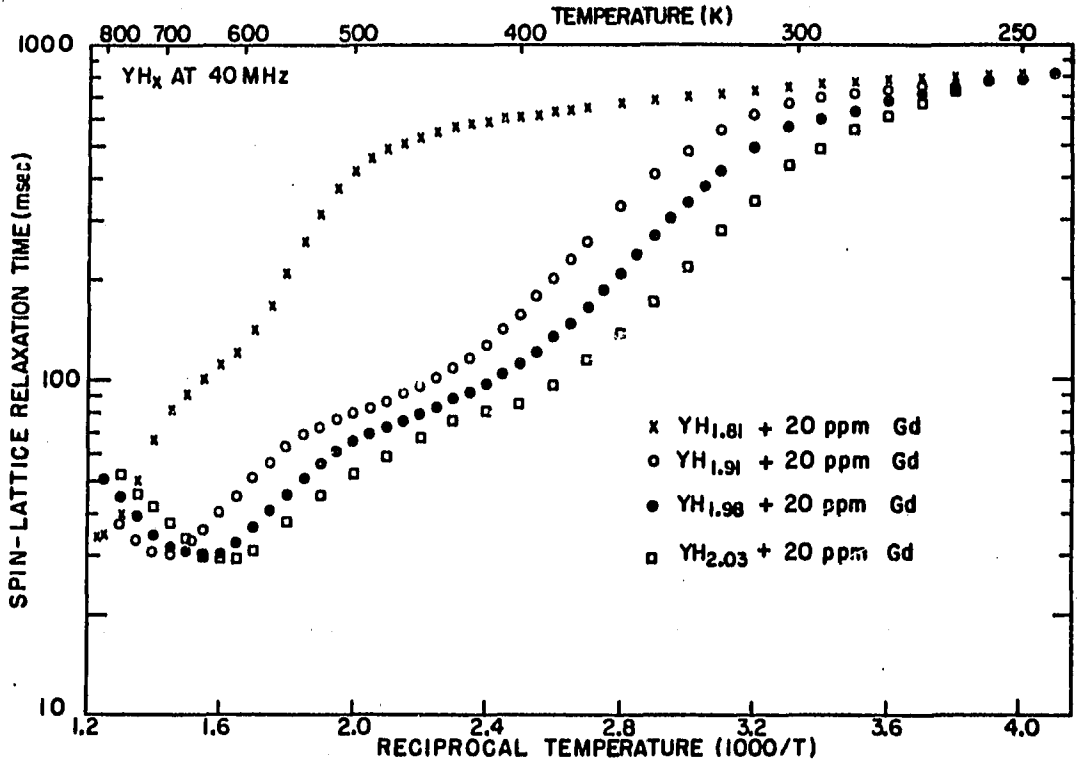

Figure 5-4. A composite plot of log T_1 versus reciprocal temperature $10^3/T$ for a series of YH_x with different hydrogen concentrations. A single piece of yttrium metal, Y-12979-W, was used. A subsidiary minimum is observed for all samples

these secondary minima in the yttrium dihydrides is much greater than in the lanthanum hydrides (previous section). This result is surprising since it was supposed (see below) that the secondary minima were a consequence of O-site hydrogen occupancy. Obviously, O-site occupancy must be greater in, say, $LaH_{2.27}$ than in $YH_{1.91}$, yet the subsidiary minimum is much more pronounced in the latter than in the former. At first it was thought that this behavior must reflect some difference in hydrogen diffusion in the two systems.

For the principal minimum, the temperature of the minimum (T_{min}) decreases with increasing hydrogen concentration. This indicates again that the hydrogen jump frequency increases as hydrogen concentration increases. This observation is exactly similar to that for the lanthanum hydrides. Thus, it matches very well the prediction made in the previous section. Again, the values of $T_{1,min}^{-1}$ are approximately proportional to hydrogen concentration as expected from Equation (2-17).

When these measurements were made, it appeared not unreasonable to assume that the hydrogen occupying the octahedral interstitial sites was the major contributor to the subsidiary minimum in these hydrides. Both NMR (19) and neutron scattering (20) studies reported premature occupancy of O-sites in yttrium dihydride. Therefore, a double-BPP function model (sum of two single BPP functions) was initially employed to interpret the experimental T_1 data showing such double minimum character. Recall Equation (1-1),

$$(T_1)^{-1} = (T_{1d})^{-1} + (T_{1e})^{-1} + (T_{1p})^{-1}.$$

Neglecting the contribution from paramagnetic impurity ions, one obtains the net relaxation rate,

$$(T_1)^{-1} = (T_{1d})^{-1} + (T_{1e})^{-1}, \tag{5-2}$$

where the rates $(T_{1d})^{-1}$ and $(T_{1e})^{-1}$ are again the contributions from hydrogen diffusion and conduction electrons, respectively. For the single-BPP function, we have, as usual,

$$(T_{1d})^{-1} = \frac{1}{1.425\ T_{1,min}} \left[\frac{\omega_0\tau_C}{1+(\omega_0\tau_C)^2} + \frac{4\omega_0\tau_C}{1+4(\omega_0\tau_C)^2}\right]. \tag{5-3}$$

The sum of two single-BPP functions is therefore given as,

$$(T_{1d})^{-1} = (T_{1d})_T^{-1} + (T_{1d})_O^{-1},$$

$$(T_{1d})^{-1} = \frac{1}{1.425\ T_{1T,min}} \left[\frac{\omega_0\tau_{C,T}}{1+(\omega_0\tau_{C,T})^2} + \frac{4\omega_0\tau_{C,T}}{1+4(\omega_0\tau_{C,T})^2}\right]$$

$$+ \frac{1}{1.425\ T_{1O,min}} \left[\frac{\omega_0\tau_{C,O}}{1+(\omega_0\tau_{C,O})^2} + \frac{4\omega_0\tau_{C,O}}{1+4(\omega_0\tau_{C,O})^2}\right], \tag{5-4}$$

which may be used in Equation (5-2) for the net relaxation rate with $(T_{1e})^{-1} = T/K$; K = Korringa constant. The assumption that the rates

$(T_{1d})_T^{-1}$ and $(T_{1d})_O^{-1}$ are additive implies that there exists a common spin temperature and a single T_1 for all protons on both T and O-sites. This is consistent with the fact that in all of these measurements only exponential magnetization recoveries, and single T_1's, were observed. This is not unreasonable, since the T and O-site sublattices are, in fact, interpenetrating sublattices, so that the nearest neighbors of each species are on the other sublattice. We assume that $\tau_{D,O} << \tau_{D,T}$ and that relaxation due to O-O dipolar interaction is negligible. Then $(T_{1d})_T^{-1}$ can be interpreted as the relaxation rate due to T-T interactions, and $(T_{1d})_O^{-1}$ as that due to O-T interactions. In this case, $\tau_{C,T} = \frac{1}{2}\tau_{D,T}$ and $\tau_{C,O}^{-1} = \tau_{D,O}^{-1} + \tau_{D,T}^{-1} \simeq \tau_{D,O}^{-1}$.

The values of the activation energies, minimum spin-lattice relaxation times, and jump frequencies obtained by fitting this double-BPP formulation to the data of Figure 5-4 are summarized in Table 5-4. In general, the fits that were obtained in this manner using Equation (5-4) agreed excellently with the experimental values. The results of these fits are shown in Figures 5-5 to 5-8.

It can be shown that in this model, the ratio of the maximum relaxation rates $(T_{1T,min})^{-1}$ and $(T_{1O,min})^{-1}$ is related to the ratio of hydrogen occupancies in T and O-sites, but weighted by the ratio of the second moments M_{TT}, M_{OT} associated with T-T and O-T dipolar interactions. The results in Table 5-4 show that approximately 7% to 13% of octahedral interstitial sites are occupied in the temperature region around the T_1 minima, with very little change between the samples with

Table 5-4. Diffusion parameters and the percentage of O-site occupancy for hydrogen in YH_x. The hydrogen concentration $x = 2\beta+\alpha$; α and β represent the probability of occupancy for O and T-sites, respectively, then $R = \frac{\beta}{\alpha}\frac{M_{TT}}{M_{OT}}$ with $\frac{M_{TT}}{M_{OT}} = 0.407$ for YH_2

	Activation energy (eV)		Minimum T_1 (ms)	
X	E_O	E_T	$T_{1O,min}$	$T_{1T,min}$
1.81	0.705	0.857	191	39.3
1.91	0.289	0.481	120	36.5
1.98	0.286	0.413	123	34.8
2.03	0.265	0.400	107	34.9

Jumping frequency (s^{-1})			
ν_0 (300K)	ν_T (500K)	$R = \frac{(T_{1T,min})^{-1}}{(T_{10,min})^{-1}}$	% of O-sites occupied
71.2	5.80×10^4	4.86	7
1.54×10^6	2.05×10^6	3.29	11
2.85×10^6	5.35×10^6	3.53	11
5.11×10^6	8.30×10^6	3.07	13

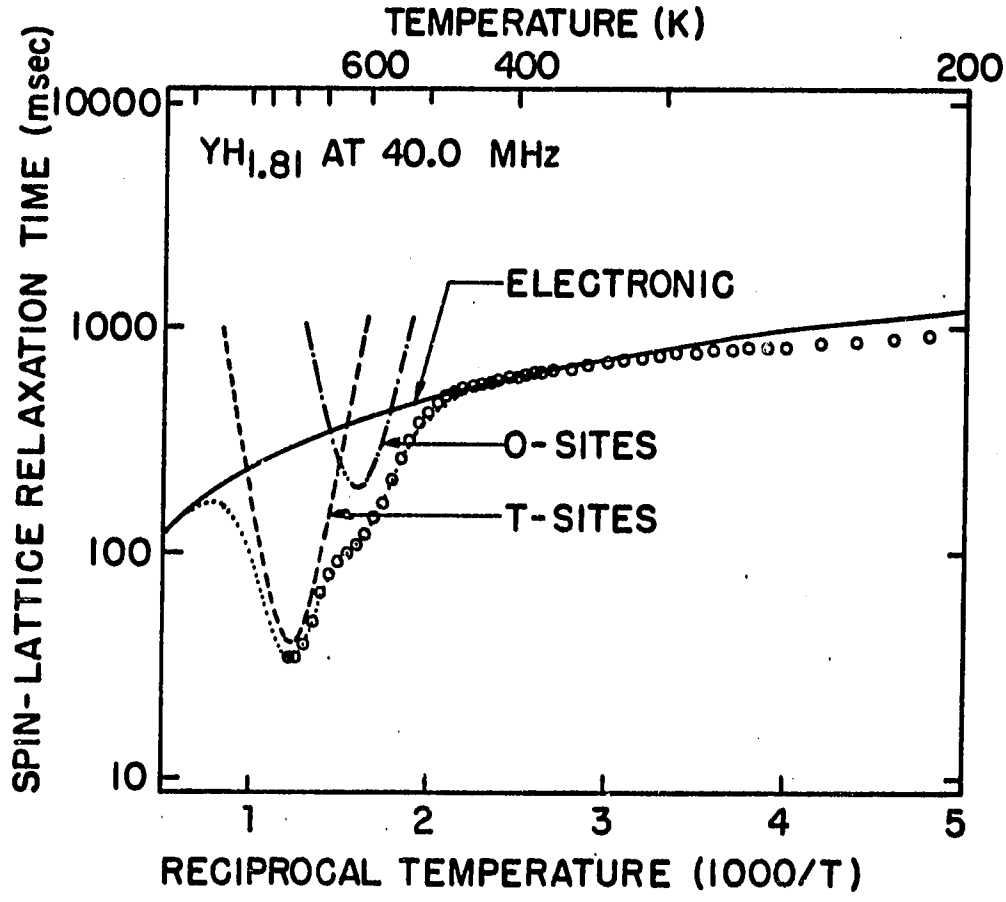

Figure 5-5. Logarithm of T_1 against $10^3/T$ in $YH_{1.81}$. The resolution of two minima (attributed to T-T interactions and O-T interactions) was carried out by using Equation (5-4) with the assumptions that $\tau_{D,O} \ll \tau_{D,T}$ and relaxation due to O-O dipolar interaction is negligible

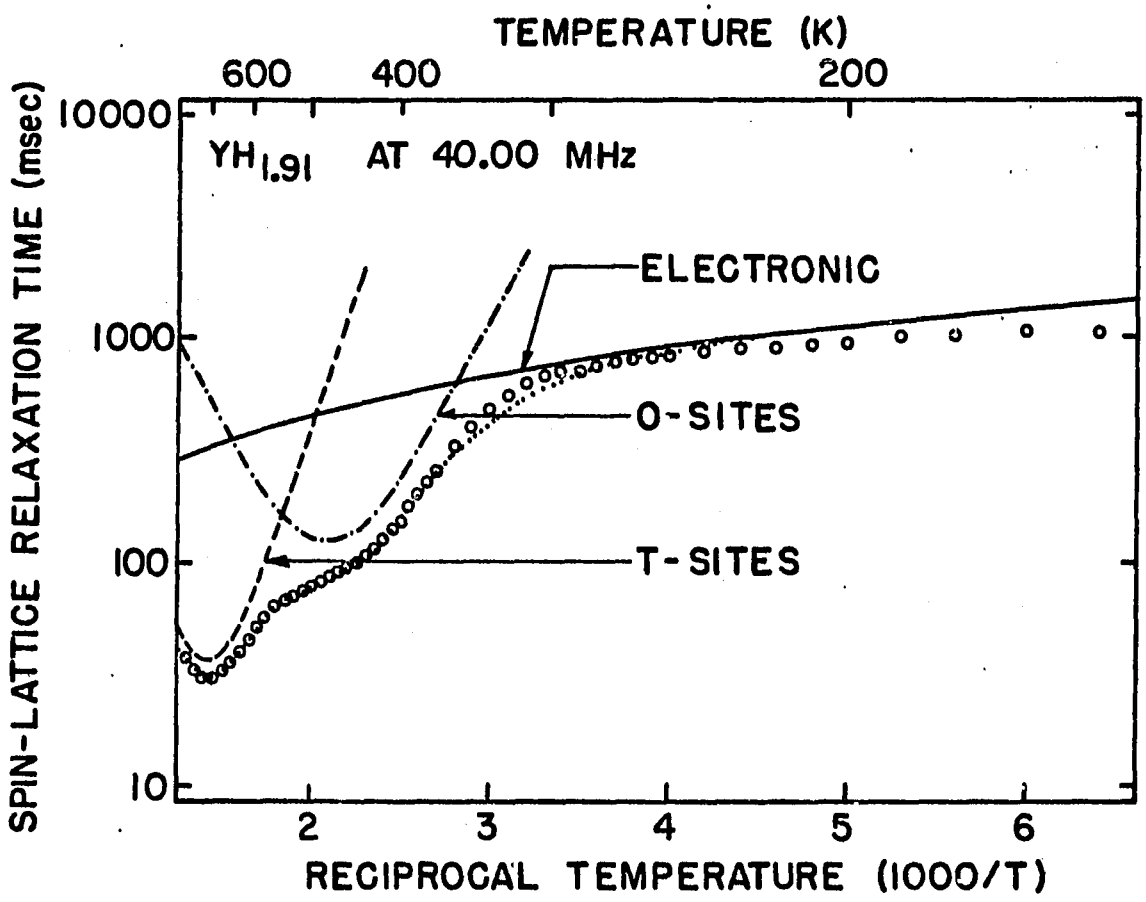

Figure 5-6. Plot of log T_1 against $10^3/T$ for $YH_{1.91}$. The higher temperature minimum (attributed to T-T interactions), lower temperature minimum (attributed to O-T interactions), and conduction electron contribution (solid line) are clearly shown

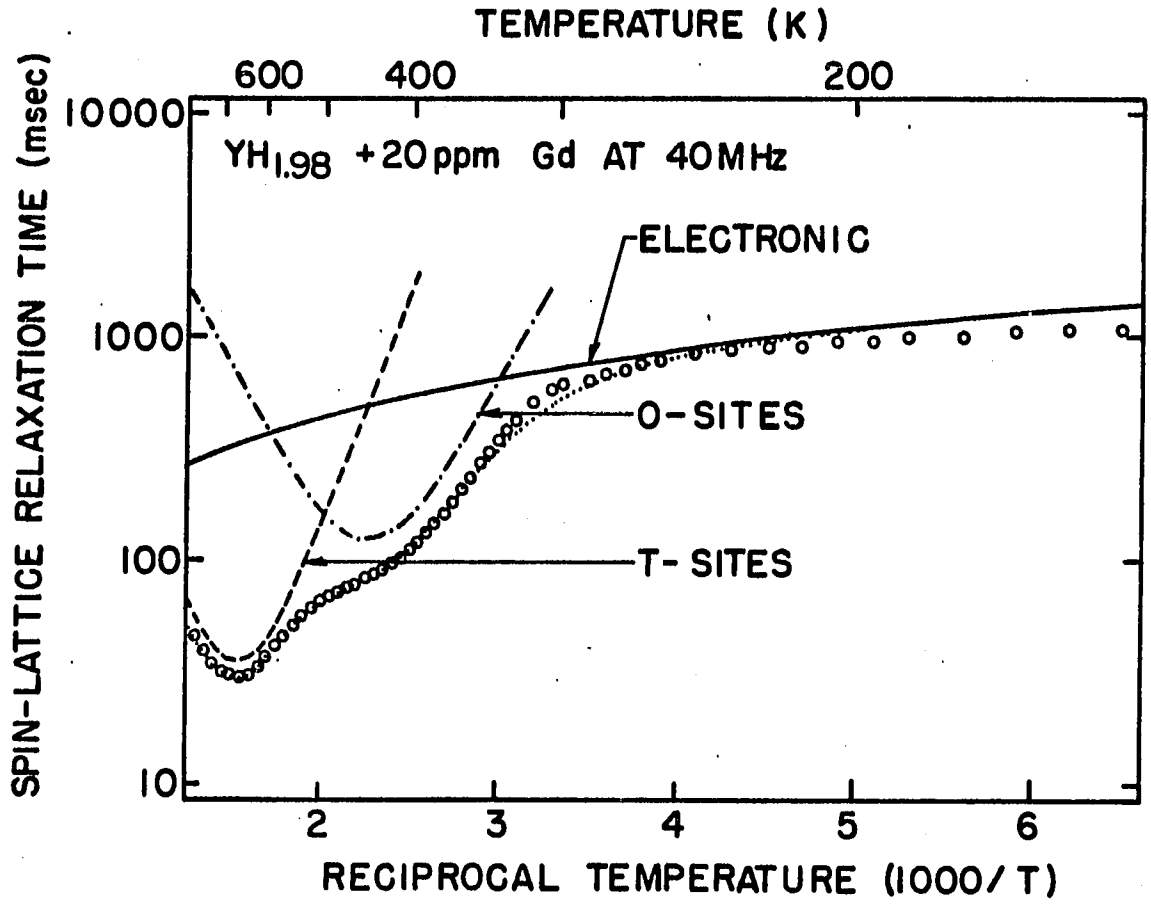

Figure 5-7. Logarithm of T_1 versus reciprocal temperature $10^3/T$ in $YH_{1.98}$ sample. The data were resolved into three additive relaxation rates, conduction electron contribution, subsidiary minimum due to O-T hydrogen interactions and the "main" minimum due to T-T hydrogen interactions

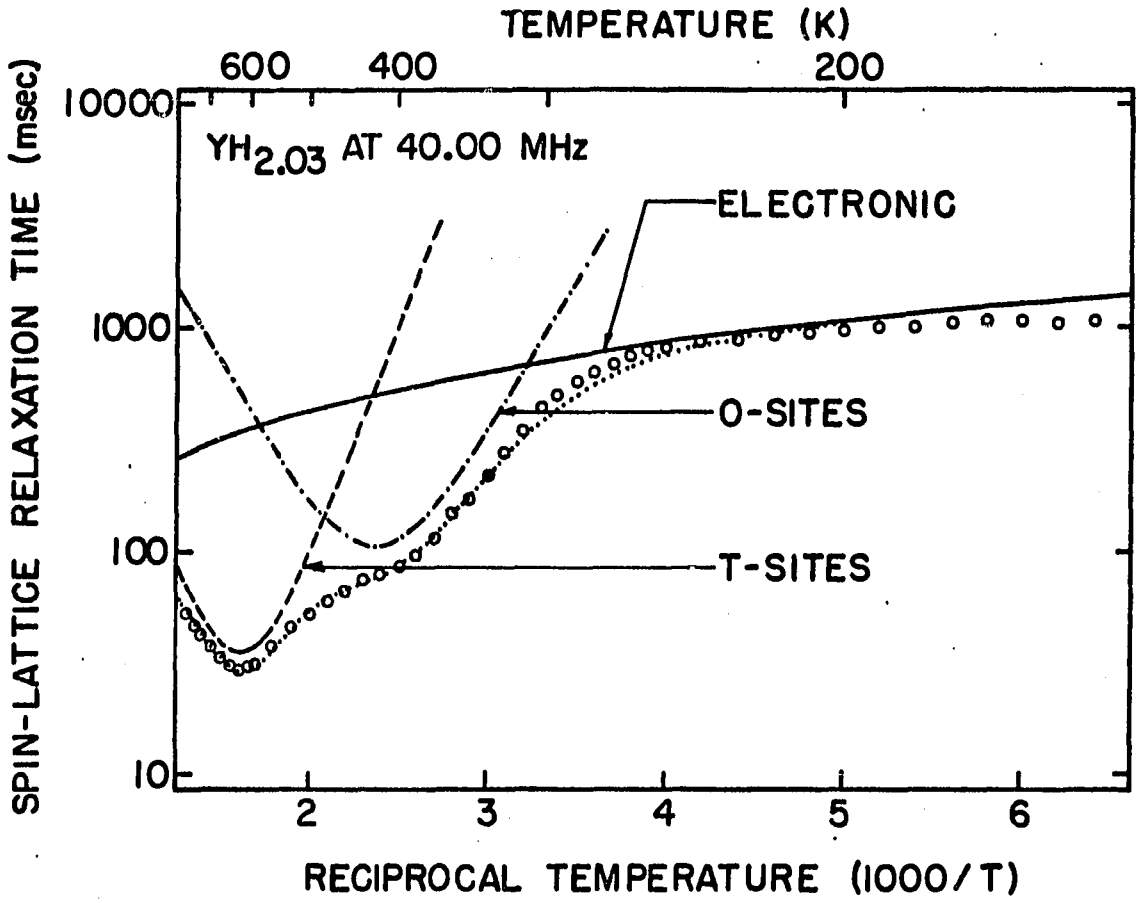

Figure 5-8. Resolution of log T_1 vs $10^3/T$ in $YH_{2.03}$. The same assumptions and equations as for previous figures, 5-5 to 5-7, were adopted

$x = 1.91$ to 2.03. These values are generally similar to those obtained from wide-line NMR (19) and neutron scattering (20) measurements, but the substantial increase in O-site occupancy between $x = 1.9$ and 2.0 shown by wide-line NMR is not reproduced. At this point some discrepancy therefore remained, together with the unexplained feature, already mentioned, that the subsidiary minima in this system are more marked than in the corresponding lanthanum hydrides. Rather than discuss this further here, another possibility for the origin of the subsidiary minimum will be discussed shortly.

As the temperature decreases, one enters the rigid-lattice regime from the motional-narrowing region, and hydrogen diffusion slows down. Consequently, the conduction electrons provide the major spin-lattice relaxation mechanism. As seen in Figure 5-4, (and confirmed by further lower temperature measurements) the values of proton T_1 in the rigid-lattice regime for all these hydride samples show signs of flattening out and becoming nearly temperature independent. However, the value of T_1 does increase slowly with decreasing temperature, even down to 77K. Table 5-5 lists the measurements of the proton T_1 at the lowest temperature ($T = 77K$) and also the Korringa products at this temperature. In the entire low temperature range, the Korringa product always increases to a maximum value and then decreases with further decreasing temperature. The average Korringa products, K, in the vicinity of the maximum value are also listed in Table 5-5. This table shows that the value of K decreases to about half its maximum value as the temperature

Table 5-5. Korringa products for YH_x, which are the averages in the appropriate temerpature range in the vicinity of the maximum product. The Korringa products at 77K are listed for comparison

X	T_1 (msec) at 77K	T_1T (sec-K)[a] at 77K	T_1T (sec-K)[a] T > 210K
1.81	1430	110	245
1.91	1370	105	205
1.98	1320	100	200
2.03	1230	95	200

[a]Typical uncertainty is about $\pm$3%.

decreases to T ≈ 77K. This decrease of the Korringa product was already mentioned in the preceding section for lanthanum hydrides. Once again, this may indicate the presence of paramagnetic impurity ions in the samples. In fact, by referring to the spark source mass spectrometric analysis listed in the Appendix, the major paramagnetic impurity is seen to be about 20 ppm of gadolinium. Although it seemed reasonable to ascribe the decrease of the Korringa product to the presence of 20 ppm of gadolinium, it seemed unlikely that so little Gd^{3+} could be responsible for the appearance of the subsidiary minimum as the temperature enters the motional-narrowing region. However, at this stage, there still appeared to be two possibilities for the origin of the subsidiary minimum: the effect of O and T-sites occupancies, and the effect of paramagnetic impurities.

In order to clear up this confusion and reach a clear understanding of the true origin of the subsidiary T_1 minimum, further investigation was needed. As a first step, measurements on a much purer yttrium hydride sample were carried out. By reducing the level of paramagnetic impurity as far as possible, it was hoped that any possible influence of the impurity could be ruled out.

C. The "Purest" $YH_{1.98}$ Versus "Pure" $YH_{1.98}$

A new yttrium dihydride sample, $YH_{1.98}$ was prepared from the purest yttrium metal available (Y-81180) in the Ames Laboratory. The proton spin-lattice relaxation times were again measured over the

temperature range, 77K to 800K, at the resonance frequency of 40MHz. The values of T_1 obtained are much longer than those for the "old" sample of $YH_{1.98}$ described in the preceding section throughout the entire temperature range. For the purpose of direct comparison, the proton spin-lattice relaxation times for the "old" and "new" hydrides, $YH_{1.98}$, are plotted in Figure 5-9. Not only are the low temperature T_1 values longer but the subsidiary minimum has essentially vanished. The principal difference between the two batches of yttrium metal used for these samples is the concentration of gadolinium impurity (see Appendix). It is remarkable that such a small increase in gadolinium impurity concentration at such a low level, from 2 ppm to 20 ppm, can be so effective in dominating the spin-lattice relaxation time T_1 over the entire temperature range, especially in the high temperature region.

A substantially larger Korringa product, K = 295 sec-K, was obtained for the "new" sample than that, K = 200 sec-K, for the "old" sample. This indicates that the electronic density of states at the Fermi level, $N(E_F) \propto (K)^{-1/2}$, is somewhat smaller than was previously estimated. Hence, even as little as 20 ppm of gadolinium impurity can lead to an incorrect estimation of the Korringa product. However, the most striking feature of the data is the disappearance of the subsidiary minimum for the "new" sample. The strength of the subsidiary minimum is so weak that it only appears as a form of "slope-change" in the same temperature region. As remarked in Chapter I and Section A in the present chapter, this "slope-change" feature had been

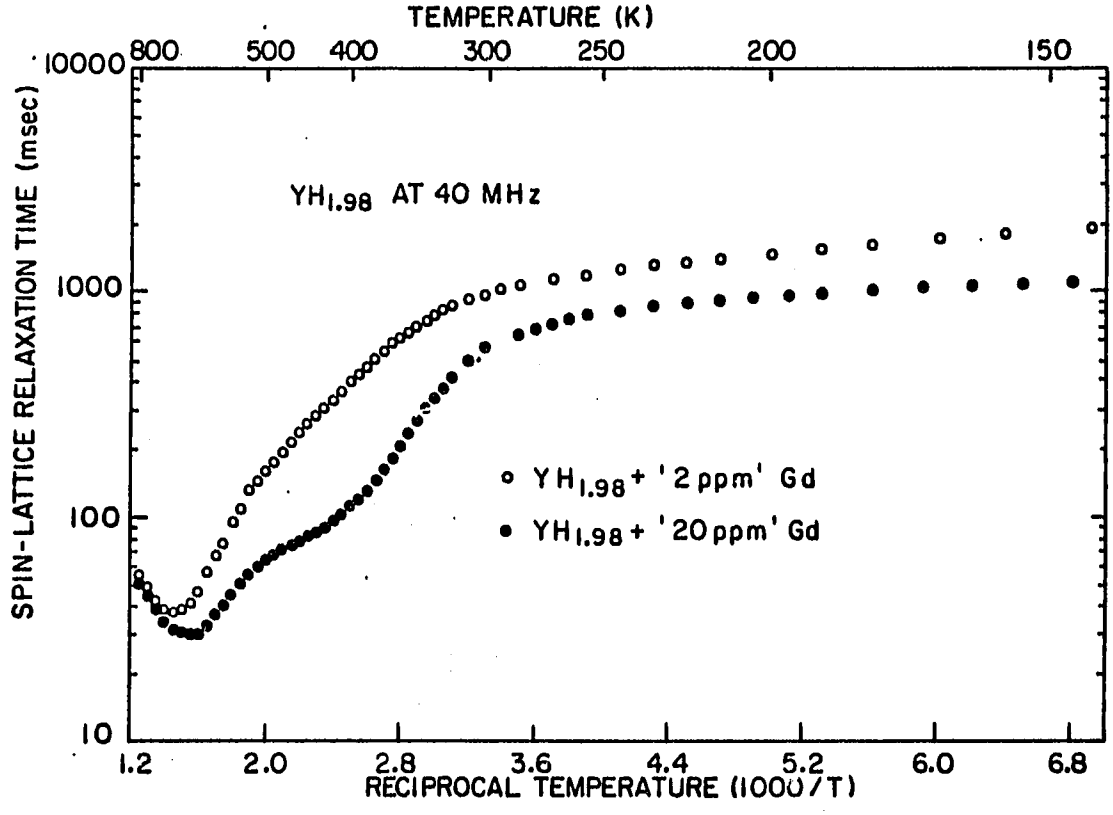

Figure 5-9. Comparison of log T_1 vs $10^3/T$ plots for $YH_{1.98}$ samples with 2 ppm Gd and 20 ppm Gd. The vanishing of the subsidiary minimum and the increase of T_1 at low temperatures are clearly seen for the purer sample

seen in some other metal hydrides, and it had been explained as arising from separate relaxation mechanisms for hydrogen occupying tetrahedral and octahedral interstitial sites. Such claims have to be investigated further; however, one can conclude without doubt that the subsidiary minimum seen in the "old" YH_x samples is caused by the presence of 20 ppm of gadolinium. Furthermore, the "slope-change" feature in the "new" sample can surely be ascribed to the remaining 2 ppm of gadolinium plus other minor paramagnetic impurities (2 ppm Ce^{3+}, 4 ppm Tb^{3+}, 4 ppm Pr^{3+}). Therefore, it appears likely that only a single diffusion-induced minimum without slope-change or other anomalies on the low temperature side will be observed if an entirely "impurity-free" hydride can be obtained. Since it is clear from the other evidence that there is substantial O-site occupancy, such a single minimum may imply that the times associated with jumps between various sites are not very different from one another (as opposed to the earlier assumption that $\tau_{D,O} < \tau_{D,T}$) so that separate minima can not be resolved.

Figure 5-10 shows the results of fitting the single-BPP function model to the "new" and "old" sample data, respectively, where the parameters were chosen for best fit around the principal minimum and at low temperature. The substantial weakening of the subsidiary minimum is clearly evident. The double-BPP function was also fitted to the data and these results are compared in Figure 5-11. The fit obtained in this case was, of course, much better than with the single-BPP function in the motional-narrowing region. However, the fits

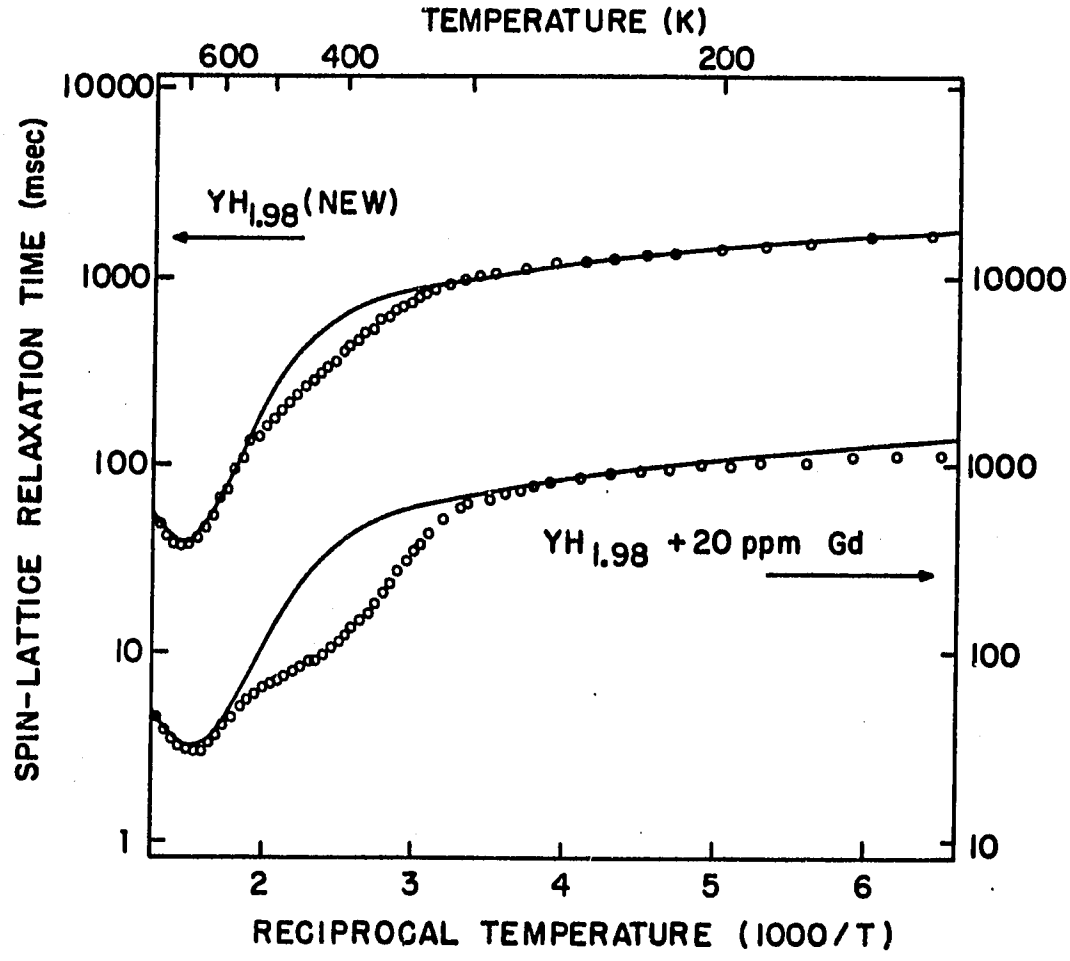

Figure 5-10. Comparison of T_1 data for "old" and "new" $YH_{1.98}$ samples. The solid lines are the least-squares fit using a single-BPP function. The parameters are chosen for best fit around the principal minimum and at low temperature

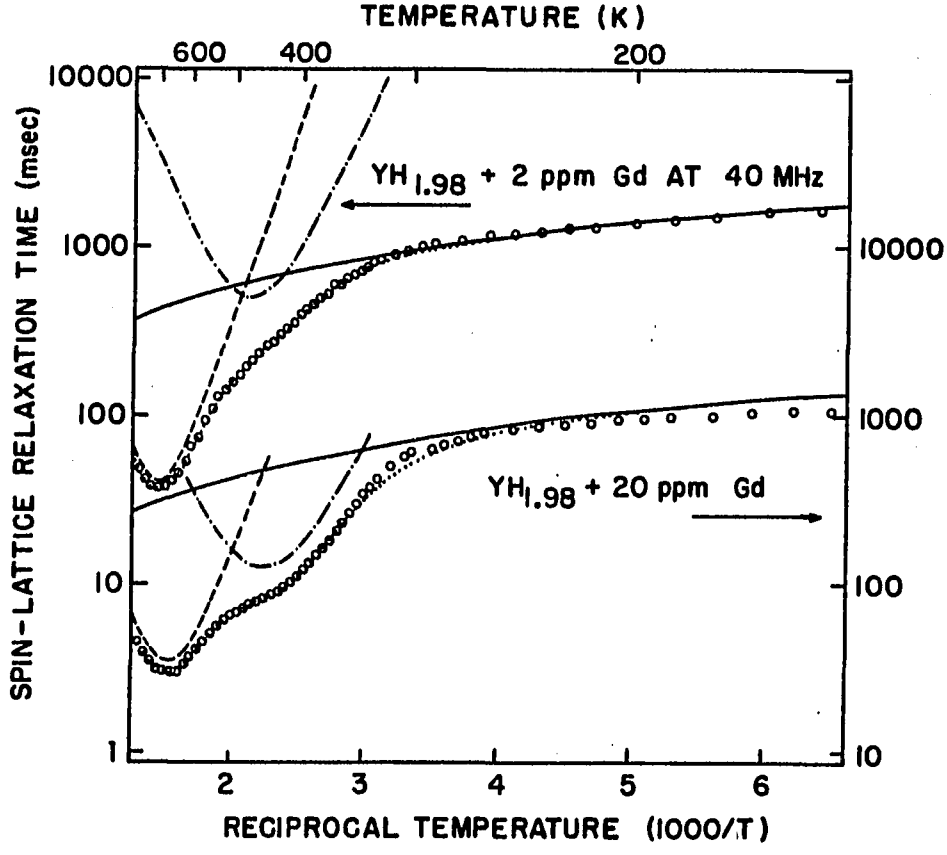

Figure 5-11. Comparison of T_1 data for two different $YH_{1.98}$ samples (old and new). The double-BPP function was used to resolve the subsidiary minimum from the principal minimum with the usual assumptions ($\tau_{D,O} << \tau_{D,T}$ and the relaxation due to O-O dipolar interaction is negligible)

obtained using both the double-BPP and single-BPP functions for the "old" sample were not as good as those for the "new" sample in the low temperature range (rigid-lattice regime). This result may surely be ascribed to the 20 ppm of gadolinium impurity present in the "old" sample. All these indications show the marvelous effectiveness of the low level of gadolinium impurity concentration in inducing proton spin-lattice relaxation. It should be noted that the temperature of the minimum spin-lattice relaxation time, $T_{1,min}$, is shifted from T = 654K to T = 688K for the "new" sample. This shift may be due to a discrepancy in the hydrogen concentration; the two hydride samples may not have exactly the same hydrogen concentration. As indicated in Chapter III, sample preparation section, the typical uncertainty in the determination of hydrogen concentrations is $\pm 2\%$.

On the basis of these remarkable observations, it seemed appropriate to set foot in the direction of studying the effects on the proton T_1 of controlled amounts of gadolinium impurity in both yttrium and lanthanum dihydrides. Such study would hopefully enable one to understand the mechanism by which the gadolinium ions relax the proton spins and affect so strongly their spin-lattice relaxation time at both low and high temperatures in typical metal hydrides.

D. Studies of $Y_{1-x}Gd_xH_{1.98}$

1. The impurity-induced relaxation rate

A series of $YH_{1.98}$ samples (i.e., 1.98 ± 0.02) containing controlled Gd^{3+} concentrations ranging from 50 ppm to 915 ppm was prepared, using

yttrium metal Y-12381B as basis. The measured proton spin-lattice relaxation times at 40MHz for these samples are shown plotted against reciprocal temperature in Figure 5-12.

Depression of the proton T_1 by the Gd^{3+} impurity ions is observed over the whole temperature range, from 77K to 800K. The depth of the subsidiary (or secondary) minimum increases as the Gd^{3+} concentration increases. The two minima then merge into a single broad minimum as the concentration of Gd^{3+} becomes greater than about 200 ppm. For the X = 915 ppm sample, the secondary minimum has even become the principal feature of the curve.

By using the two-sublattice BPP model for the curves for which two minima are resolvable, one finds that the strength (or the depth) of the subsidiary minimum decreases as the Gd^{3+} concentration decreases. A plot of the strength of the subsidiary minimum (which we have hitherto called $(T_{10,min})^{-1}$) versus Gd^{3+} concentration is shown in Figure 5-13. This graph strongly supports the view expressed earlier that the subsidiary minimum will disappear for completely impurity-free samples.

Hereafter, we shall regard the "new" $YH_{1.98}$ sample as "pure" yttrium dihydride. Even though it still shows the presence of some residual effects from the 2 ppm Gd^{3+} and 4 ppm Tb^{3+} impurity level, it is the purest yttrium hydride available in this study. The relaxation rate due to the interaction of the protons with the Gd^{3+} ions, $(T_{1p})^{-1}$, can be determined by subtracting the rate for the pure sample from the rates for the doped samples,

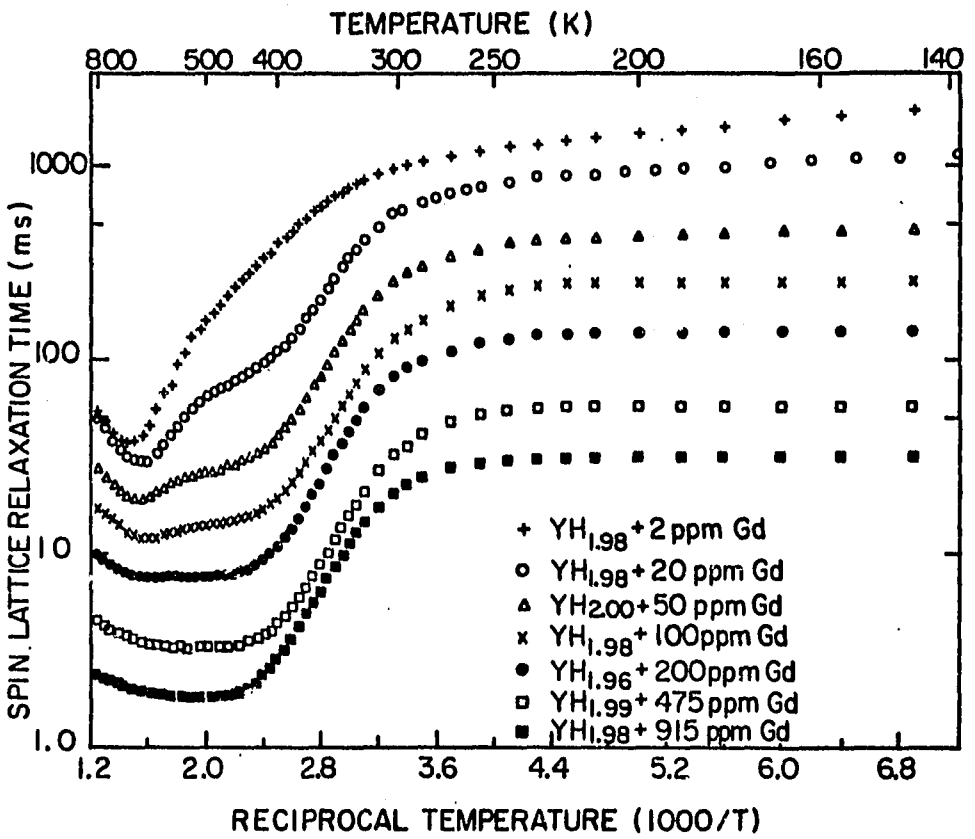

Figure 5-12. Composite plot of log T_1 versus $10^3/T$ for yttrium dihydrides with various Gd^{3+} concentrations at 40MHz. The Gd content in the two samples with least impurity were obtained by mass spectrometric analysis, while all other samples are prepared by the method described in Chapter III

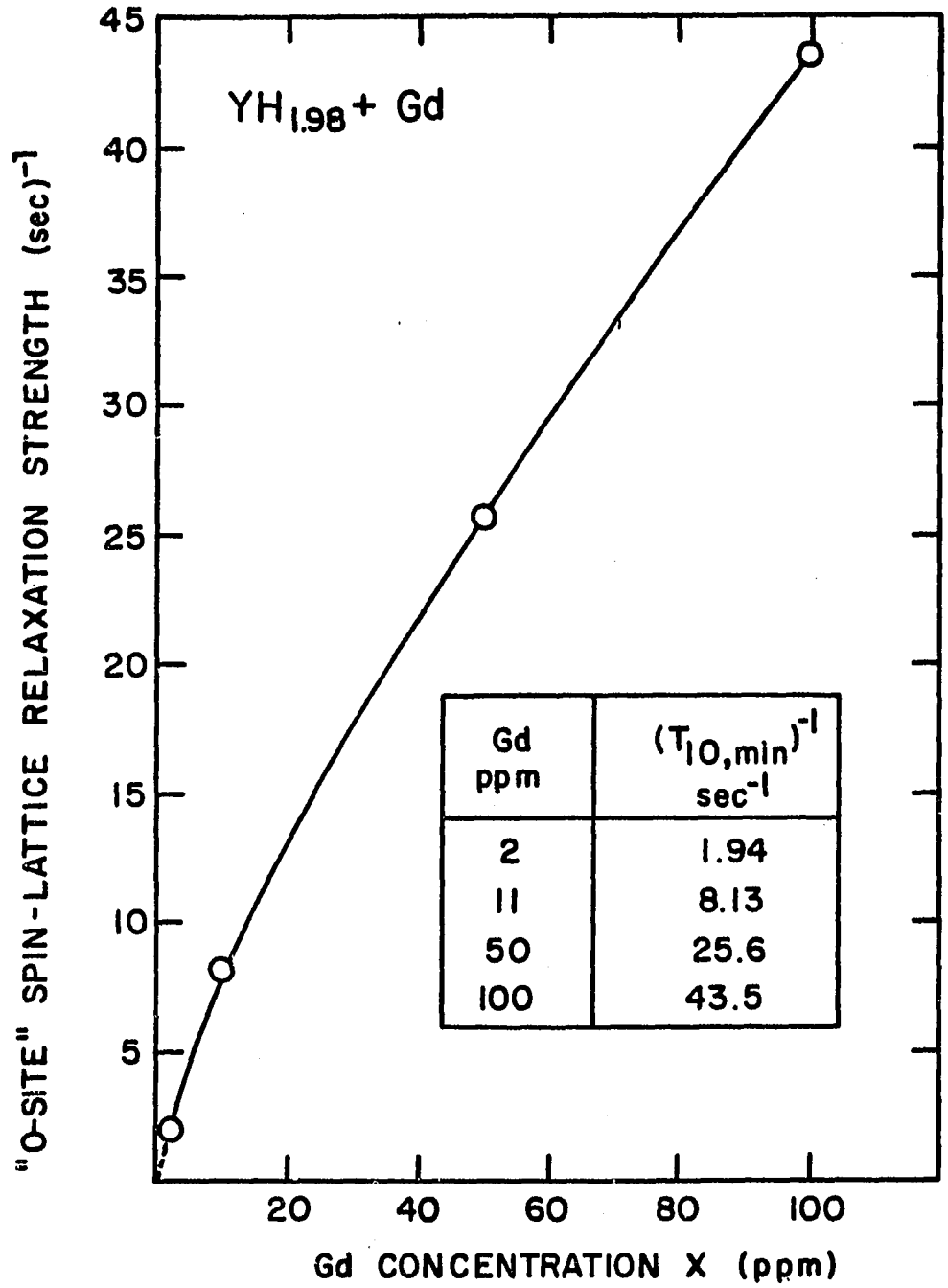

Figure 5-13. The variation with Gd concentration of the strength (or depth) of the subsidiary minimum, $(T_{10,min})^{-1}$ in yttrium dihydride at 40MHz. The point for the sample for which mass-spectrometric analysis indicated 20 ppm Gd^{3+} falls on the line at a Gd^{3+} concentration of 11 ppm. The solid line is a guide to the eye of the reader

$$(T_{1p})^{-1} = (T_1)^{-1}_{total} - (T_1)^{-1}_{pure}. \qquad (5\text{-}5)$$

The resulting rates, T_{1p}^{-1}, for these samples are plotted in Figure 5-14 for temperatures above 250K. For temperatures below 250K, the relaxation rate for each sample always shows weakly temperature dependent behavior. The rates increase rapidly for temperatures between 300K and 400K and then reach a broad maximum at higher temperatures. Qualitatively, this behavior resembles the "Magnetic Tagging" effect in Mn-doped PbF_2 reported recently by Vernon et al. (55). In the temperature range between 300K and 400K, the slopes of the log $(T_{1p})^{-1}$ versus $10^3/T$ curves are identical for all samples. We shall see that this means that the activation energy for hydrogen diffusion is the same in all the samples, i.e., it is independent of Gd^{3+} concentration.

Figure 5-15 shows a log-log plot of the relaxation rates due to the impurity, $(T_{1p})^{-1}$, at 500K and 145K as a function of Gd^{3+} concentration. Both at high temperatures (motional-narrowing) and low temperatures (rigid-lattice), the paramagnetic impurity contribution is directly proportional to the Gd^{3+} concentration. However, the impurity relaxation rate at 500K is about 20 times stronger than that at 145K. So actually, the impurity ions are more effective in relaxing proton spins at higher temperatures. In this figure, the $(T_{1p})^{-1}$ data points for the sample for which mass-spectrometric analysis indicated 20 ppm Gd^{3+} would fall on the lines at a Gd^{3+} concentration of 11 ppm. It is believed, therefore, that this graph can be used to determine low-level concentrations of paramagnetic impurities in yttrium hydrides with good accuracy.

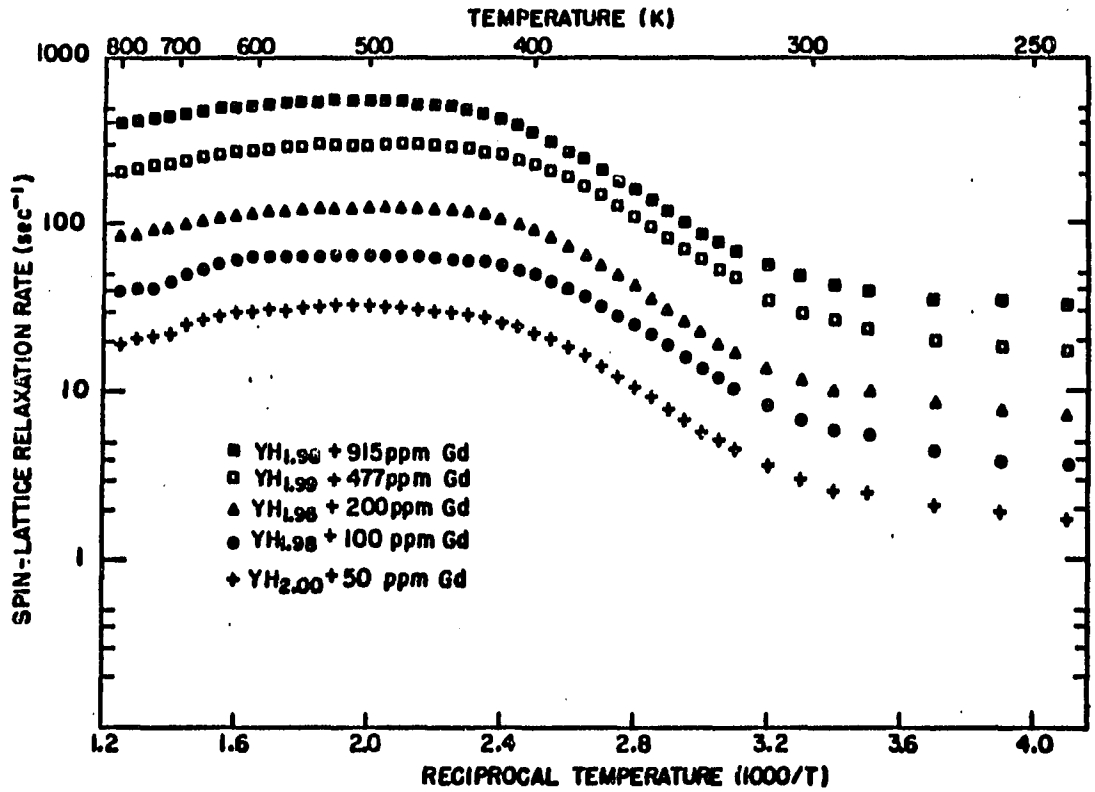

Figure 5-14. Logarithm of relaxation rate induced by Gd^{3+} impurity, T_{1p}^{-1}, versus reciprocal temperature $10^3/T$ for various Gd^{3+}-doped yttrium dihydride samples. T_{1p}^{-1} is obtained from $T_{1p}^{-1} = (T_1)^{-1}_{total} - (T_1)^{-1}_{pure}$

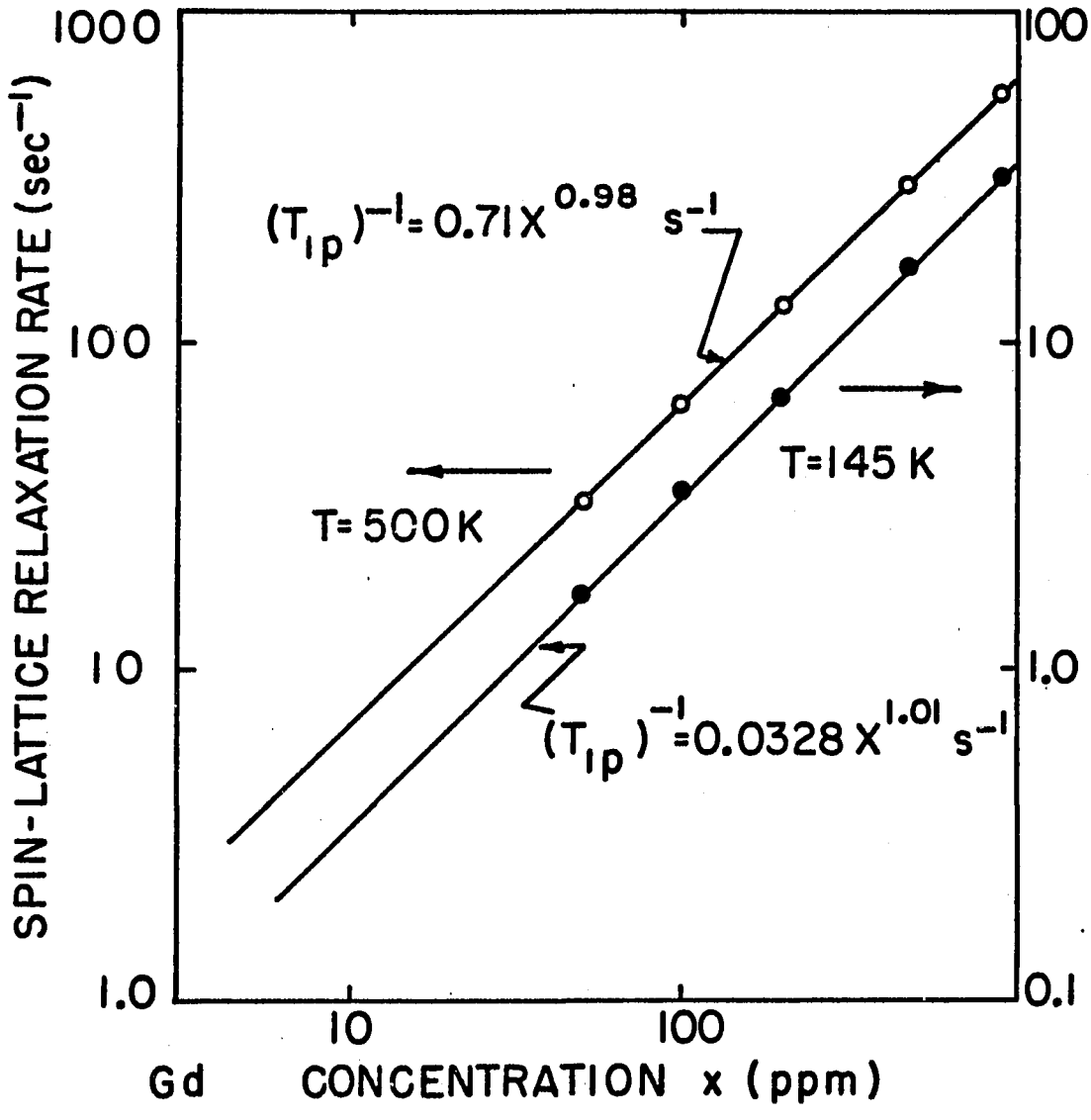

Figure 5-15. Logarithm of relaxation rate T_{1p}^{-1} against logarithm of Gd^{+3} concentration in $Y_{1-x}Gd_xH_{1.98}$, at T = 145K and T = 500K. The solid lines are the best fit by least squares. The $(T_{1p})^{-1}$ data points for the sample in which mass-spectrometric analysis indicated 20 ppm Gd^{3+} would fall on the lines at a Gd^{3+} concentration of 11 ppm

2. The spin diffusion region

The behavior of the $(T_{1p})^{-1}$ curve in the yttrium hydrides may be understood on the basis of the magnetic dipolar coupling of the proton spin to the impurity spin combined with both spin and particle diffusion (56) as described in Chapter II. The overall picture may be divided into three temperature regions. The first, low temperature region is the spin-diffusion region ($\tau_D < T_2$) in which T_{1p}^{-1} is only weakly temperature dependent. Since hydrogen ions are essentially immobile at these temperatures, the only way to transport extra spin energy from regions far from a paramagnetic center is via mutual spin flips (i.e., spin-diffusion). The observed relaxation rate is, therefore, jointly controlled by the direct relaxation rate near an impurity and by the spin-diffusion rate. The relaxation rate for this process given by Rorschach has been discussed in Chapter II (Equation 2-27), and is repeated here for convenience:

$$(T_{1p})^{-1} = 8\pi N D_s \beta \cdot \frac{\Gamma(\frac{3}{4})}{\Gamma(\frac{1}{4})} \cdot \frac{I_{3/4}(\delta)}{I_{-3/4}(\delta)}. \qquad (5\text{-}6)$$

In Equation (5-6), N is the impurity concentration. In the case of fcc yttrium hydride, $N = \frac{4X}{a_o^3}$, where a_o is the lattice constant and X the number of impurity ions per metal atom. D_s is the diffusivity for nuclear spin-diffusion, for which we use the estimate given by

Bloembergen (30), $D_s = \frac{a^2}{5CT_2}$, where $a = a_o/2$ and T_2 are the internuclear spacing the nuclear spin-spin relaxation time, respectively. The "pseudopotential radius", $\beta = (C/D_s)^{1/4}$, where C gives the strength of the proton-ion interaction:

$$C = \frac{2}{5} (\gamma_p \gamma_n \hbar)^2 \, J(J+1) \, \frac{\tau_i}{1+\omega_0^2 \tau_i^2}, \tag{5-7}$$

γ_p and γ_n are the gyromagnetic ratios of the impurity ions and the nuclei, respectively; J is the total angular momentum quantum number of the impurity ion. The spin-lattice relaxation time of the impurity ion is τ_i, and ω_0 is the Larmor precession frequency of the protons. The quantity δ is defined by $\delta = \frac{\beta^2}{2b^2}$, where b is the diffusion barrier radius within which spin-diffusion cannot occur,

$$b = \left[\frac{3\langle\mu_p\rangle}{\mu_n}\right]^{1/4} \left(\frac{a_o}{2}\right) \tag{5-8}$$

μ_p and μ_n are the magnetic moments of the ions and protons, respectively. The temperature dependence of $\langle\mu_p\rangle$ is given by Equations (2-30, 2-31, 2-32) of Chapter II.

Drulis (57) has measured the ESR linewidth for 3% Gd^{3+} in $YH_{1.83}$. The linewidth, $\Delta\omega$, increases linearly with temperature. If we assume that this represents lifetime broadening associated with the ion's

spin-lattice relaxation, then $\Delta\omega = \tau_i^{-1}$, and we find that τ_i conforms to a Korringa relation, $T\tau_i = 1.0 \times 10^{-7}$ sec-K. Using the values of

$$\tau_i = 1.0 \times 10^{-7} \times T^{-1} \text{ sec},$$

$$T_2 = 1.2 \times 10^{-5} \text{ sec},$$

$$a_0 = 5.204 \times 10^{-8} \text{ cm},$$

$$J = 7/2$$

$$\gamma_p = g_p \mu_0 / \hbar = 1.76 \times 10^7 \text{ Hz/Oe},$$

the relaxation rate T_{1p}^{-1} in the spin-diffusion region can be calculated as a function of temperature from Rorschach's Equation (5-6). The relaxation rates T_{1p}^{-1} obtained agree satisfactorily with the experimental values, as shown in Figure 5-16 for $T \lesssim 310$K (see below).

In the spin-diffusion region, even though T_{1p}^{-1} is observed to be only weakly temperature dependent, it does increase as the temperature decreases. Since from Equation (5-7), $C \alpha \tau_i/(1+\omega_0^2 \tau_i^2)$, it appears that T_{1p}^{-1} should continue to increase until a temperature at which $\omega_0 \tau_i \simeq 1$ is reached. Following this maximum, the rate will then decrease with decreasing temperature. Such behavior of T_{1p}^{-1} has been reported for ^{19}F in rare-earth doped CaF_2 samples (58-62). Thus, τ_i can be determined at the temperature at which the minimum in T_{1p} is observed. This could be of some importance because, with a knowledge of τ_i, T_{1p} and the concentration and identity of the paramagnetic species present,

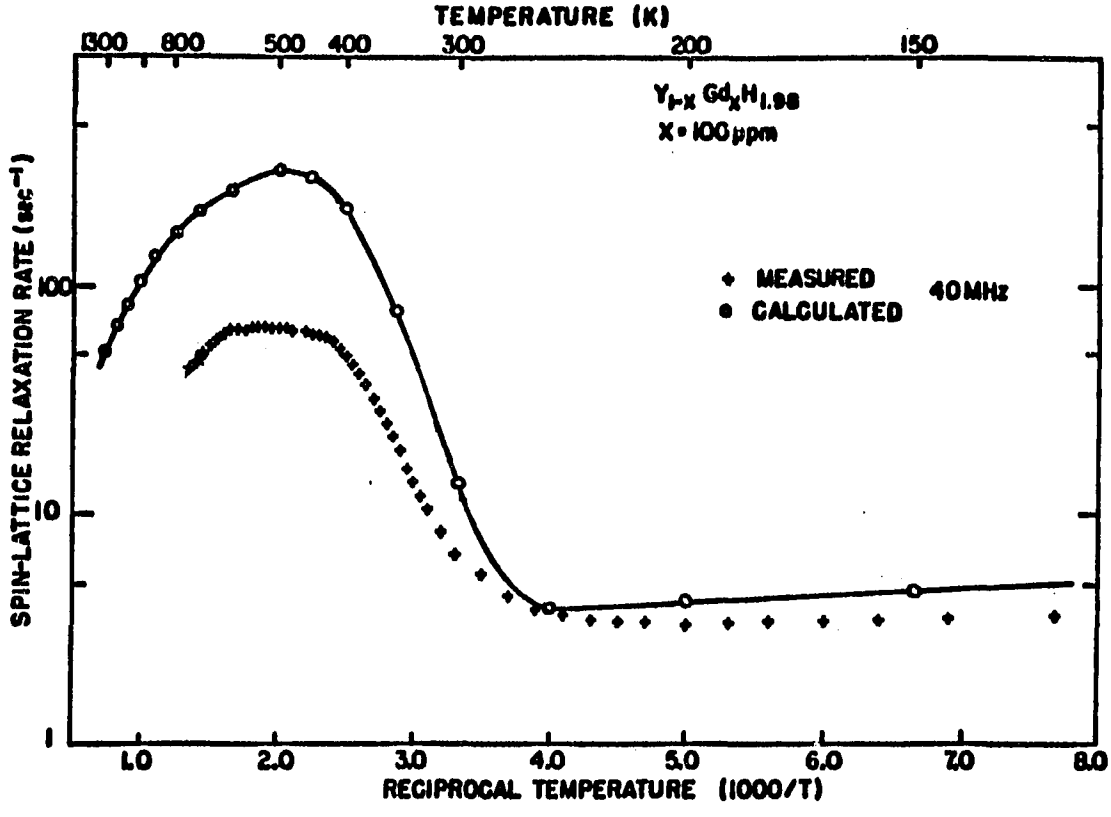

Figure 5-16. Comparison of experimental $T_{1\rho}^{-1}$ values for $YH_{1.98}$ = 100 ppm Gd with the rates calculated by the appropriate Rorschach equations in various temperature regions (spin diffusion, slow atomic diffusion, fast atomic diffusion). The solid line is a guide to the eye of the reader

one could deduce D_{s_2} (rather than rely on the rather approximate value used above, $D_s \overset{\sim}{=} \frac{a^2}{50T_2}$). It follows further that, since in the low temperature regime the only temperature dependence of T_{1p} arises from that of τ_i, one could then derive values of τ_i at other temperatures in this regime.

3. The atomic diffusion region

With increasing temperature, the motional-narrowing region is entered and hydrogen diffusion becomes effective in transporting nuclear magnetization. This is the atomic diffusion limited regime.

The change-over temperature from the low temperature (spin diffusion) regime to the atomic diffusion regime, is found to be about 310K in the case of Gd^{3+} in yttrium dihydride. For temperatures $T \overset{\sim}{>}$ 310K, atomic diffusion takes over from spin diffusion as the agent for transporting proton magnetization to the paramagnetic ion relaxation center. Hence, the diffusion barrier radius b is replaced by the proton-Gd^{3+} spacing, $a_1 = \frac{\sqrt{3}a_0}{4}$, and the spin-diffusivity D_s is replaced by the atomic-diffusivity,

$$D_A = D_0 \exp(-E_{act}/k_B T),$$

and $$D_A = \frac{a^2}{6\tau_D},$$

so $$D_A = \frac{a^2}{6\tau_{D,0}} \cdot \exp(-E_{act}/k_B T), \qquad (5\text{-}9)$$

where $a = a_o/2$ for jumps between T-sites (as an approximation jumps involving O-sites are ignored), and $\tau_{D,O} = 2\tau_{C,O}$. The modified form of Equation (5-6) then contains $D_A^{3/4}$ as a factor and, for temperatures somewhat larger than 310K, it is this factor which provides the main temperature dependence of T_{1p}^{-1}. (The temperature dependences arising from $C^{1/4}$ and the Bessel function ratio are smaller.) The apparent activation energy in this regime is therefore predicted to be about 3/4 that for hydrogen diffusion. The bottleneck in this region is the relaxation transfer rate to nuclei far from the impurity ion by atomic diffusion (or particle diffusion).

With further increasing temperature, hydrogen diffusion becomes very fast. Here the correlation time for the fluctuation of the interaction with an impurity ion, occurring in Equation (5-7), becomes $(\tau_i^{-1} + \tau_D^{-1})^{-1}$ instead of simply τ_i in the spin-diffusion region. When the pseudopotential radius, $\beta = (C/D_A)^{1/4}$, becomes less than the gadolinium-nearest neighbor proton distance, $a_1 = \frac{\sqrt{3}a_o}{4}$, the relaxation process is no longer limited by atomic diffusion. This is the fast atomic-diffusion regime in which the bottleneck becomes the direct relaxation rate of protons adjacent to the paramagnetic impurity ions. Using the appropriate definitions of β and D_A, the change-over from slow atomic diffusion to fast atomic diffusion can be said to occur when $\tau_D^{-1} = Ca_1^{-6}$. The observed transition temperature in this case is approximately 400K and should be independent of the proton resonance frequency.

Figure 5-16 compares the results of this calculation of T_{1p}^{-1} with the experimental values for the sample with 100 ppm Gd^{3+}. Without any adjustable parameters this calculation reproduces the essential features of the $T_{1p}^{-1}(T)$ temperature dependence. As remarked above, in the atomic diffusion limited region, $T_{1p}^{-1}(T)$ is dominated by the $D_A^{3/4}$ factor and should display an apparent activation energy three-fourths that of the hydrogen diffusion. The experimental data for T_{1p}^{-1} in Figure 5-16 yield an apparent E_{act} = 0.29 eV/atom in the temperature range 320K to 400K which may be compared with 0.43 eV/atom for τ_D. However, there is a substantial discrepancy between the calculated and experimental values in the high temperature portion of the curve (regions two and three). The experimental rates obtained are weaker than those calculated using Equation (5-6) by a factor of about 5.

Possible sources for this discrepancy include the values of the ion spin-lattice relaxation time τ_i and the hydrogen jump time τ_D. The values of τ_i used in the calculation may not be correct, since the concentration of Gd^{3+} is much more dilute and the hydrogen concentration is higher in this study than in Drulis' sample of $YH_{1.83}$. Furthermore, the temperature dependence of τ_i may not follow Korringa behavior above 300K. In addition, the Gd^{3+} impurity may not be completely randomly distributed (although the observed linear dependence of T_{1p}^{-1} on Gd^{3+} concentration implies that the Gd^{3+} distribution is random). Also, the dwell time τ_D for hydrogen close to the Gd^{3+} ions may differ from that appropriate to hydrogen far away from the ion (although the

near equality of atomic sizes and of hydrogen affinities of Y and Gd metals suggests such difference should be small). All these factors may combine in influencing the outcome of the calculation.

4. Determination of Korringa constants

Several articles (38,52) have suggested and used a method for determining the Korringa constant by plotting the total relaxation rate T_1^{-1} in the rigid-lattice regime versus temperature. In this regime, $T_1^{-1} = T_{1e}^{-1} + T_{1p}^{-1}$, so that if T_{1p} is temperature independent, such a graph should yield a straight line whose slope gives the Korringa constant and whose intercept on the T_1^{-1} axis gives the impurity rate, T_{1p}^{-1}. This method of analysis was carried out for the purest yttrium hydride, $YH_{1.98}$, and for the samples with 20 ppm and 50 ppm Gd^{3+} concentrations. The resulting graphs are shown in Figure 5-17.

The straight lines in this figure have been fitted to the "straight line" portion of the data. It is evident in the case of the 50 ppm Gd^{3+} sample that at low temperatures T_1^{-1} passes through a minimum so that this straight line region is somewhat arbitrary. From the slopes of the lines one finds that the purest sample has the smallest value for the Korringa constant, and the 50 ppm Gd^{3+} sample has the largest. The results obtained in this way and the results obtained directly from the T_1T product (as discussed in Section C) are in reversed order. That is, in the latter case the purest sample has the largest Korringa constant. It is, therefore, clear that this method (of Figure 5-17) is

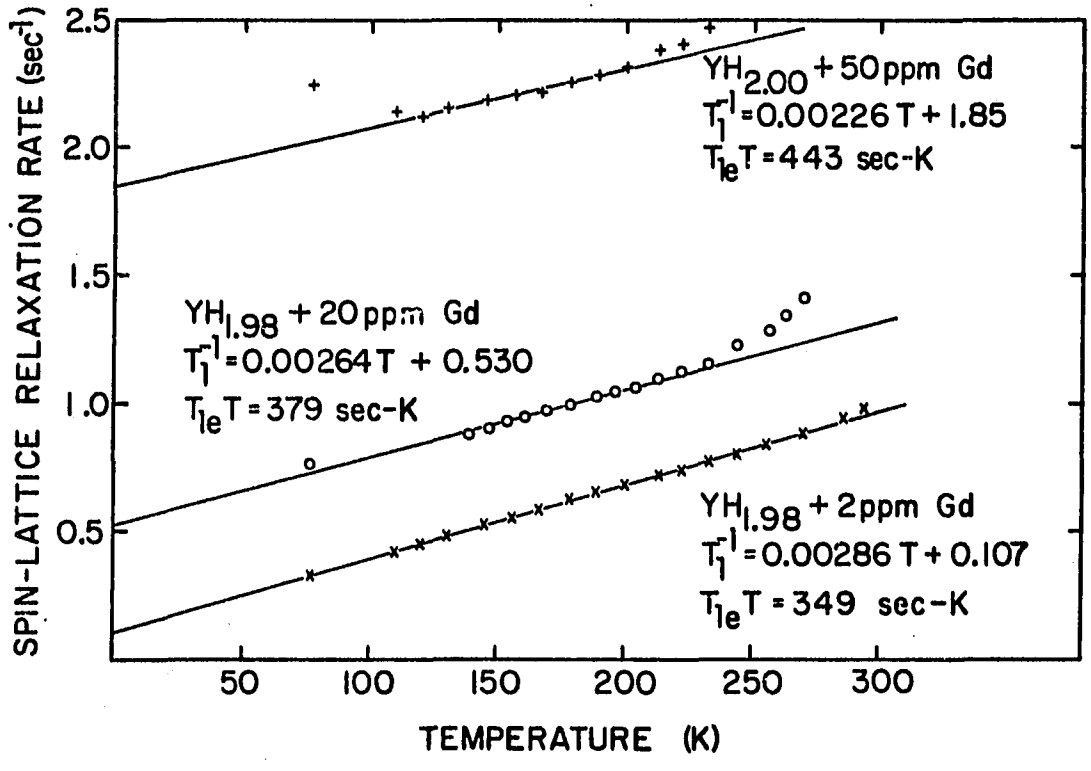

Figure 5-17. The temperature variation of the proton spin-lattice relaxation rate T_1^{-1} in yttrium dihydride at low temperatures for three samples with lowest Gd concentrations (2 ppm, 20 ppm, and 50 ppm). The solid lines have been fit to the "straight line" portion of the data

not an appropriate one by which to determine the Korringa constant. The failure of the method is caused by the fact that the relaxation rate T_{1p}^{-1} due to interaction between the paramagnetic impurity ion and the proton spin is not constant at low temperatures.

5. Rigid lattice temperature dependence of T_{1p}

An estimate of the relation between T_{1p} (obtained using Equation 5-5) and temperature can be obtained by plotting log T_{1p} vs log T. This requires first of all that T_{1p} can be determined by suitable subtraction of the relaxation rate in a pure sample and assumes that $T_{1p} \propto T^n$, that is, that there exists a power law dependence on T. Figure 5-18 shows such a plot of the T_{1p} data for the $YH_{1.98}$: Gd^{3+} samples. The low temperature portions of these plots show reasonable straight-line behavior corresponding to an average dependence on temperature of the form $T_{1p} \propto T^{0.16}$. This may be compared with the relation $T_{1p} \propto T^{0.25}$ which is to be expected if the ion spin-lattice relaxation time τ_i itself obeys a Korringa product relation, $\tau_i T$ = constant, and which was assumed to hold in making the calculation of T_{1p}^{-1} described earlier. The difference between the two power laws is, in fact, already evident in Figure 5-16 where the calculated curve has the greater slope in the low temperature region.

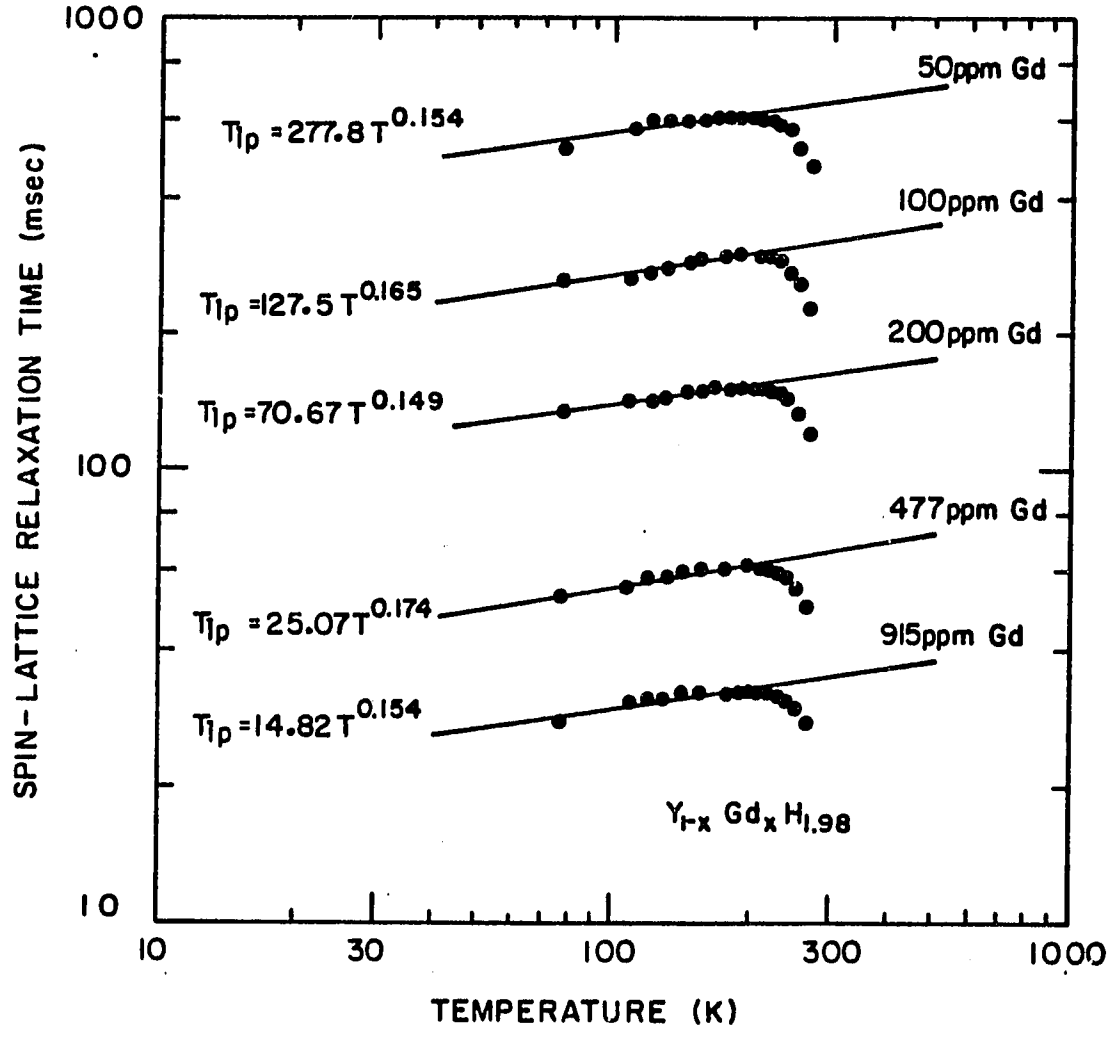

Figure 5-18. Logarithm of $T_{1\rho}$ against logarithm of T; the temperature dependences of $T_{1\rho}$ for $Y_{1-x}Gd_xH_{1.98}$ samples are thus obtained in the spin diffusion region. The solid lines are the least squares fit to the "straight line" portion of the data

E. Studies of $La_{1-x}Gd_xH_{2.25}$

In order to determine that the effects of the Gd^{3+} impurity described in the previous section were not unique to the yttrium hydrides, a series of $LaH_{2.25}$ samples doped with controlled levels of Gd^{3+} impurity was also prepared and studied. These samples were doped with 50 ppm, 100 ppm, 200 ppm and 500 ppm of Gd^{3+}, respectively. The composition x = 2.25 was chosen in order that the region of the T_1 minimum could be adequately measured at 40MHz. As seen in Figure 5-1, the temperature of the T_1 minimum is roughly 500K, so that excellent delineation of the entire minimum is attainable.

Qualitatively, the presence of Gd^{3+} ions has the same effects on the proton spin-lattice relaxation time as in the yttrium hydrides. A depression of the relaxation time over the entire temperature range investigated is again observed. A composite plot of the T_1 results in this series of samples is shown in Figure 5-19. Features similar to those in YH_x again appear: the growth in strength of the subsidiary minimum with Gd^{3+} concentration, the merging of the two minima at the highest Gd^{3+} concentration, and weakly temperature dependent relaxation times at low temperatures. A single BPP function was used to fit the relaxation time for the "pure" $LaH_{2.27}$ prepared from batch La-8681 of lanthanum metal. The result of this fit is shown in Figure 5-20, and is seen to be extremely satisfactory, showing the expected correct behavior for an "impurity-free" hydride. The fitting parameters obtained are

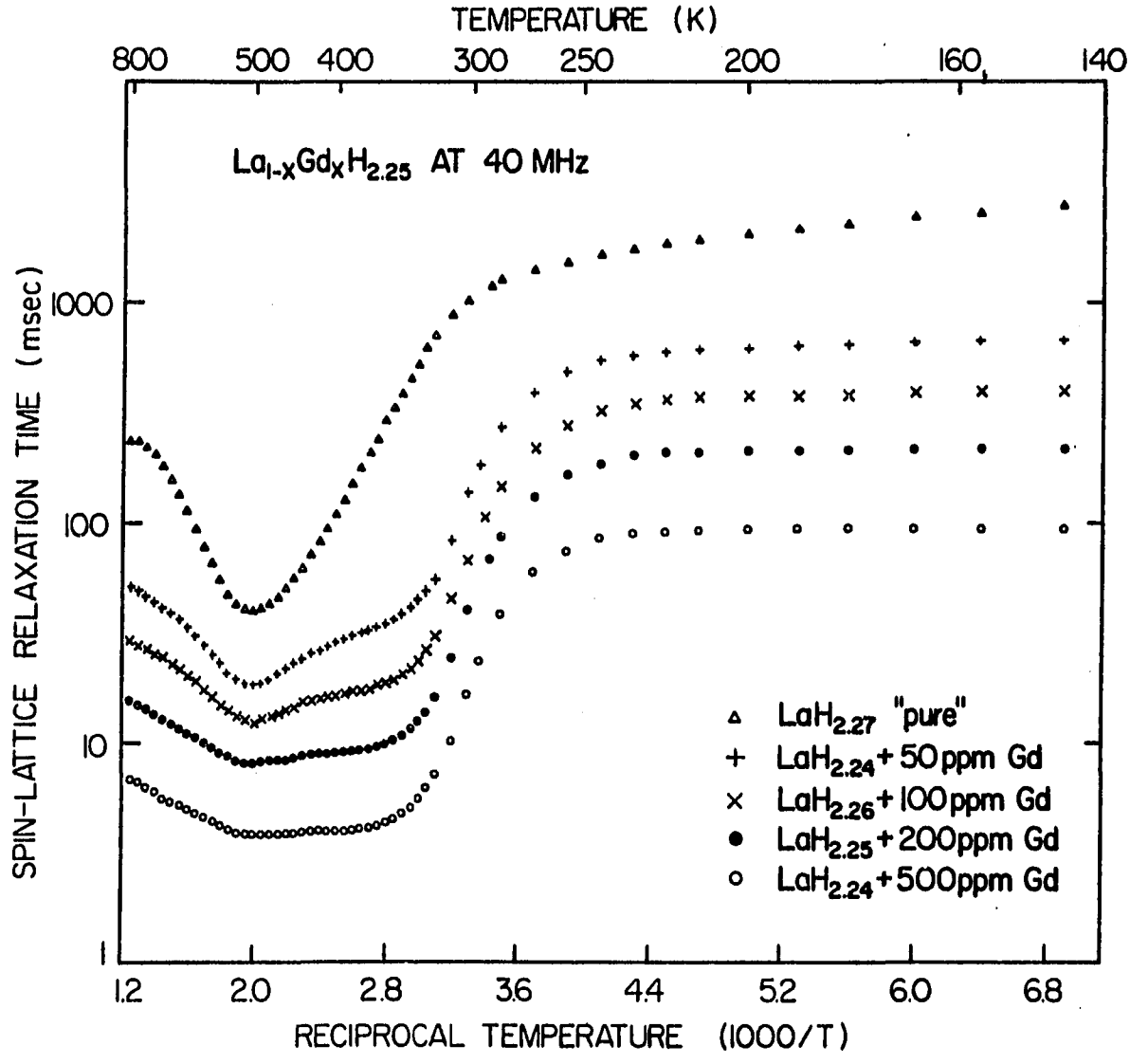

Figure 5-19. The temperature variation of the proton spin-lattice relaxation time in lanthanum hydride, $LaH_{2.25}$, for several concentrations of added gadolinium

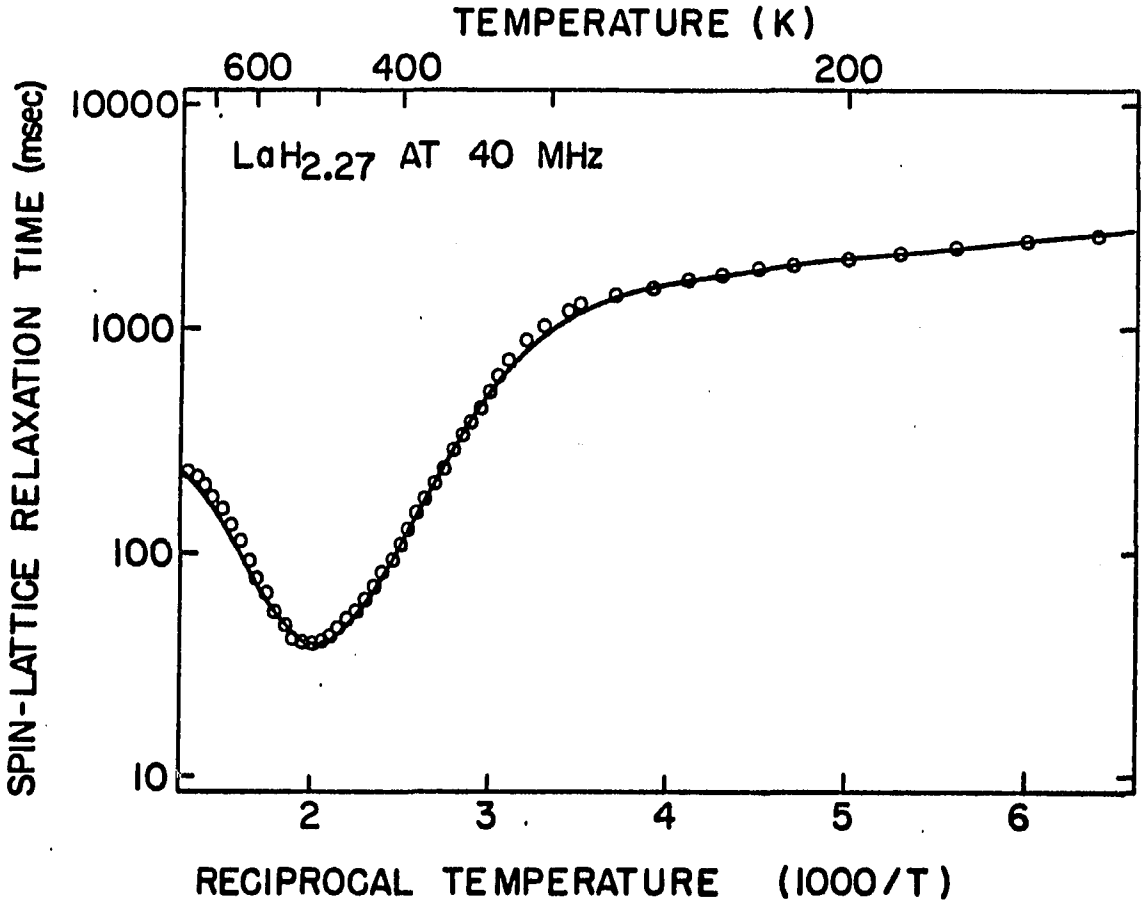

Figure 5-20. Logarithm of T_1 versus reciprocal temperature $10^3/T$ for the "pure" $LaH_{2.27}$ sample at 40 MHz. The solid line is the best fit using a single BPP function. The fitting parameters are E_{act} = 0.35 eV/atom, $\tau_{D,0}$ = 1.4 x 10^{-12} sec, $T_{1,min}$ = 42.1 msec and K = 410 sec-K

E_{act} = 0.35 eV/atom,

$\tau_{D,0}$ = 1.4 x 10^{-12} sec^{-1},

$T_{1,min}$ = 42.1 msec,

K = 410 sec-K.

The procedure used to analyze the yttrium hydride data was again applied, i.e., the measured rate, T_1^{-1}, for pure $LaH_{2.27}$ was subtracted from the others. The resulting relaxation rates due to the coupling between the nuclei and the Gd^{3+} ions are plotted in Figure 5-21. The three characteristic regions are again clearly seen, namely, spin-diffusion at low temperatures, atomic diffusion limited at intermediate temperatures, and rapid atomic diffusion at higher temperatures. An important difference with respect to the YH_x case appears in that the "activation energy" in the slow atomic diffusion region is no longer 3/4 of the activation energy for hydrogen diffusion. In fact, the two energies are almost identical. The reason for this is unknown. However, we may suppose that it is somehow related to the greater O-site occupancy in $LaH_{2.25}$ compared to $YH_{1.98}$. It is worth noting that in the case of PbF_2 : Mn the slope of the $(T_{1\rho})^{-1}$ versus T^{-1} curve in the intermediate region corresponds, in fact, to the activation energy for F^- ion motion (55). But in that case, the relaxation is through a contact interaction rather than the dipolar interaction. Just as for the yttrium hydrides, the "activation energy" in this intermediate temperature region is independent of Gd^{3+} concentration.

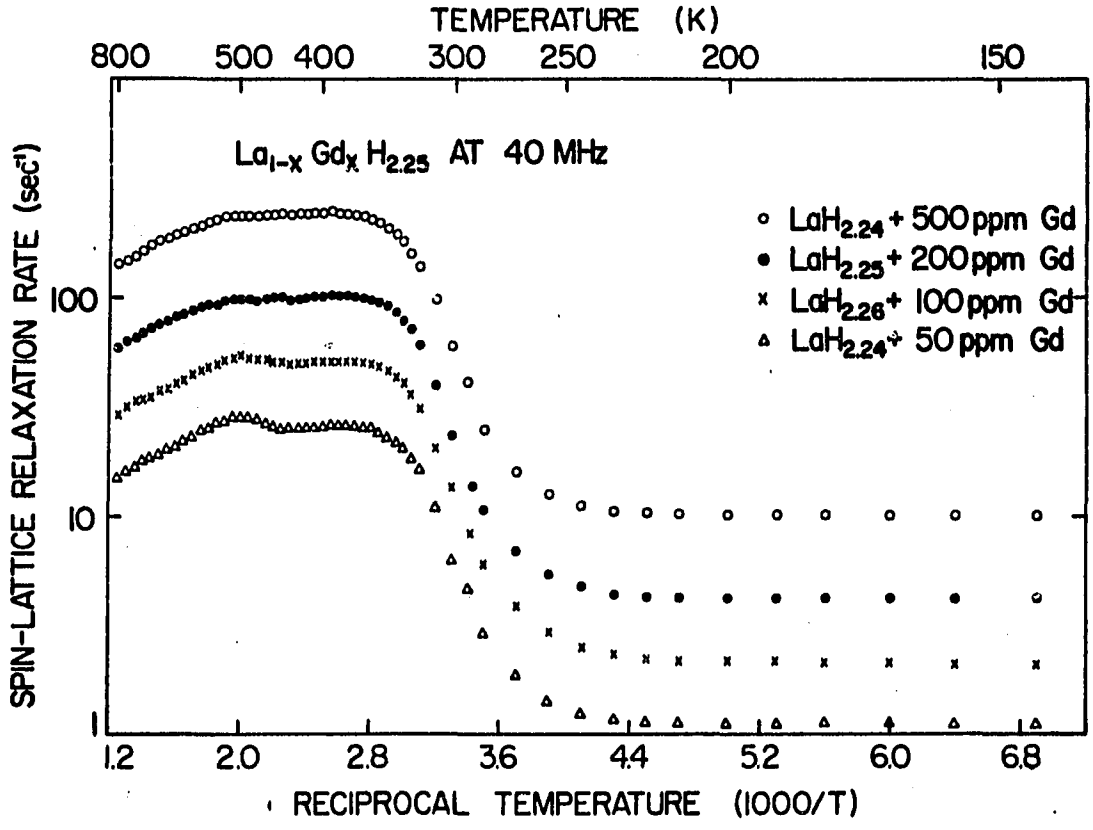

Figure 5-21. Logarithm of relaxation rate induced by Gd^{3+} impurity, T_{1p}^{-1} versus reciprocal temperature $10^3/T$ for various Gd^{3+}-doped lanthanum hydrides

A linear relation between the impurity ion induced relaxation rate, T_{1p}^{-1}, and the impurity concentration X is once again obtained within experimental error, as shown in Figure 5-22. The rate T_{1p}^{-1} is proportional to the Gd^{3+} concentration both at high (T = 500K) and low (T = 145K) temperatures, the rate at high temperatures being about 30 times more effective than that at the low temperatures. An attempt to determine the temperature dependence of T_{1p} at low temperatures by plotting log T_{1p} versus log T is shown in Figure 5-23. Again, T_{1p} is seen to be weakly temperature dependent, $T_{1p} \propto T^{0.16}$. This is similar to the case of Gd^{3+} in yttrium hydrides (Figure 5-18); however, the proportionality constant is slightly larger than that in the yttrium hydrides. It is also evident in Figure 5-23 that the straight-line fits are not nearly so good as in Figure 5-18. Qualitatively, the data points do not appear to follow straight-line behavior. Further measurements in the low-temperature region are clearly needed.

A quantitative fit to the data parallel in Figure 5-16 was not attempted both because no T_1 data are available for these hydrides and also because of the additional complexity caused by nonnegligible O-site occupation. However, the general similarity with the data for the yttrium hydrides is convincing evidence that Gd^{3+} ions cause strong proton relaxation in both systems largely through a dipolar interaction.

F. Studies of $La_{1-x}Ce_xH_{2.25}$

In their pioneering NMR study of lanthanum hydrides, Schreiber and Cotts (47) used commercially supplied La metal having typical impurity

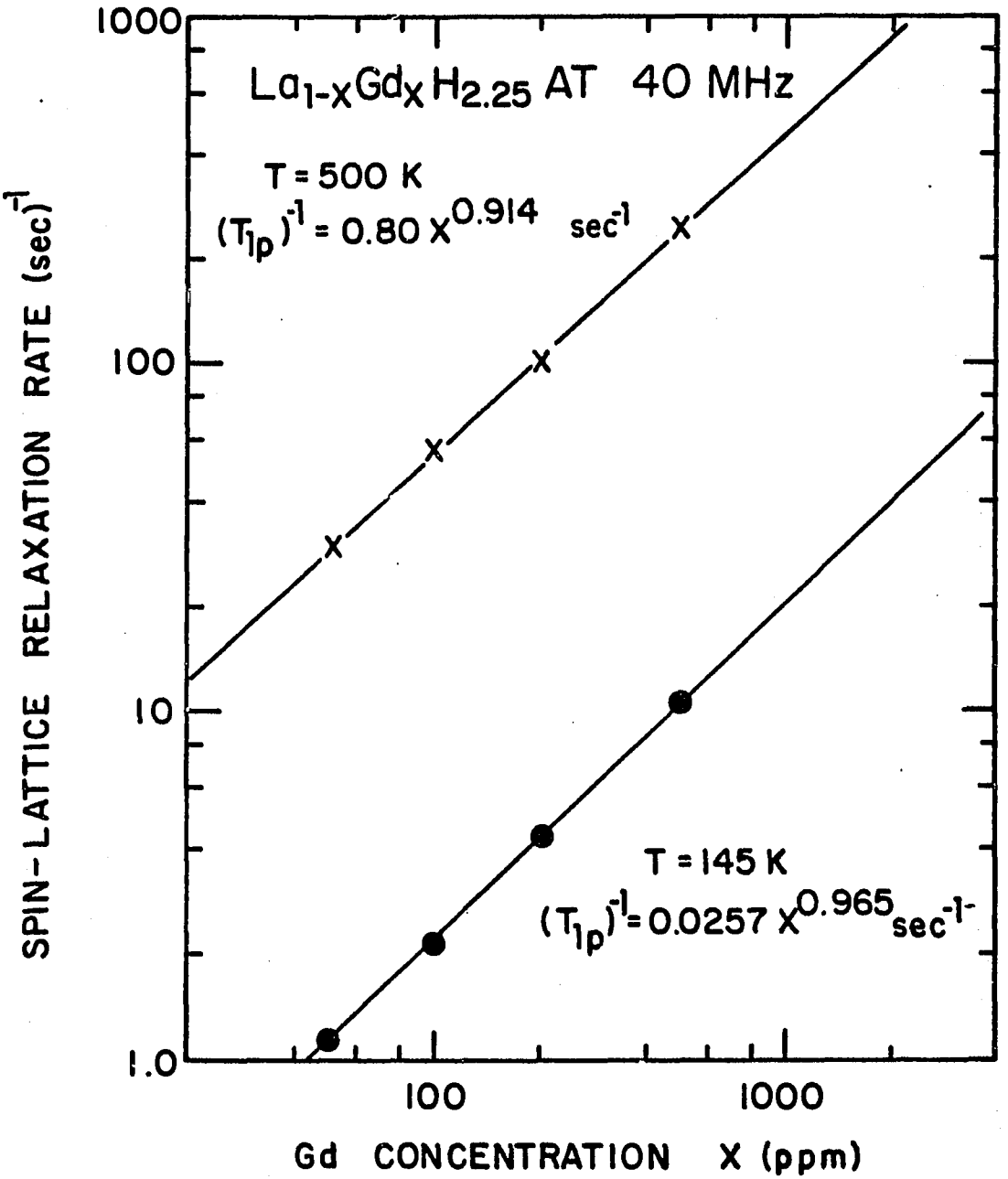

Figure 5-22. Logarithm of Gd^{3+} ion induced relaxation rate, log T_{1p}^{-1}, versus logarithm of Gd^{3+} concentration in $La_{1-x}Gd_xH_{2.25}$ samples, both at T = 145K and T = 500K. The solid lines are the best fit to the data points

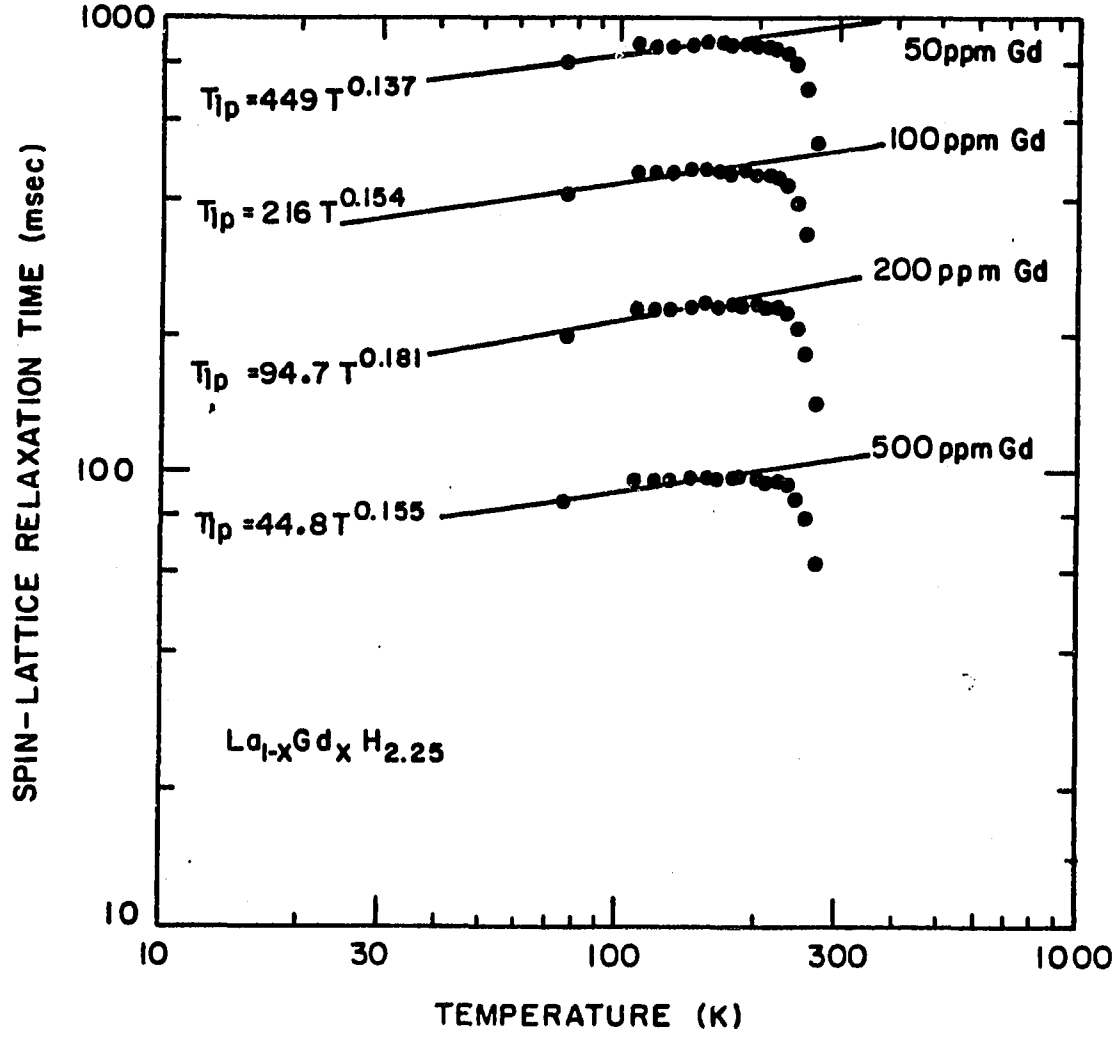

Figure 5-23. Logarithm of Gd^{3+} ion induced relaxation time log $T_{1\rho}$ versus log T for $La_{1-x}Gd_xH_{2.25}$ samples with X = 50, 100, 200, and 500 ppm in the spin diffusion region at 40 MHz. The solid lines have been fit to the "straight line" portions of the data in the lowest temperatures region

levels (stated by the supplier) of several thousand ppm of mainly light rare earths (Ce, Pr, Nd). Although the proton T_1 was strongly depressed at low temperatures, no significant depression occurred in the high temperature region so that the T_1 minimum due to the modulation of the proton-proton dipolar interaction by hydrogen diffusion appeared normal. A very similar observation was made in a more recent study in this laboratory (63) in which La containing 2700 ppm of Ce^{3+} was used to prepare $LaH_{2.89}$. This suggests that cerium behaves quite differently from gadolinium, particularly in the region of atomic diffusion where the "magnetic tagging" effect apparently does not occur. An obvious probable explanation for this relates to impurity ion relaxation through the phonons (additional to the Korringa process already considered) and lies in the fact that Gd^{3+}, being an S-state ion ($J = S = 7/2$) interacts only weakly with the crystalline electric field (CEF) so that it is a relatively slowly relaxing ion. On the other hand, Ce^{3+} ($S = 1/2$, $J = 5/2$) interacts strongly with the CEF and is a relatively fast relaxing ion with a more strongly temperature dependent relaxation time. (In some situations Ce can exist as Ce^{4+} or even in a mixed-valence state, where Ce^{4+} is nonmagnetic. For the present we make the simplest assumption that all Ce is in the form Ce^{3+}.)

It's interesting to note at this point that whereas the light rare earths are likely to be present in lanthanum, gadolinium is not, and that essentially the reverse is true for yttrium. This very likely accounts for the fact that the full range of double-minimum and slope-

change effects have been reported in studies of YH_x (12), but not in those of LaH_x.

Accordingly, to investigate these possibilities more systematically, it was decided to make measurements on $LaH_{2.25}$ and $YH_{1.98}$ doped with controlled levels of cerium impurity (i.e., 100, 200, 480, and 910 ppm).

The measured proton spin-lattice relaxation times for the $La_{1-x}Ce_xH_{2.25}$ samples are plotted in Figure 5-24. Unfortunately, these hydrides were prepared from Ames Laboratory La-72280 metal which was found to contain about 15 ppm of Gd and 80 ppm of Fe impurities (by spark source mass spectrometric analysis).

The Ce^{3+} ions are very effective in the low temperature region. Although the depression of T_1 is not as great as with Gd^{3+} (compare Figure 5-19), the effect is more strongly temperature dependent. At the higher Ce^{3+} concentrations, T_1 clearly passes through a broad maximum and then decreases with decreasing temperature. All the Ce^{3+}-doped samples show the presence of a subsidiary minimum, but it is independent of Ce^{3+} concentration. The data show that Ce^{3+} is ineffective in the high temperature region. This is also very different from the case of Gd^{3+} in $LaH_{2.25}$ (Figure 5-19). However, by comparing the samples with Ce^{3+} dopant with the "pure" sample, a small depression of the T_1 values at high temperatures still occurs. Thus, it is tempting to blame the small depression and the subsidiary minimum on the presence of the 15 ppm Gd^{3+}, since the high temperature T_1 values are virtually independent of Ce^{3+} concentration. Yet the "pure" sample

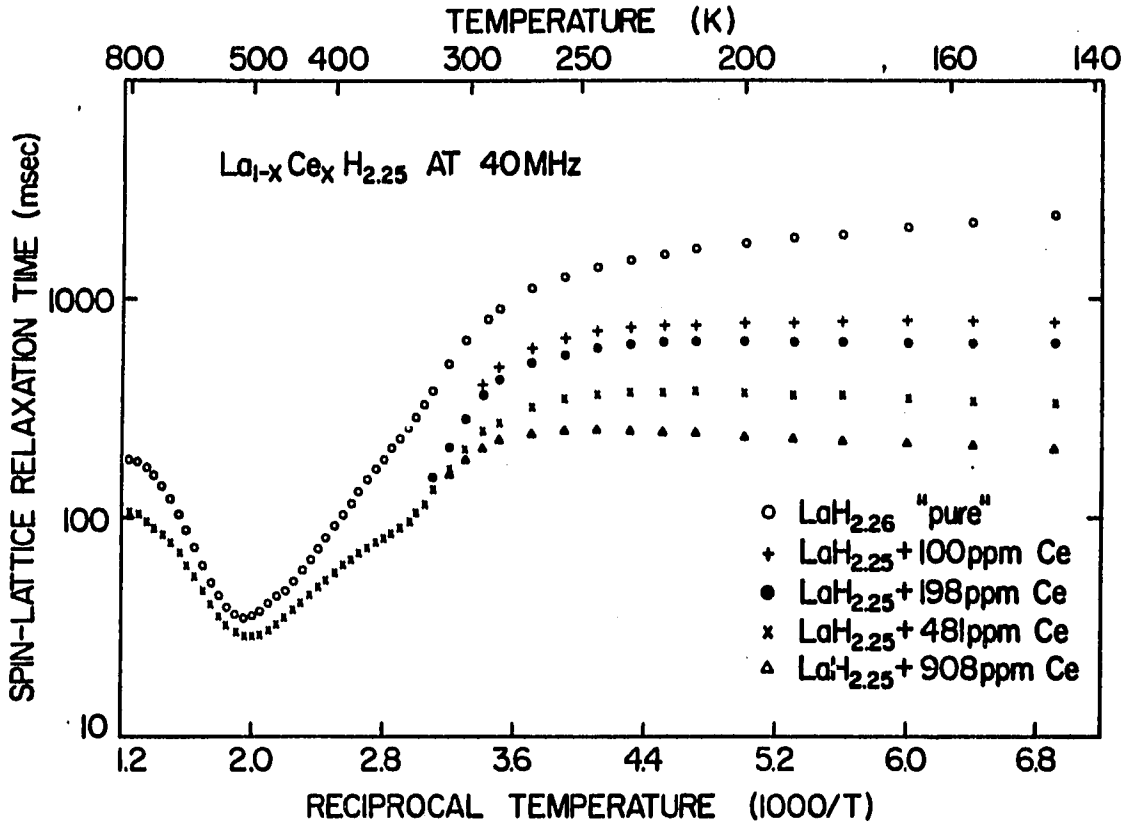

Figure 5-24. The temperature variation of the proton spin-lattice relaxation time T_1 in $La_{1-x}Ce_xH_{2.25}$ samples with X = 100, 198, 481, and 908 ppm. The results for sample $LaH_{2.26}$ with a negligible level of Ce^{3+} ions is also plotted here for comparison. The data points for all Ce^{3+}-doped samples coincide within experimental error above 320K and are not therefore shown separately

shows very little or no sign of the presence of the subsidiary minimum.

Just as in the previous two cases ($Y_{1-x}Gd_xH_{1.98}$ and $La_{1-x}Gd_xH_{2.25}$), the relaxation rate due to the interaction of the protons with impurity ions Ce^{3+}, T_{1p}^{-1}, can be determined by subtracting the rates for the "pure" $LaH_{2.26}$ sample from the rates for the doped samples,

$$(T_{1p})^{-1} = (T_1)^{-1}_{measured} - (T_1)^{-1}_{pure}. \qquad (5\text{-}10)$$

The T_{1p}^{-1} values for various samples at T = 145K as a function of the Ce concentration are shown in Figure 5-25. It clearly illustrates a linear relation between T_{1p}^{-1} and Ce content; however, the straight line does not pass through the origin as one might have expected and as occurs in the cases of Gd^{3+} in $YH_{1.98}$ and $LaH_{2.25}$. This suggests that the relaxation rates T_{1p}^{-1} determined by Equation (5-10) are higher than their "true" values and leads one to suspect the reliability of the reported value of impurity content in the "pure" $LaH_{2.26}$ sample. It may not contain 15 ppm of Gd as indicated by the mass spectrometric analysis. It seems likely that the Gd impurity ions were not uniformly distributed throughout the starting La metal. Hence, there must be some suspicion that the portion of La metal used in preparing "pure" $LaH_{2.26}$ actually contains less Gd impurity than all the others. This may well be the major factor responsible for the absence of the subsidiary minimum and higher T_1 values in the "pure" sample.

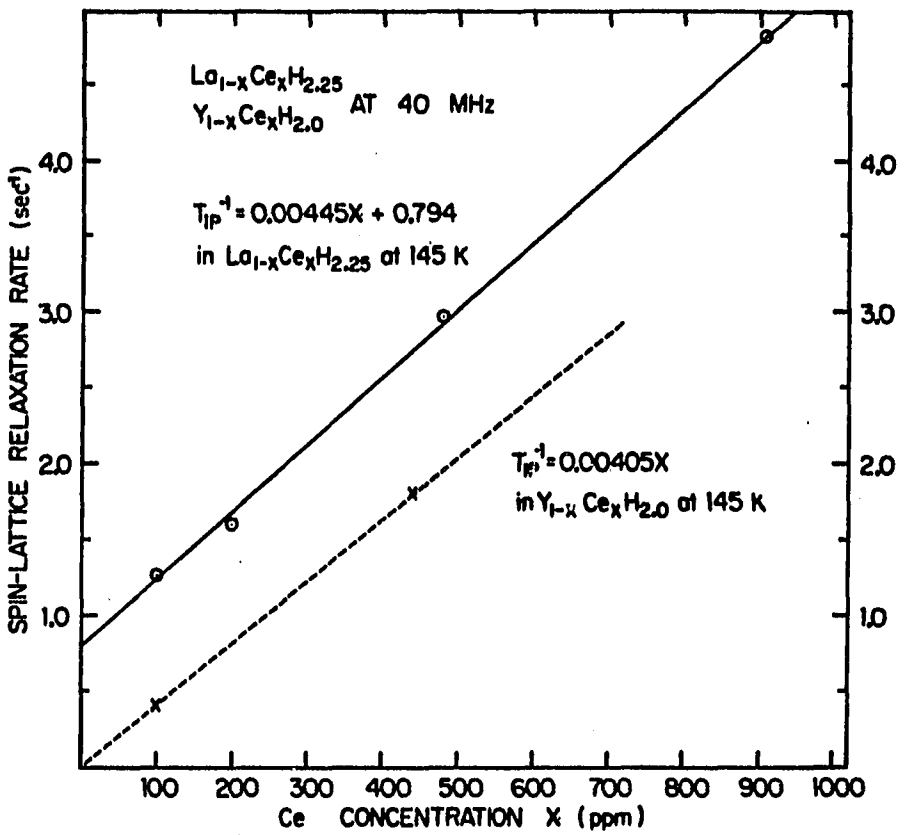

Figure 5-25. Spin-lattice relaxation rate T_{1p}^{-1} versus cerium concentration for $La_{1-x}Ce_xH_{2.25}$ at 145K. T_{1p}^{-1} values for $Y_{1-x}Ce_xH_{1.98}$ are also plotted for comparison (see Section G)

Since the T_1 values for the "pure" $LaH_{2.26}$ sample cannot reasonably be used in Equation (5-10), one has no better choice but to adopt the T_1 values for the 100 ppm Ce sample as the base value in determining the relaxation rate T_{1p}^{-1}, according to,

$$(T_{1p})^{-1} = (T_1)^{-1}_{\text{measured}} - (T_1)^{-1}_{100\ \text{ppm}}. \qquad (5\text{-}11)$$

The rates obtained by Equation (5-11) would be the relaxation rates due to the additional Ce content in these samples, i.e., 98 ppm, 381 ppm, and 808 ppm of Ce impurity.

A plot of the impurity ion induced relaxation rate $(T_{1p})^{-1}$, as determined by Equation (5-11), for the different Ce^{3+} concentrations is shown in Figure 5-26. The rates in the low temperature region have a stronger temperature dependence than in the Gd^{3+} case (Figure 5-21). An explanation for this observation will be given later in the section. Due to the ineffectiveness of Ce^{3+} at higher temperatures, the second and third regions, corresponding to slow and fast atomic diffusion, respectively, were not convincingly obtained. No discussion can be given nor conclusions drawn for these two regions at this time. (The increase of the rate in the 481 ppm Ce^{3+} sample for $10^3/T < 3.1$ in the figure is simply the result of uncertainties in the data when taking the small difference between two large measured quantities.)

Log-log plots of the relaxation time T_{1p} due to the Ce^{3+} impurity ions against temperature at low temperatures are shown in Figure 5-27.

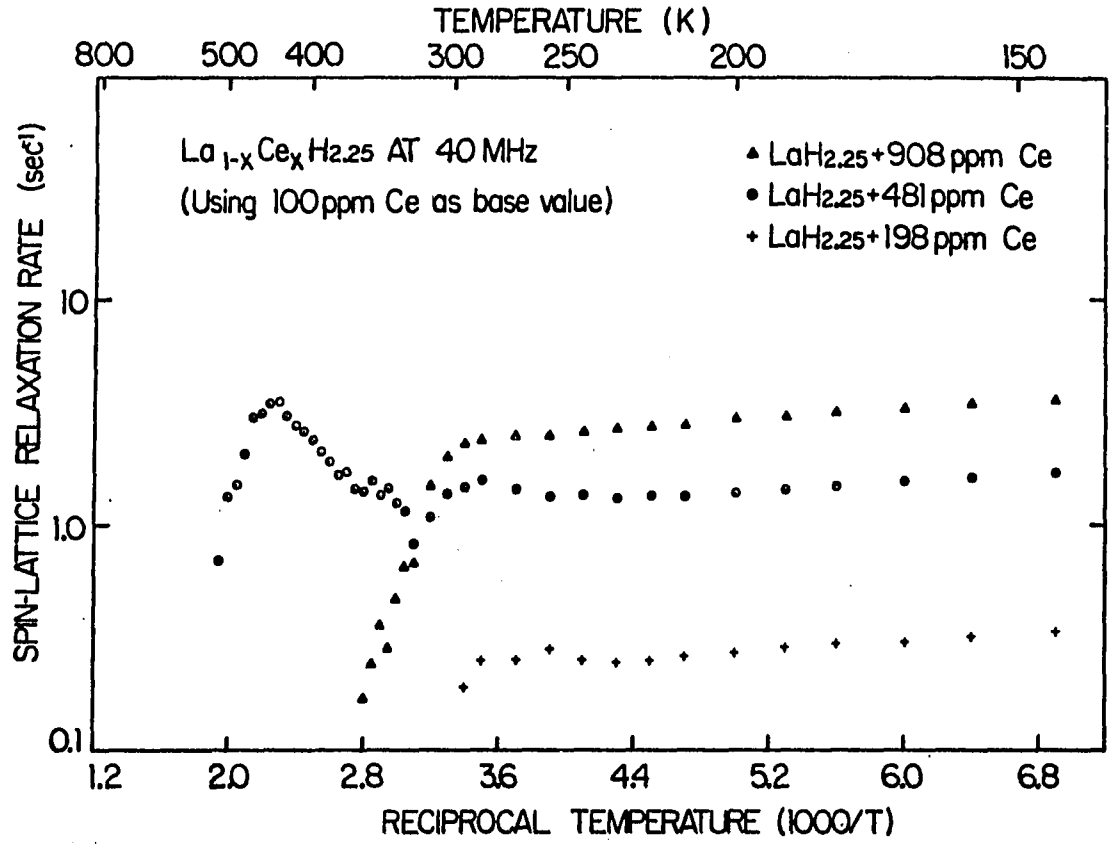

Figure 5-26. Logarithm of Ce^{3+} impurity induced relaxation rate, log T_{1p}^{-1}, versus reciprocal temperature $10^3/T$ in $La_{1-x}Ce_x H_{2.25}$ samples with X = 198, 481, and 908 ppm. Equation (5-11) was used to determine T_{1p}^{-1}. The additional Ce concentrations for the 198, 481, and 908 ppm samples become 98, 381, and 808 ppm. The irregularity of the data points for $10^3/T < 3.1$ in the figure is simply the result of uncertainties in the data when taking the small difference between two large measured quantities

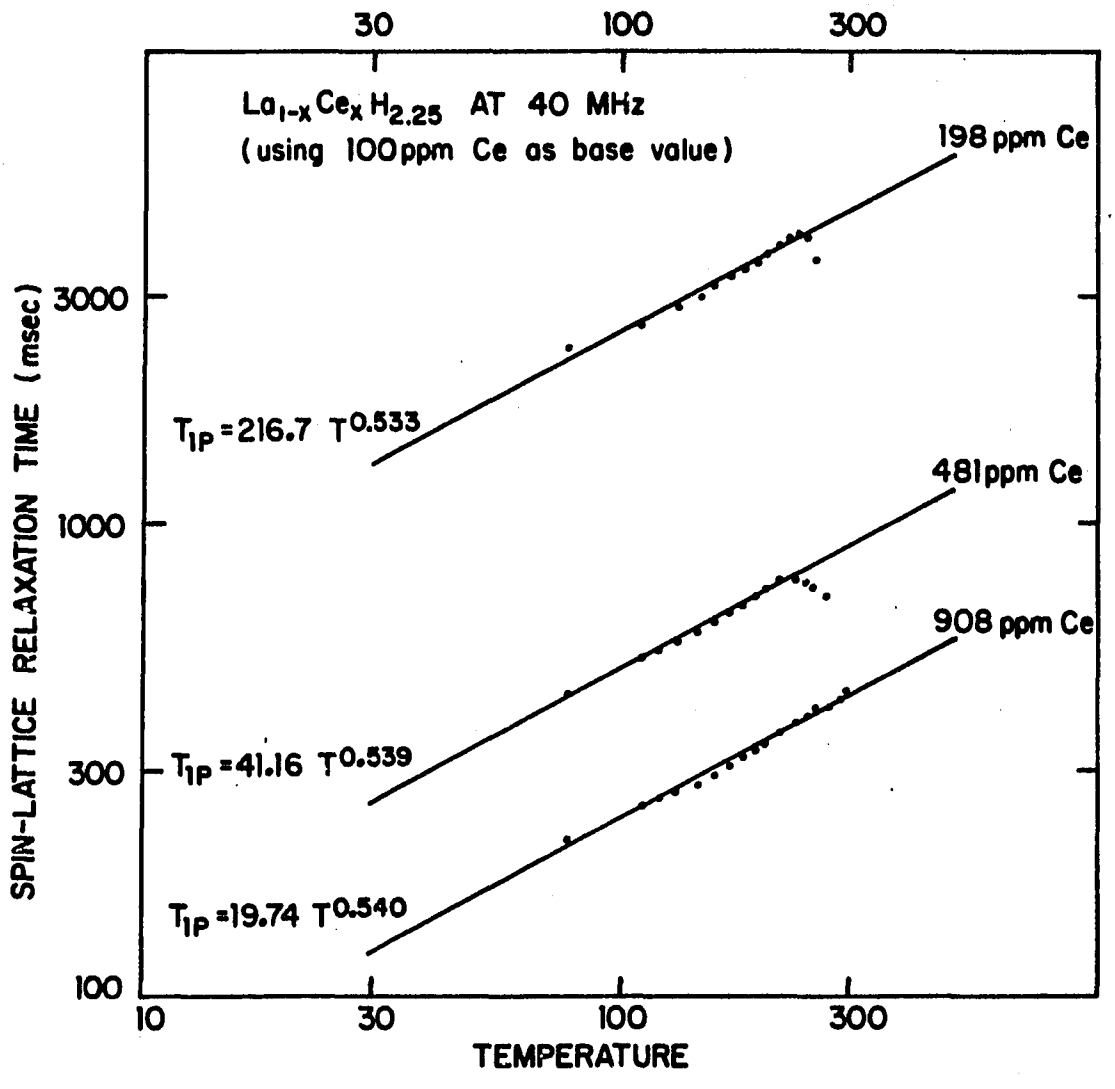

Figure 5-27. Logarithm of Ce^{3+} ion induced relaxation time, log T_{1p}, versus log T for $La_{1-x}Ce_xH_{2.25}$ samples with X = 198, 481, and 908 ppm in the spin diffusion region. The values of T_{1p} were determined by Equation (5-11), so that the effective concentrations are 98, 381, and 808 ppm. The lines are fit to the "straight line" portions of the data

The slopes are essentially the same for all compositions with an average relation of the form $T_{1p} \propto T^{0.54}$. This exponent is greater than that for Gd^{3+} in $LaH_{2.25}$. Within the context of spin diffusion relaxation, this corresponds to a dependence of the ionic spin-lattice relaxation time τ_i on temperature on the order of $\tau_i \propto T^{-2}$. This is not surprising, considering that CEF interactions surely contribute to the Ce^{3+} ion τ_i, making it both shorter and more strongly temperature dependent than that of Gd^{3+}.

G. Studies of $Y_{1-x}Ce_xH_{1.98}$

Two yttrium dihydride samples doped with Ce^{3+} impurity, 98 and 444 ppm, respectively, were also studied. Ames Laboratory Y-12381B metal which contains low levels of rare earth impurities (2 ppm Gd, 2 ppm Ce, 4 ppm Tb, and 4 ppm Pr) was used. The T_1 data are shown in Figure 5-28. Just as in the case of $LaH_{2.25}$, the Ce^{3+} ion is only effective in relaxing the proton spins in the low temperature region; however, it is not as effective as the Gd^{3+} ion. In the higher temperature range, for $T > 350K$, it is very ineffective. There is no detectable difference in the T_1 values for the two Ce^{3+} doped samples and the "pure" sample (i.e., that with 2 ppm Gd, 2 ppm Ce, 4 ppm Pr, and 4 ppm Tb) for temperatures higher than 600K. One might say that the Ce^{3+} ions are invisible to the diffusing hydrogen in that temperature range.

No indication of a subsidiary minimum on the low temperature side of the principal T_1 minimum can be seen; however, a change of slope is convincingly observed. In the temperature range $350K < T < 500K$,

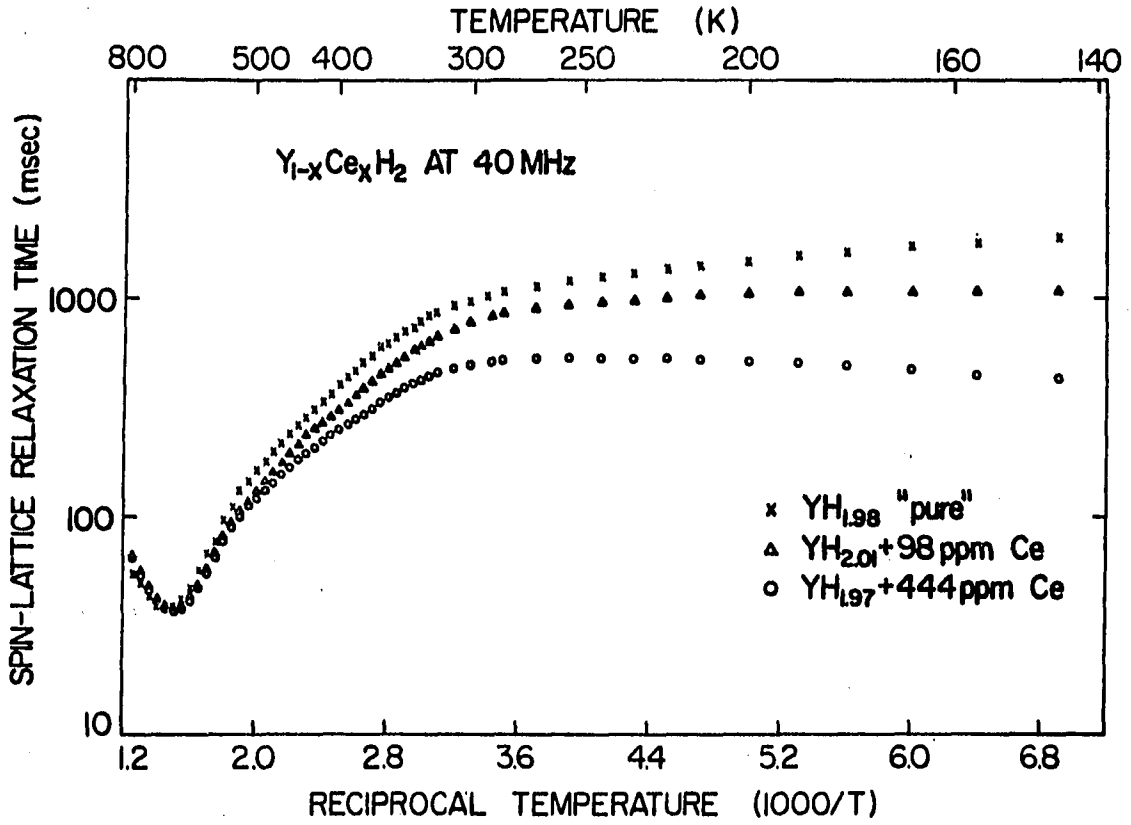

Figure 5-28. Composite plot of log T_1 versus $10^3/T$ for the $Y_{1-x}Ce_xH_2$ samples (X = 98 and 444 ppm) and the "pure" $YH_{1.98}$ sample

this slope decreases as Ce^{3+} concentration increases. Thus, one might say that the apparent activation energy for hydrogen diffusion decreases with increasing Ce^{3+} concentration.

This unusual observation raises serious doubts as to the validity of any interpretation based on two separate (independent) sub-lattice relaxation mechanisms in these hydrides. It is not unreasonable to believe that a single activation energy would be found in this temperature range if an "impurity free" sample were available.

Since the Ce^{3+} ions appear to be invisible to hydrogen and are ineffective in relaxing the nuclear spins at high temperatures (T > 500K), one can obtain a fairly reliable activation energy (E_{act} = 0.45 eV/atom) from the data in the vicinity of the principal diffusion minimum provided no other "high-temperature-effective" paramagnetic impurity ions such as Gd^{3+} are present. The depression of T_1 values at low temperatures (rigid-lattice regime), and the decreasing trend of the T_1 values at low temperatures are similar to those in the $La_{1-x}Ce_xH_{2.25}$ system.

The relaxation rates T_{1p}^{-1} contributed by the Ce^{3+} ions in the two samples are plotted in Figure 5-29 as a function of reciprocal temperature. A temperature dependent spin diffusion region for T < 250K is clearly evident. The relaxation times in this region have a stronger temperature dependence than in the $La_{1-x}Ce_xH_{2.25}$ system. In the second or intermediate temperature region (slow atomic diffusion), the apparent activation energy depends on the Ce^{3+} concentration. Hence, the

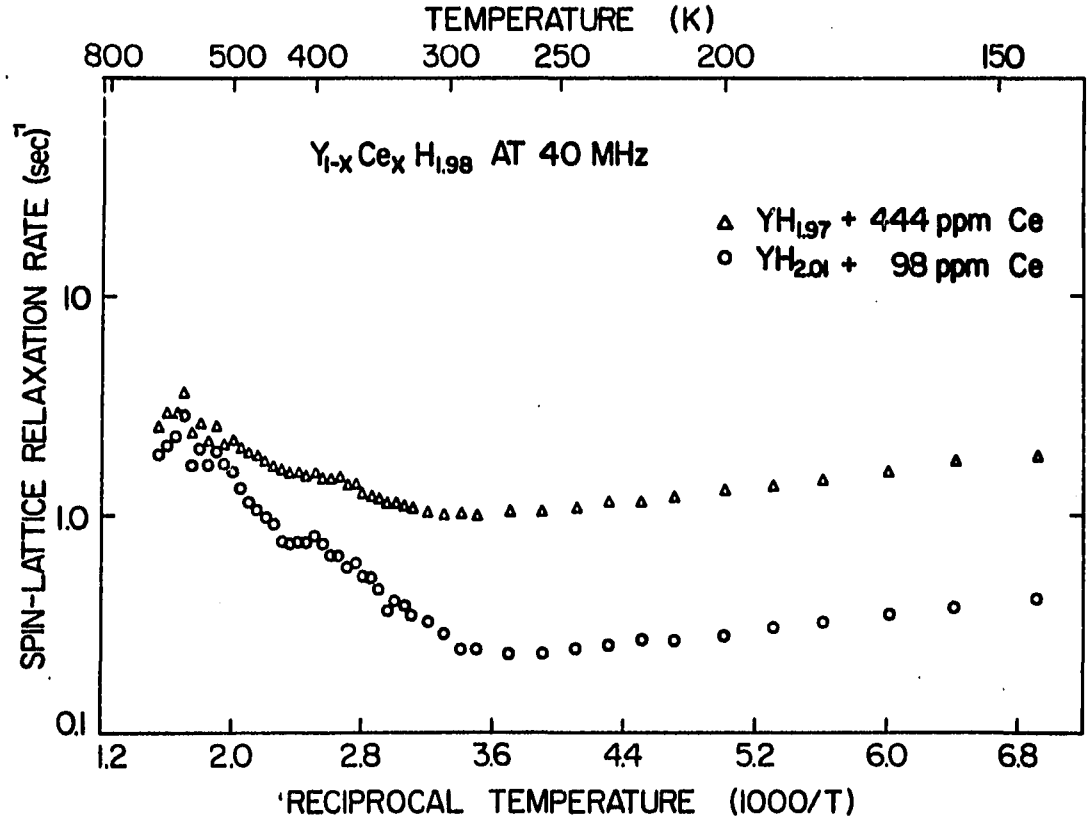

Figure 5-29. Logarithm of Ce^{3+} impurity induced relaxation rate, log T_{1p}^{-1}, against reciprocal temperature $10^3/T$ in $Y_{1-x}Ce_xH_{1.98}$ samples with X = 98 ppm and 444 ppm. The fast atomic diffusion region is not observed in either sample

modified form of Rorschach's equation (2-38) no longer appears to be appropriate. Due to the fact that the Ce^{3+} ions are not effective at high temperatures (T > 500K), the third region, that of fast atomic diffusion, is not observed at all.

To determine the relation between the relaxation time T_{1p} and the temperature, a log-log plot of T_{1p} against temperature is shown in Figure 5-30 for the spin diffusion region. A relation of the approximate form $T_{1p} \propto T^{0.80}$ is found. Comparing this result to that in the $La_{1-x}Ce_xH_{2.25}$ system, $T_{1p} \propto T^{0.54}$, the temperature dependence is seen to be substantially stronger in yttrium hydride.

As has already been noted, in the context of relaxation by slow spin diffusion (Equation 2-25), the temperature dependence of T_{1p} reflects directly the temperature dependence of the ion spin-lattice relaxation time τ_i, provided that $\omega_0^2\tau_i^2 \ll 1$, a condition which appears to be satisfied even for slowly relaxing ions like Gd^{3+}. Since, from Equation (2-25), $T_{1p} \propto C^{-1/4}$, and from Equation (2-23), $C \propto \tau_i$, one has $T_{1p} \propto \tau_i^{-1/4}$. If τ_i follows a Korringa law dependence, $\tau_i \propto T^{-1}$, and $T_{1p} \propto T^{1/4}$. In a similar way, for the fast spin diffusion limit (Equation 2-26), $T_{1p} \propto T^n$ where $\frac{1}{4} \leq n \leq \frac{5}{8}$. For Gd^{3+} in both $LaH_{2.25}$ and $YH_{1.98}$, we have seen that $T_{1p} \propto T^{0.16}$, approximately. For Ce^{3+}, in $YH_{1.98}$ however, we see that since $T_{1p} \propto T^{0.8}$, then $\tau_i \propto T^{-n}$ $(1.3 \leq n \leq 3.2)$ and similarly in $LaH_{2.25}$ we have $\tau_i \propto T^{-n}$ $(0.86 \leq n \leq 2.2)$. As discussed in Section F, the stronger temperature dependence of $\tau_i(Ce^{3+})$ reflects interactions with the CEF. The present measurements show that $\tau_i(Ce^{3+})$ depends more strongly on temperature in $YH_{1.98}$ than in $LaH_{2.25}$ and imply that CEF interactions are, therefore, stronger in $YH_{1.98}$ than in $LaH_{2.25}$. This may

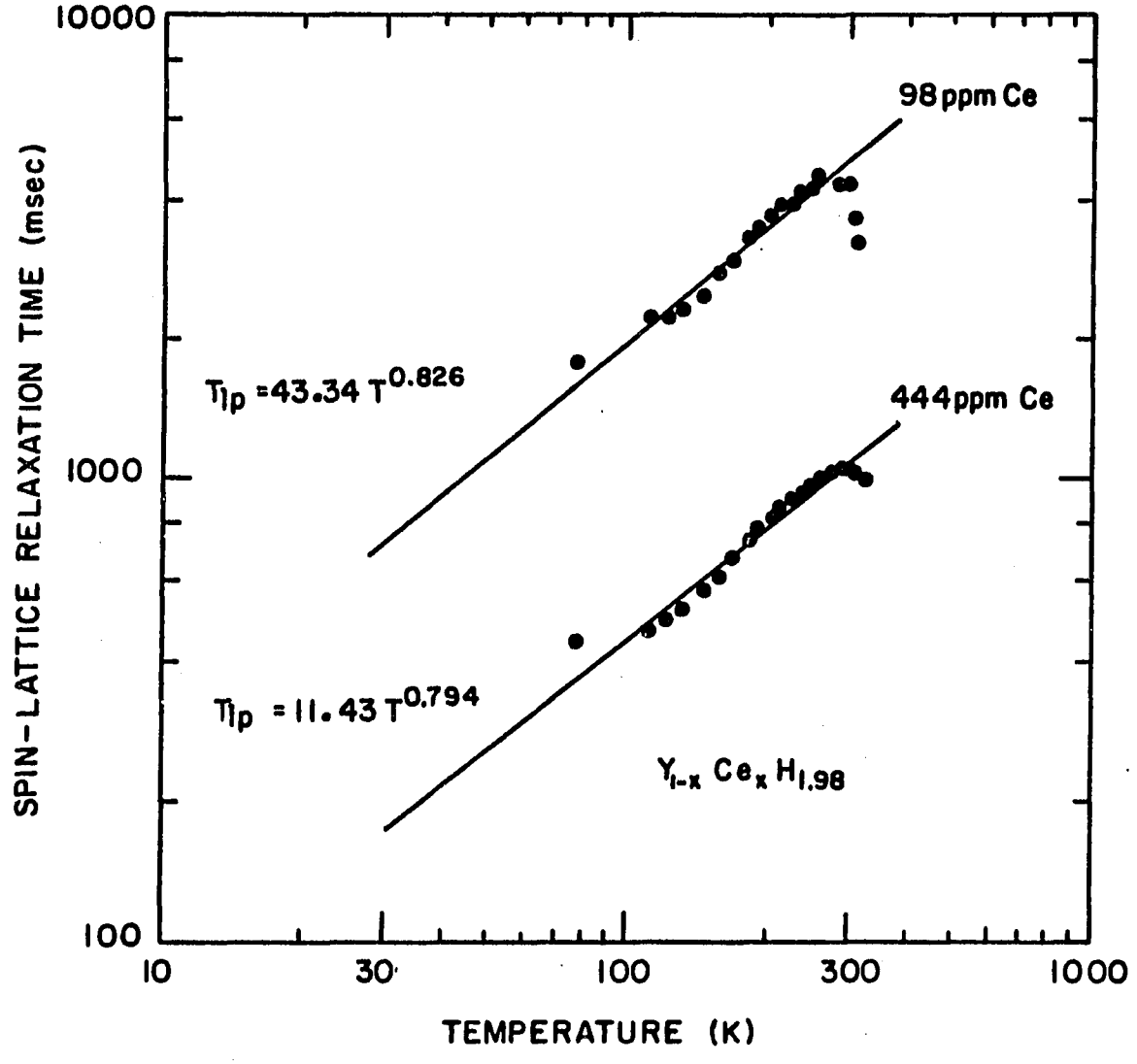

Figure 5-30. Logarithm of Ce^{3+} ion induced relaxation time log $T_{1\rho}$ versus log T for $Y_{1-x}Ce_xH_{1.98}$ samples with X = 98 and 444 ppm in spin diffusion region. The straight lines are best fit to the "straight line" portions of the data points measured

possibly be related to the significantly smaller lattice constant for YH_2, which is $\sim 0.4\text{Å}$ less than for either CeH_2 or LaH_2. In spite of this difference, it is interesting to note that the absolute magnitudes of T_{1p}^{-1} for the lanthanum and yttrium based systems are not very different from one another. For instance, as shown in Figure 5-25, both are given approximately by $T_{1p}^{-1} \simeq 0.004X$ at 145K.

H. Survey of $Y_{1-x}(RE)_xH_{1.98}$

Following the investigation of the effects of Gd^{3+} and Ce^{3+} on the proton T_1 in $YH_{1.98}$ and $LaH_{2.25}$, it seemed appropriate to conclude by making a brief survey of the effects of other rare earths in one of these host materials. $YH_{1.98}$ was chosen for this, and the impurities introduced were RE = Dy, Er and Nd, with X = 100 and 500 ppm. Leaving out samarium, these complete the sequence of ions with half-integral spin (Kramers ions). The Dy^{3+} and Er^{3+} impurities behave similarly to Gd^{3+} but with less effectiveness. All the T_1 features were reproduced over the entire temperature range investigated. For a clear comparison, the T_1 data for the yttrium hydrides with 100 ppm and 500 ppm of the five rare-earth dopants investigated are plotted in Figures 5-31 and 5-32, respectively.

The T_1 in the samples with Nd^{3+} dopant behaves very differently from that in the others. At low temperatures, the depression of T_1 is much more serious than for Ce^{3+}, Dy^{3+} and Er^{3+}, but it becomes much less pronounced than for Dy^{3+} and Er^{3+} at higher temperatures. For both the 100 ppm and 500 ppm Nd^{3+} doped samples, T_1 shows a weak

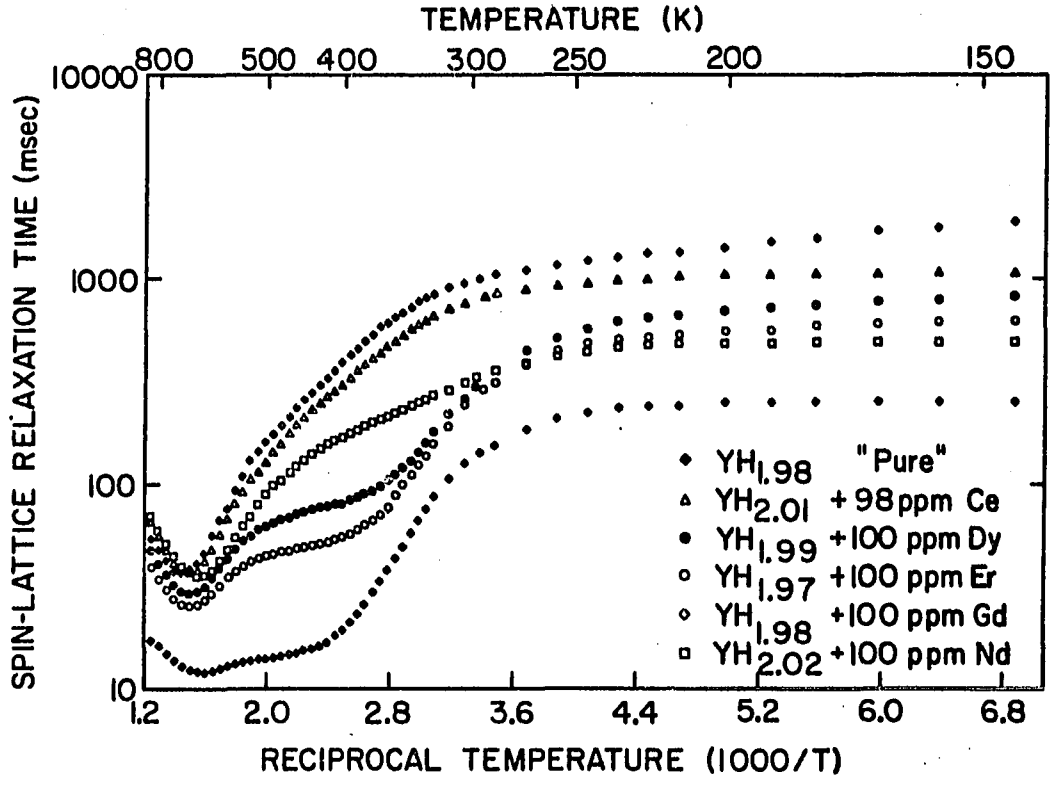

Figure 5-31. Composite plot of log T_1 versus $10^3/T$ for $Y_{1-x}(RE)_xH_2$ samples with X = 100 ppm and RE = Ce, Nd, Gd, Dy, and Er. The results for the "pure" $YH_{1.98}$ sample are also shown for comparison

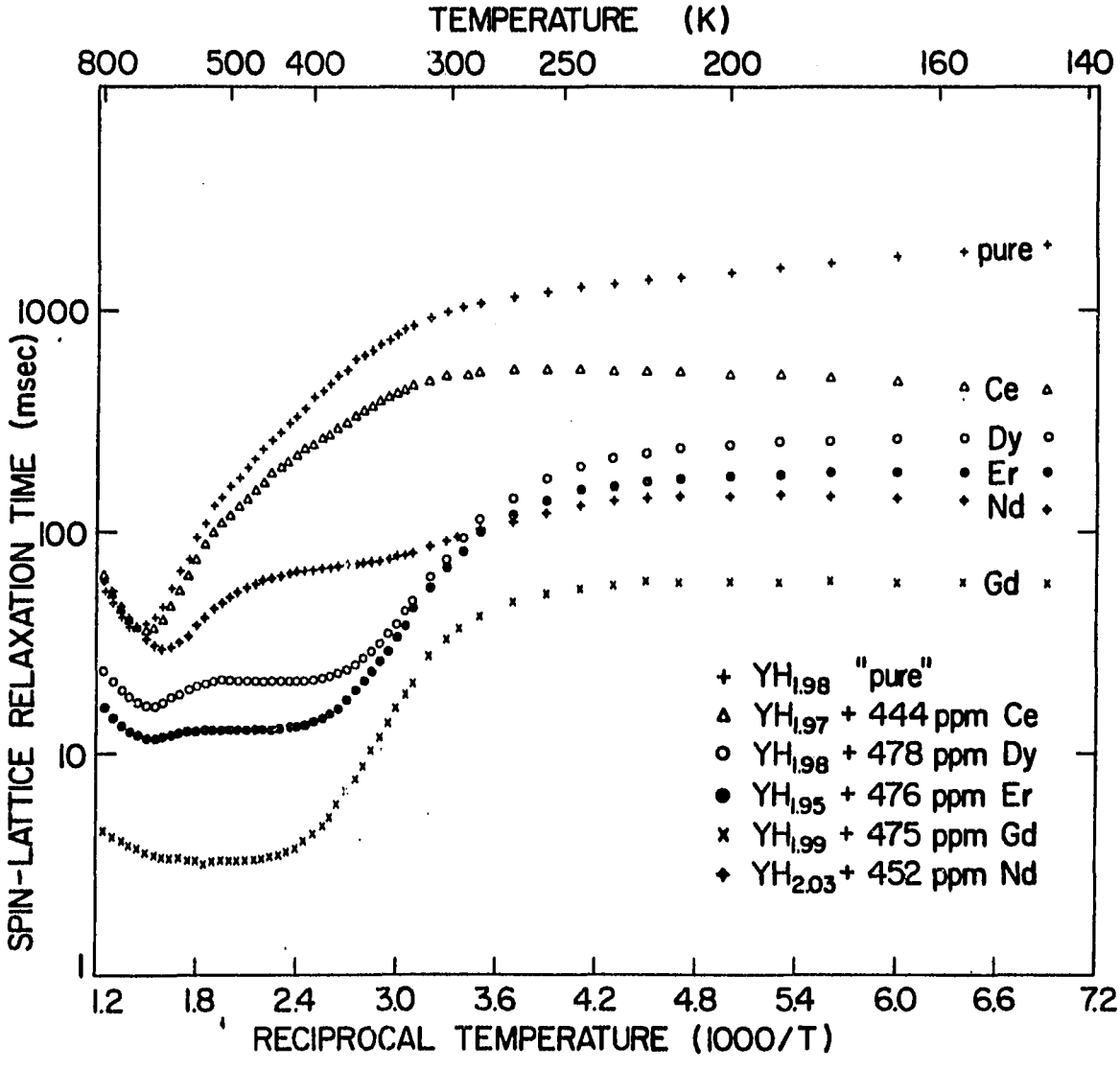

Figure 5-32. Composite plot of log T_1 versus $10^3/T$ for $Y_{1-x}(RE)_xH_2$ samples with $X \simeq 470$ ppm and RE = Ce, Nd, Gd, Dy, and Er. The results for the "pure" $YH_{1.98}$ samples are also shown for comparison

temperature dependence in the rigid-lattice regime, as do all the other depants. The depression of T_1 in this region is stronger than for any of the other dopants except Gd^{3+}. However, for temperatures higher than room temperature ($T \tilde{=} 300K$), Nd^{3+} becomes less effective. The subsidiary T_1 minimum on the low temperature side of the principal diffusion minimum can be clearly observed in the higher Nd^{3+} concentration sample. The depth of the subsidiary minimum is weaker than that of Dy^{3+}, Er^{3+} and Gd^{3+} dopants. In the lower Nd^{3+} concentration sample the subsidiary minimum only appears as a form of "slope-change". Thus, one becomes convinced that the "slope-change" effect is the weak form of the subsidiary (secondary) minimum. Its appearance is a function of both the type and concentration of impurity ions. On the high temperature side of the main diffusion minimum, Nd^{3+} becomes very ineffective and essentially invisible to the hydrogen, no sign of depression being observed in this region. It should be noted that the hydrogen concentration in the Nd^{3+}-doped samples is somewhat higher (H/Y = 2.02) than in the other samples. This contributes to a noticeable deepening of the principal T_1 minimum as well as to a shift of the minimum toward lower temperatures (compare Figures 5-32 and 5-4).

The impurity-induced relaxation rates T_{1p}^{-1} for the Nd^{3+}, Dy^{3+}, and Er^{3+}-doped samples are plotted against reciprocal temperature in Figures 5-33, 5-34, and 5-35, respectively. The results for the samples containing Er^{3+} and Dy^{3+} are similar to those with Gd^{3+} impurity, but the rates are relatively smaller than with Gd^{3+}. Three

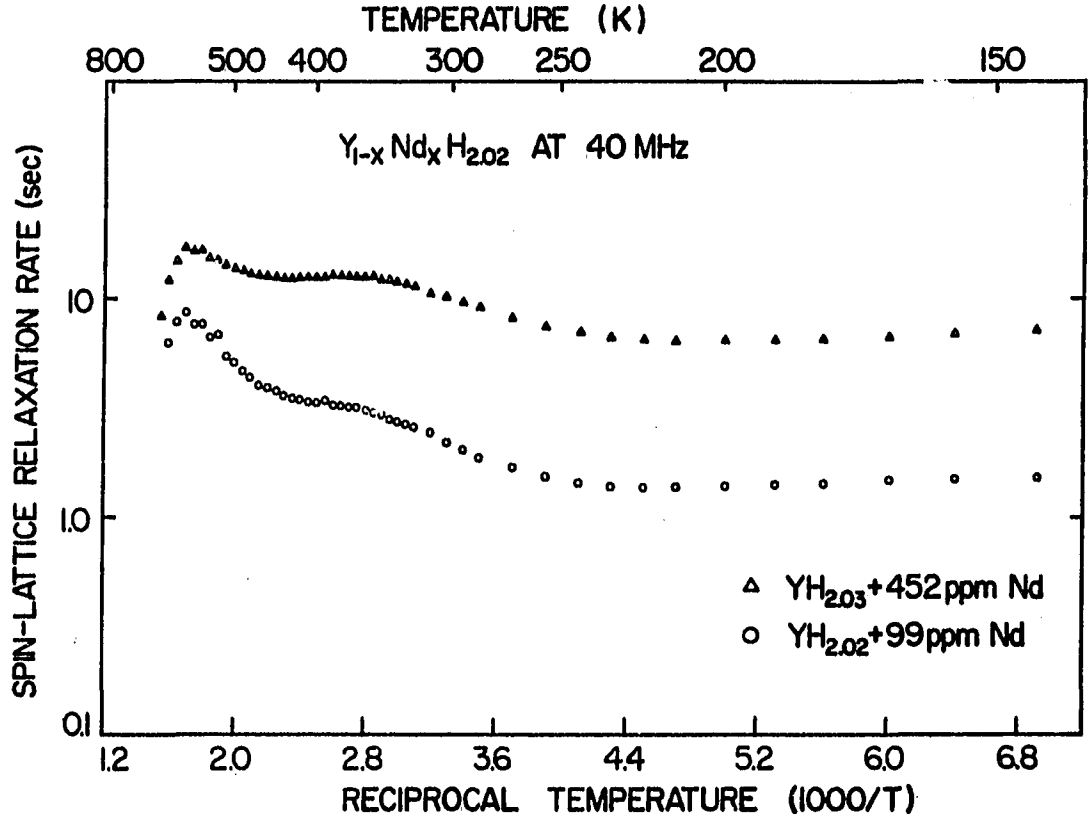

Figure 5-33. Nd^{3+} impurity induced relaxation rate, log T_{1p}^{-1}, versus reciprocal temperature, $10^3/T$, for $Y_{1-x}Nd_xH_{2.02}$ samples with X = 99 ppm and 452 ppm. No indication of the third region (fast atomic diffusion) was obtained

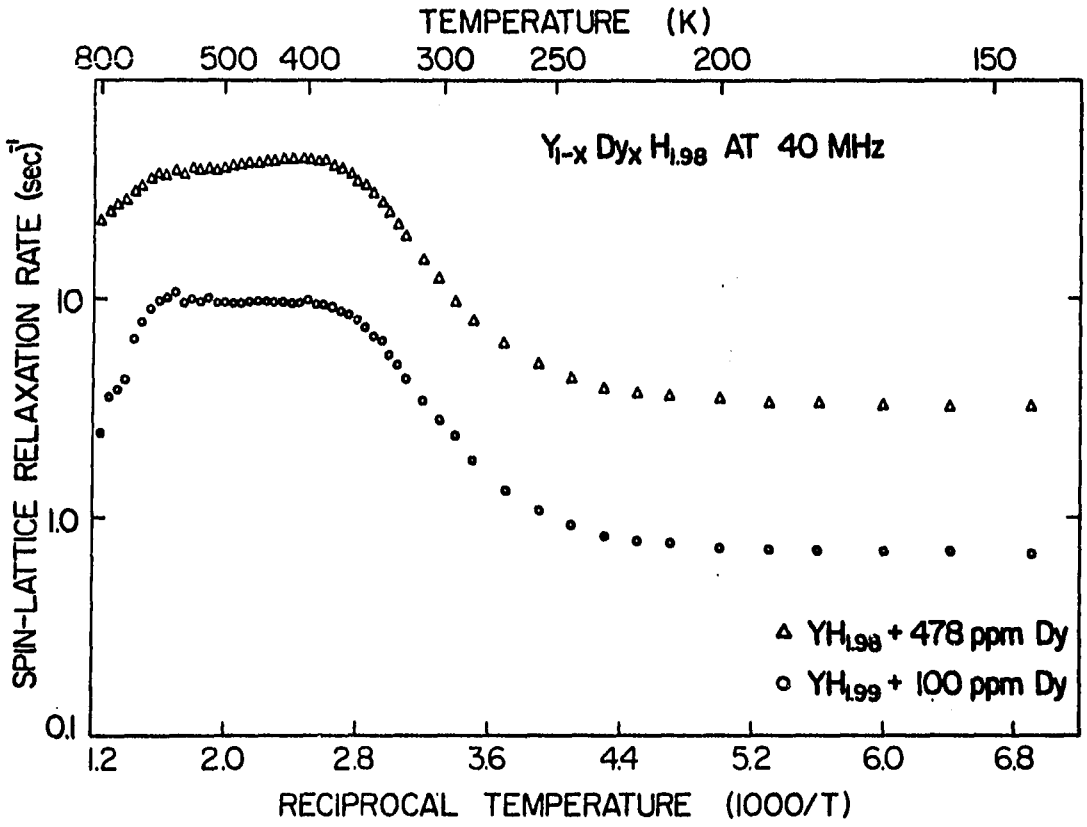

Figure 5-34. Logarithm of relaxation rate induced by Dy^{3+} impurity, log T_{1p}^{-1}, versus reciprocal temperature $10^3/T$ for 100 ppm and 478 ppm Dy^{3+} doped yttrium dihydride samples

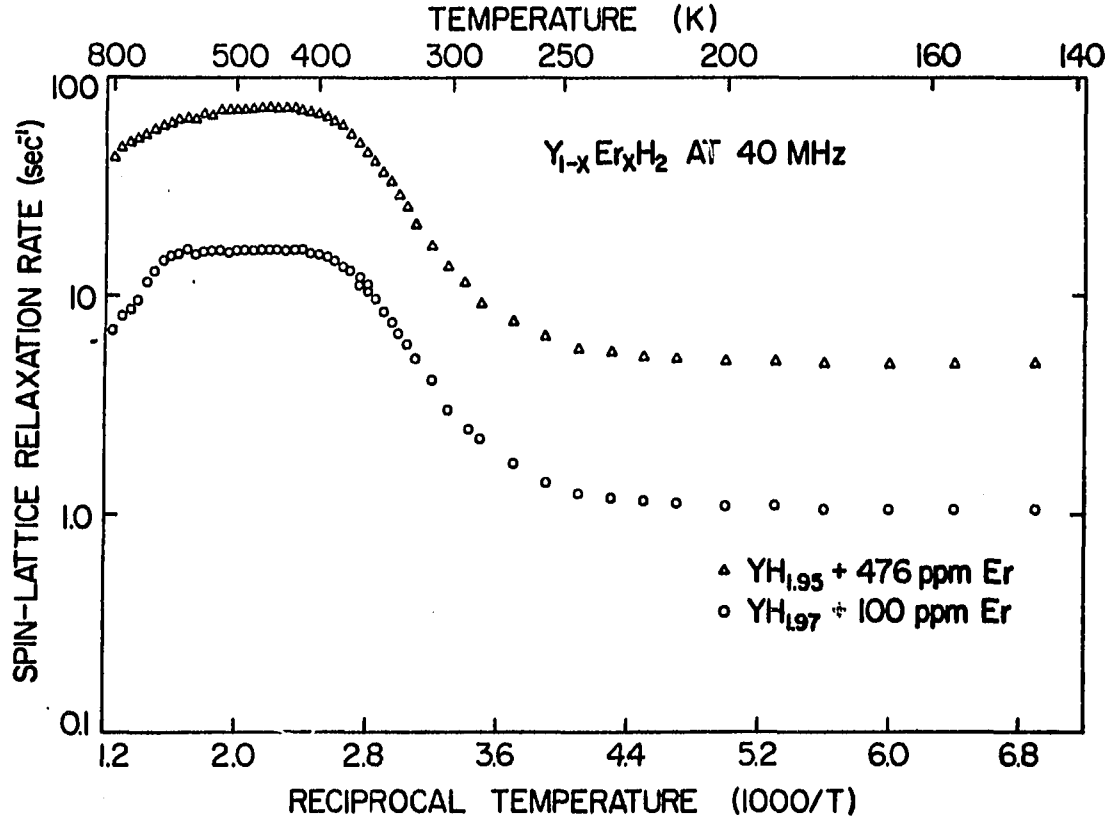

Figure 5-35. Logarithm of relaxation rate induced by Er^{3+} impurity, log T_{1p}^{-1}, against $10^3/T$ for 100 and 476 ppm of Er^{3+} doped yttrium dihydride samples

regions showing different temperature dependences are again obtained for these two systems, i.e., spin diffusion in the low temperature range ($T \lesssim 300K$), slow atomic diffusion at intermediate temperatures ($300K \lesssim T \lesssim 400K$), and finally fast atomic diffusion for $T \gtrsim 400K$. This distinct three-region character was not observed for the Nd^{3+} doped systems, due to the ineffectiveness of the Nd^{3+} ions at higher temperatures.

The temperature dependence of T_{1p} in the low temperature region for these three systems is shown in Figures 5-36, 5-37, and 5-38. The relations are as follows:

$$Nd^{3+};\ T_{1p} \propto T^{0.22} \quad (T<200K)$$

$$Dy^{3+};\ T_{1p} \propto T^{0.37} \quad (T \lesssim 140K)$$

$$Er^{3+};\ T_{1p} \propto T^{0.81} \quad (T \lesssim 130K)$$

It is clear from Figures 5-37 and 5-38 that not too much weight should be attached to the exponents derived for the Er^{3+} and Dy^{3+} doped samples. Table 5-6 summarizes the $T_{1p}^{-1}(T)$ results in the low temperature region for the samples with 100 ppm and 500 ppm of all the various dopants.

The spin-lattice relaxation rate induced by the impurity ions, T_{1p}^{-1}, for the $Y_{1-x}(RE)_xH_{1.98}$ systems at T = 145K are plotted against the rare-earth concentrations for various dopants with $X \simeq 100$ ppm and 500 ppm in Figure 5-39. The rates are linearly proportional to the impurity contents; the graphs all pass through the origin for zero

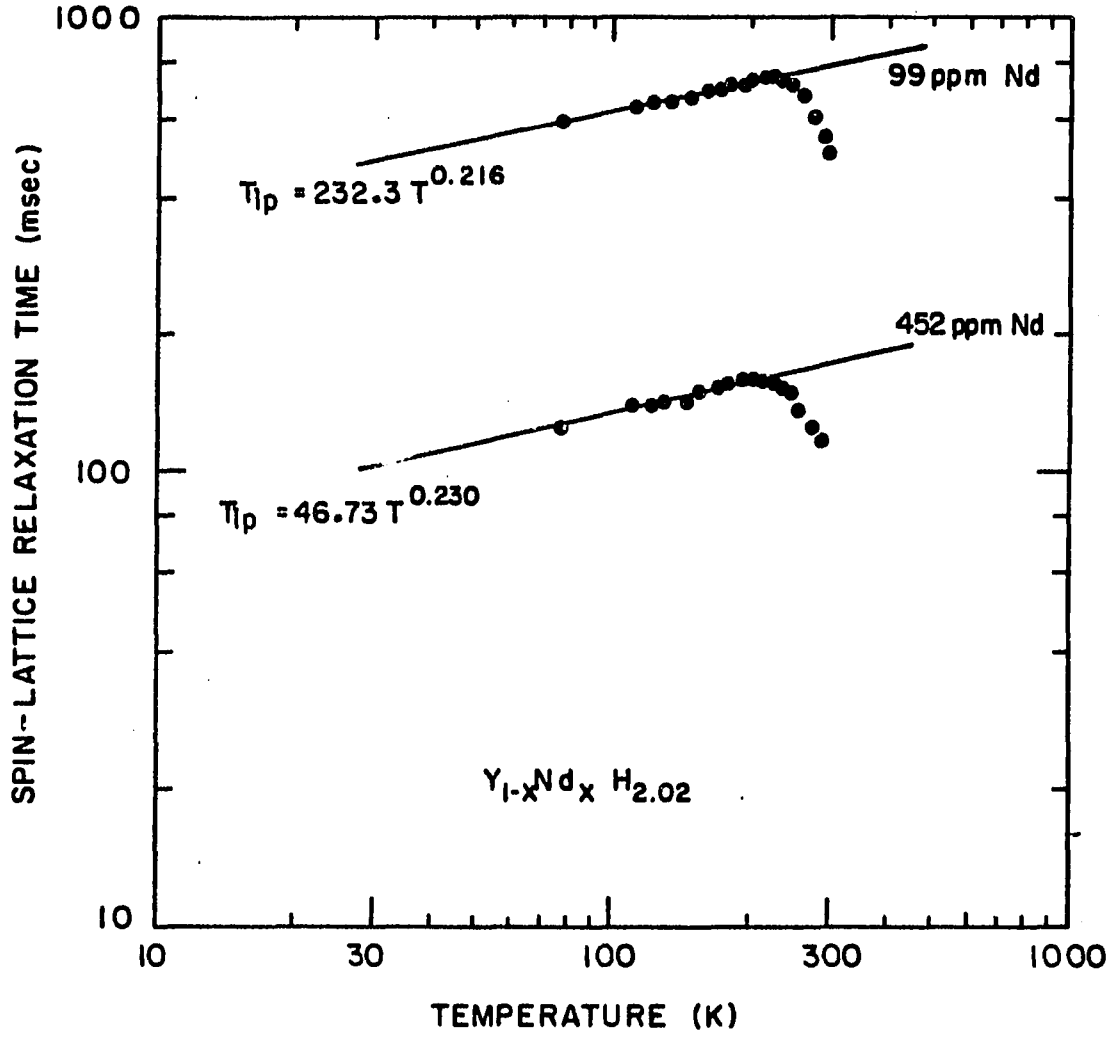

Figure 5-36. Logarithm of Nd^{3+} ion induced relaxation time, log T_{1p}, versus log T for $Y_{1-x}Nd_xH_{2.02}$ samples with X = 99 and 452 ppm in the spin diffusion region. The solid lines have been fit to the "straight line" portion of the data

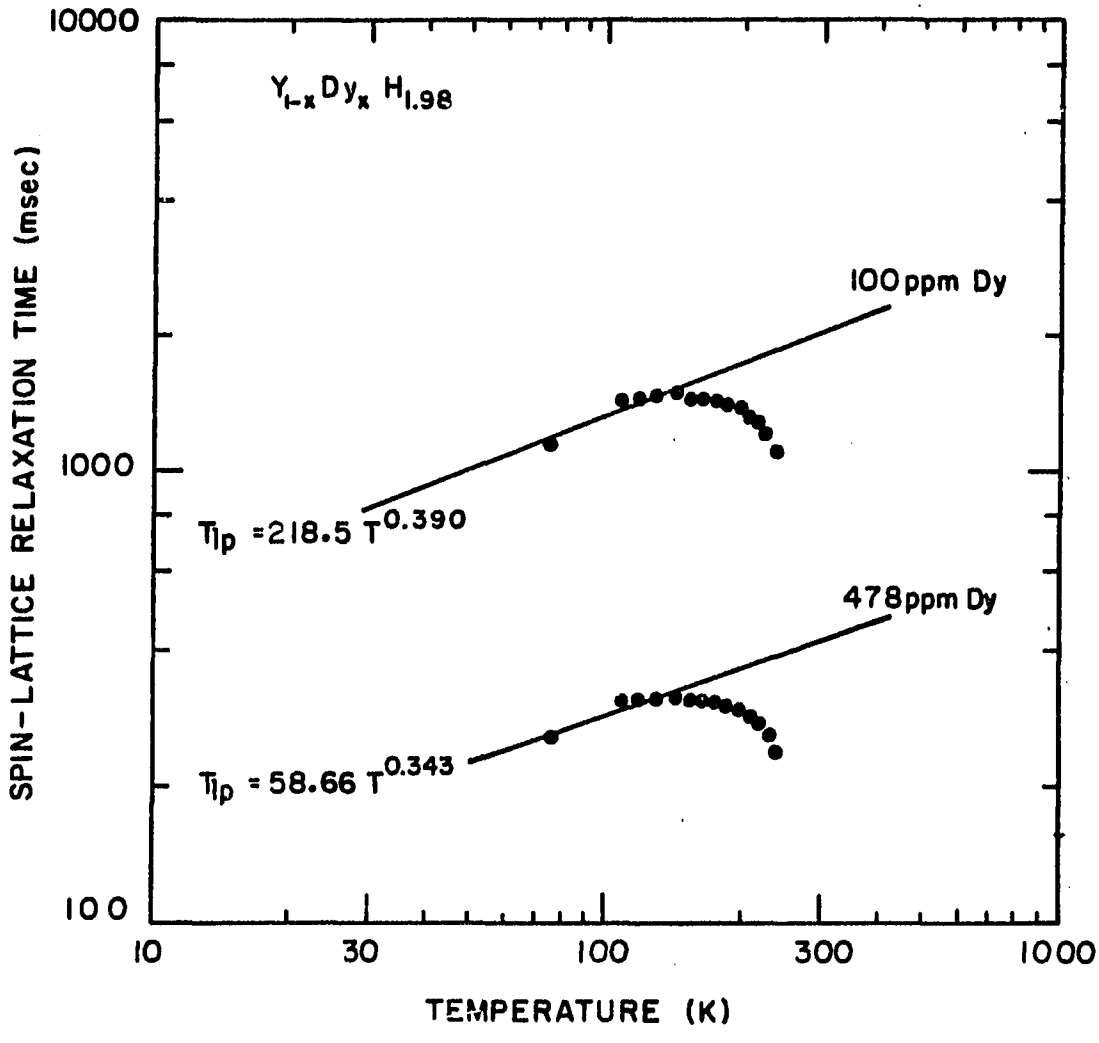

Figure 5-37. Logarithm of Dy^{3+} ion induced relaxation time, log T_{1p}, versus logarithm of temperature T in $Y_{1-x}Dy_xH_{1.98}$ samples with X = 100 and 478 ppm. Straight lines are fit to the four lowest temperature points only

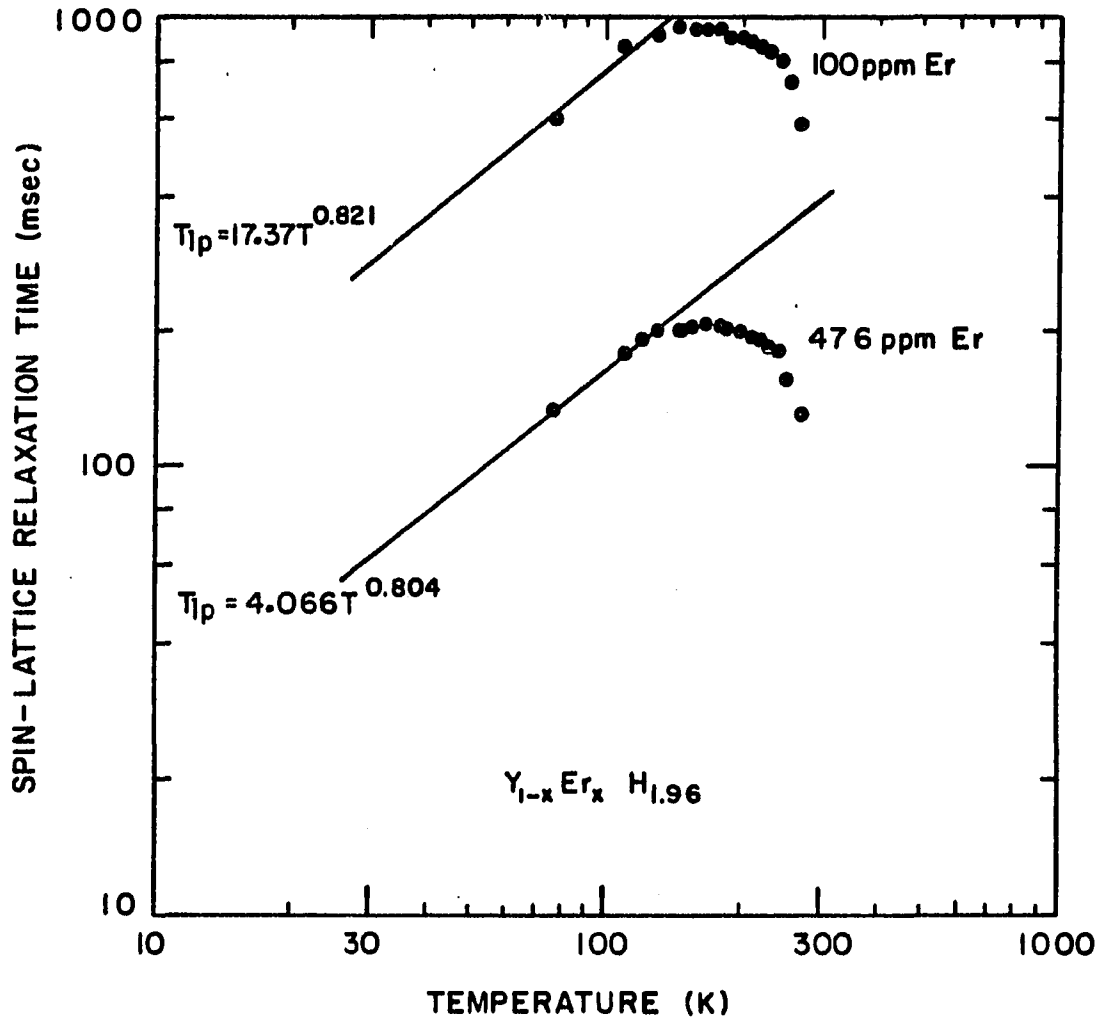

Figure 5-38. Logarithm of Er^{3+} ion induced relaxation time, log T_{1p}, against logarithm of temperature T for $Y_{1-x}Er_xH_{1.96}$ samples with X = 100 and 476 ppm in the rigid-lattice regime. The straight lines are the least-squares fit to the four lowest temperature points only; not too much significance should be attached to the exponents derived

Table 5-6. Summaries of the impurity ion induced relaxation rate $T_{1p}^{-1}(T)$ in the low temperature region for $Y_{1-x}(RE)_xH_{1.98}$ samples with 100 ppm and 500 ppm of all the various dopants. The coefficients in 500 ppm column for 444 ppm to 478 ppm are adjusted for X = 500 ppm

	Impurity-induced relaxation rate, $T_{1p}^{-1}(T)$[a]	
Dopant	X = 100 ppm	X = 500 ppm
Ce^{3+}	$23.3\ T^{-0.83}$	$111\ T^{-0.79}$
Nd^{3+}	$4.3\ T^{-0.22}$	$23.7\ T^{-0.23}$
Gd^{3+}	$7.8\ T^{-0.17}$	$41.9\ T^{-0.17}$
Dy^{3+}	$4.6\ T^{-0.39}$	$17.8\ T^{-0.34}$
Er^{3+}	$57.5\ T^{-0.82}$	$258\ T^{-0.79}$

[a] Values of $(T_{1p})^{-1}$ are in $(sec)^{-1}$.

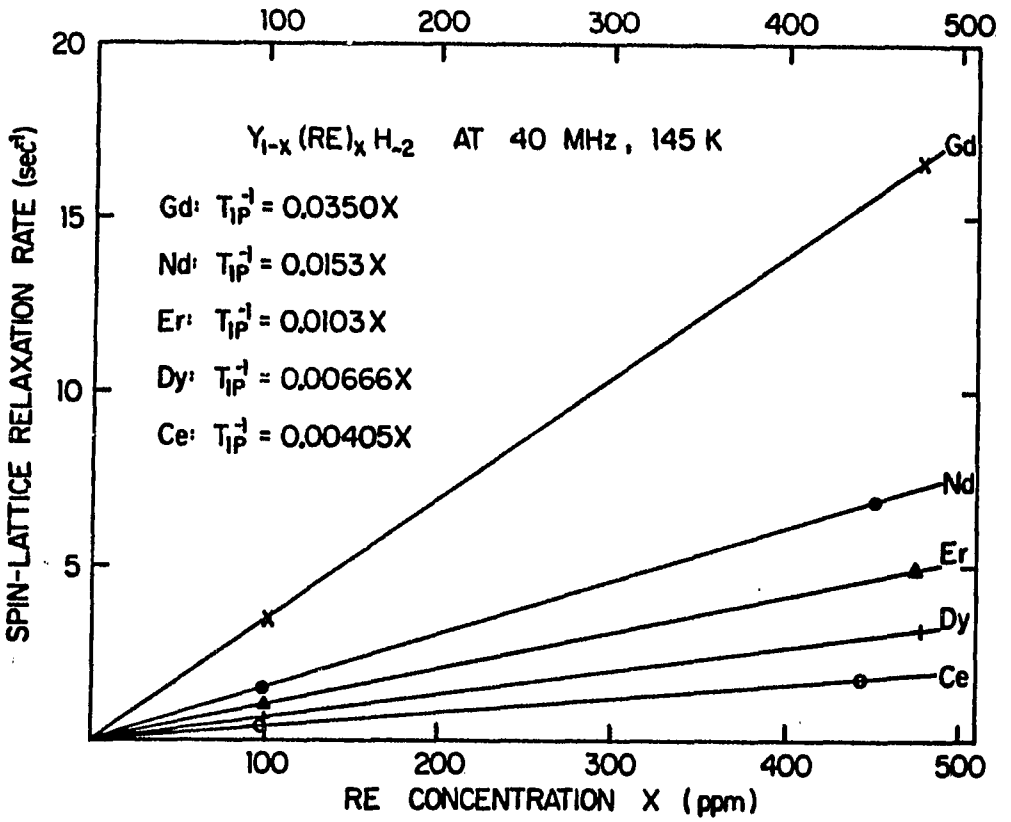

Figure 5-39. Composite plot of relaxation rate, T_{1p}^{-1}, versus the impurity concentration for $Y_{1-x}(RE)_xH_{1.98}$ samples at T = 145K

impurity as expected. At this temperature, Gd^{3+} is the most effective in relaxing proton spin, followed by Nd^{3+}, Er^{3+}, and Dy^{3+}, and Ce^{3+} is the most ineffective ion of all.

From the T_{1p} values in the spin diffusion region, one can estimate the spin-lattice relaxation time τ_i for these ions as a function of temperature by an iterative procedure using Equation (5-6), if one makes some assumption about the impurity moments. Taking the free ion values (which may not be correct because of CEF effects) the estimated values for the lowest temperature, 77K, are found and tabulated in Table 5-7. The Dy^{3+} and Ce^{3+} have the fastest relaxation times and Gd^{3+} is the slowest relaxing ion.

It is worth noting that the effectiveness of the various dopants follows the order, Ce < Dy < Er < Nd < Gd, at low temperatures and the order, Ce $\lesssim$ Nd < Dy < Er < Gd, in the high temperature region. According to the model of spin and atom diffusion to dipolar relaxation centers at low and high temperatures, respectively, the rank ordering of impurity ion effectiveness is controlled by two factors, the magnetic moment μ_p and spin-lattice relaxation time τ_i of the ions. The main problem in the detailed interpretation of the data is the lack of information about τ_i, and the conclusions must therefore be more qualitative. The similarity of the results for Gd, Dy, and Er is so close that the curves of Figures 5-34 and 5-35 fall rather well on a simple "universal" curve if they are simply displaced along the vertical axis appropriately, over the whole temperature range (140K $\lesssim$ T $\lesssim$ 600K)

Table 5-7. Estimated values of spin-lattice relaxation time at 77K for $Y_{1-x}(RE)_xH_{1.98}$ samples. The effective magnetic moments μ_p for these ions taken from the literature, are also listed here for comparison

Dopant	Ion spin-lattice relaxation time at 77K, τ_i (x 10^{-10} sec)	μ_p[a] (exp)
Gd^{3+}	3.78	8.0
Nd^{3+}	2.69	3.5
Er^{3+}	1.25	9.5
Ce^{3+}	1.0	2.6
Dy^{3+}	0.59	10.5

[a]Representative values taken from the literature, in units of the Bohr magneton.

for which we expect $T_{1p}^{-1} \propto C^{1/4}$. This implies that the $[\gamma_p^2 J(J+1)\tau_i]^{1/4}$ values are in the ratio 1:1.5:4.9 for Dy:Er:Gd, independent of temperature. This result appears to indicate that τ_i depends on temperature in the same way for all these ions. Theoretically, $\tau_i^{-1} = \tau_{iK}^{-1} + \tau_{iCEF}^{-1}$, where τ_{iK}^{-1} is the Korringa contribution and τ_{iCEF}^{-1} that due to interaction with phonons. The former is presumed to be the only important term for Gd, but the latter could be expected to change much more rapidly with temperature than the Korringa term at temperatures below the Debye temperature (180 $\sim$ 200K). This "scaling" property for these different ions is therefore rather surprising.

The constant scaling factor ($C^{1/4}$) ceases to apply in the fast atomic diffusion limit where eventually $T_{1p}^{-1} \propto C$; this is presumed to be the reason for the rapid fall of T_{1p}^{-1} for Er and even more so for Dy above 600K. It must also fail at low enough temperatures, because the onset of the fast spin diffusion regime would destroy the simple $C^{1/4}$ proportionality and would set in at different temperatures for the three ions. (The factor $1 + \omega_0^2\tau_i^2$ in C would also break down the simple scaling property if $\omega_0\tau_i$ approaches unity, but this is probably only important for T $\sim$ 25K or less.)

The behavior of T_{1p} for Ce might possibly be explained by a valence change from Ce^{3+} to (nonmagnetic) Ce^{4+} with increasing temperature; however, although Ce^{4+} is known to exist in some circumstances (always at low temperature), there seems to be no particular

reason to expect its occurrence here. Moreover, T_{1p} induced by Nd behaves in a manner similar to that for Ce (Figures 5-33 and 5-29) and no such mixed-valence property can be called on for it. Instead, we note that $\gamma_p^2 J(J+1)$, equivalently μ_p^2 (Table 5-7), is about one order of magnitude smaller for Ce^{3+} and Nd^{3+} than for the other three ions, and suppose further that Ce^{3+} and Nd^{3+} in YH_2 relax very rapidly at any case above room temperature. We consider the effect for the slow atomic diffusion region. With increasing temperature this region begins when $\tau_D \sim T_2$ and ends when $\tau_D \sim \frac{a_1^6}{C}$, $a_1 = \frac{\sqrt{3}a_0}{4}$, as discussed in Section D of this chapter. For ions with small enough μ_p^2 and τ_i, it is conceivable that the temperature interval between these two limits may become extremely short or even nonexistent. On leaving the spin diffusion region, one may already have reached the condition $\delta_a \sim 1$ where $\delta_a = \beta^2/2a_1^2$ and $a_1 = \frac{\sqrt{3}a_0}{4}$ (Equation 2-39). Then one would observe a behavior intermediate between $T_{1p}^{-1} \alpha C^{1/4} D_A^{3/4}$ and $T_{1p}^{-1} \alpha C$, resulting in slopes of log (T_{1p}^{-1}) vs $10^3/T$ curves shown in Figures 5-33 and 5-29 which are less than that, 3/4 E_{act}, found for the slower relaxing ions (see, for instance, Section D). The unusual temperature dependence of T_1 for the Nd^{3+}-doped samples shown in Figures 5-31 and 5-32 would then require an extremely rapid change of τ_i with temperature, but a slow-relaxing ion at 77K as listed in Table 5-7.

Quantitative justification of these ideas must await further information on the states of the rare-earth ions in hydrides. In this connection, it is clear that magnetic susceptibility and electron spin

resonance experiments would be valuable, and in addition, further measurements of proton T_1 values both as a function of frequency ω_0 and at temperatures low enough that the predicted minimum for $\omega_0\tau_i \sim 1$ could be observed.

VI. CONCLUSIONS

The primary contribution which this investigation has made to the utilization of NMR in studies of metal hydrides has been the clear demonstration that the presence of paramagnetic impurity ions in concentrations so low as to have been heretofore regarded as insignificant can have marked effects on the temperature dependence of the proton spin-lattice relaxation time as well as on values of electronic structure and hydrogen diffusion parameters deduced from such measurements. Paramagnetic ions contribute an additional spin-lattice relaxation process which, in the yttrium and lanthanum hydrides, appears to be essentially due to the dipolar coupling between impurity and proton moments. Protons close to the impurity ion (relaxation center) are directly relaxed. At low temperatures, protons far from the relaxation center are relaxed by the mechanism of spin diffusion. At higher, intermediate temperatures hydrogen (atom) diffusion becomes more rapid than spin diffusion and takes over as the mechanism for transporting distant spins to the center. Both of these stages are diffusion limited in the sense that a single encounter with the paramagnetic center accomplishes relaxation. However, since atom diffusion increases greatly with increasing temperature, the impurity induced relaxation in the intermediate region may reach rates 20-30 times faster than at low temperature. At still higher temperatures, hydrogen diffusion becomes so rapid that the duration of individual encounters with impurity moments becomes too short for relaxation to occur.

Multiple encounters are required, and the relaxation rate passes through a broad maximum and then decreases slowly with further increasing temperature.

This behavior has been most clearly documented in this study for the Gd^{3+} ion introduced into both $YH_{1.98}$ and $LaH_{2.25}$ at controlled levels as low as 50 ppm atomic. Effects were also unambiguously observed in samples containing uncontrolled levels of paramagnetic impurities as low as 2-5 ppm. The introduction of controlled levels of Dy^{3+} and Er^{3+} yielded similar, but weaker proton relaxation rates. Although both these ions have stronger magnetic moments than Gd^{3+}, the measurements show that these ions themselves have shorter spin-lattice relaxation times than Gd^{3+}. Of all the ions investigated, Gd^{3+} was most effective in promoting proton relaxation because it is a "slow-relaxing" ion. This property is a consequence of the fact that Gd^{3+} is an S-state ion (i.e., spherical) and is, therefore, only weakly relaxed by the crystalline electric field (CEF), its relaxation being mainly due to coupling to the conduction electrons.

The light rare-earth ions Ce^{3+} and Nd^{3+} behaved quite differently from Gd^{3+}, Dy^{3+}, and Er^{3+}. Cerium, in particular, caused negligible proton spin relaxation at high temperatures, very weak relaxation in the intermediate region, but was effective at low temperatures. Qualitatively, this behavior may be attributed to the small magnetic moment of Ce^{3+} and to an extremely short spin-lattice relaxation time at high temperatures. Neodymium was more effective than Ce, Dy, or Er

at low temperatures, but like Ce became essentially ineffective at high temperatures. This brief survey shows that the impurity induced relaxation rate is sensitive to the properties of the impurity ion, as well as depending on the host hydride composition. In fact, it is abundantly clear that the various ions behave so differently that it is, indeed, dangerous to generalize as to what effects on the proton T_1 may be anticipated in specific hydrides when the actual impurity content is unknown. One is obliged to conclude that many such measurements already extant in the literature which have been interpreted in terms of unusual electronic structure and/or diffusion behavior are suspect and open to reinterpretation.

It may well be that the properties of the paramagnetic ion, especially its spin-lattice relaxation rate, can be effectively studied via the proton T_1 in hydrides containing controlled impurity dopings. The range of temperatures accessible in these measurements is 1-2 orders of magnitude greater than that typically available in electron spin resonance studies. Moreover, the non-Kramers ions (e.g., Pr^{3+}, Tb^{3+}, etc.), most of which do not normally yield ESR signals, can also be studied via their effects on the proton T_1.

As remarked above, the impurity-induced relaxation makes it very difficult to extract unambiguously the NMR parameters characterizing the electronic structure (the Korringa constant, $K = T_{1e}T$) and hydrogen diffusion (jump frequency and activation energy). Regarding determination of K, it has been almost invariably assumed heretofore that

at low temperatures, the impurity induced rate, $(T_{1p})^{-1}$, is constant, i.e., temperature independent, and can be estimated by appropriate extrapolations of data from restricted temperature ranges. Yet, the measurements made in this study show that in every system investigated, $(T_{1p})^{-1}$ is temperature dependent, in some cases quite strongly. Even the purest samples showed evidence of departure from Korringa behavior at low temperatures consistent with relaxation by paramagnetic impurities. The measurements strongly suggest that by using a truly "pure" specimen or by correctly accounting for $T_{1p}(T)$, relaxation by the conduction electrons would, indeed, be found to follow the prescription, $T_{1e}T$ = constant, and, therefore, that the density of states, $N(E_F) \propto (T_{1e}T)^{-1/2}$, would also be found to be temperature independent. In the light of the results obtained here, conclusions about temperature variations of $N(E_F)$, based on apparent nonconstant $T_{1e}T$ behavior, must be regarded with considerable caution.

The impurity-induced relaxation has been shown to have profound effects on the apparent nuclear dipolar relaxation rate, $(T_{1d})^{-1}$. Already at impurity levels as low as 10 ppm in the case of Gd^{3+}, a subsidiary (secondary) minimum in the temperature dependence of the proton T_1 may appear, which may be readily misinterpreted in terms of a second motional process. Other impurity ions (e.g., Ce^{3+}) or lower impurity levels (Gd^{3+}) yield instead a characteristic "slope change" on the low temperature side of the principal T_1 minimum, which, in turn, may be construed in terms of a change in activation energy for

diffusion. The extreme effectiveness of the slow-relaxing ions (Gd^{3+}, etc.) in promoting spin relaxation at intermediate and high temperatures where atom diffusion is fast is responsible for the shortening of the measured proton T_1 in the vicinity of the diffusion minimum even when very low impurity concentrations are present. Hence, samples of nominal high purity can be expected to exhibit $T_{1,min}$ values shorter than expected on the basis of the nuclear dipolar interaction alone.

Despite these difficulties, the measurements made here on YH_x and LaH_x have yielded some firm conclusions regarding electronic structure and hydrogen diffusion. The purest sample of $YH_{1.98}$ yielded a Korringa constant, K = 295 sec-K, substantially greater than that found in the "20 ppm" Gd samples (~200 sec-K) and far greater than that reported by Kashaev, et al. (12) (~10 sec-K). The series of 20 ppm Gd samples ($1.81 \leq x \leq 2.03$) showed little variation in the $T_{1e}T$ product. Unfortunately, a corresponding series of samples was not prepared from the purer metal, but previous measurements (64) of K made on several samples prepared from higher purity yttrium yielded K = 280 sec-K. Therefore, the value K = 295 sec-K may be regarded as approaching the true value for $YH_{1.98}$, and further, the previous measurements as well as the present ones indicate that any variation of K, and therefore of $N(E_F)$, with hydrogen concentration must be slight, in agreement with heat-capacity measurements. In the case of

the lanthanum hydrides, slightly greater K values (∿310 sec-K) were obtained near the dihydride composition, with an increase, which is believed to be real, to about 500 sec-K as $x \to 2.5$, indicating a substantial decrease in $N(E_F)$ with increasing hydrogen concentration in this range. Such a decrease is consistent with the expected decrease in metallic character as the trihydride limit is approached.

Turning to the diffusion parameters, the uniform progression of the T_1 minimum toward lower temperatures with increasing hydrogen concentration shows unambiguously that at constant temperature hydrogen diffusion increases with increasing hydrogen content in both systems. This conclusion is clearly independent of the secondary minimum and slope-change effects seen in all the YH_x samples. The slope-change effects are less pronounced in the LaH_x samples, reflecting lower concentrations of slow-relaxing impurities.

The increase of hydrogen diffusion with hydrogen concentration in these two systems is to be contrasted with the opposite behavior (i.e., decreasing hydrogen diffusion with increasing hydrogen concentration) found in the dihydride phases of both Sc and Ti. Qualitatively, it is very tempting to ascribe this difference to the fact that octahedral site occupancy occurs in the case of Y and La but not in the case of Sc and Ti. However, despite the occurrence of hydrogen in the two interstitial sublattices, the T_1 data for the purest $LaH_{2.27}$ sample show no trace whatever of a second motional process or change in activation energy with temperature. This evidence, as well as the

fact that the subsidiary minimum seen in the yttrium dihydrides is clearly demonstrated to result from the Gd impurity content, shows that diffusion in the yttrium and lanthanum dihydrides is controlled by a single motional process. It seems likely that this motion involves O↔T and T↔O jumps, possibly by an interstitialcy-type process, e.g., simultaneous jump of an O,T pair of neighboring hydrogen atoms involving one adjacent vacant O-site (V):

$$O - T - V \rightarrow \overset{\frown}{x - x} - x \rightarrow V - T - O.$$

Using the simple BPP Lorentzian spectral density function to fit the $(T_{1d})^{-1}$ data, we find also that both the activation energy and jump frequency prefactor decrease with increasing hydrogen content in these systems. Qualitatively, one may speculate that increased occupancy of the O-sublattice causes the potential wells at the two types of sites to become shallower, thereby also lowering the energy barrier to motion between the two sublattices. The very high activation energy found for $YH_{1.81}$ (0.86 eV/atom) then suggests that O-site occupancy is very low at the low hydrogen concentration limit of the dihydride phase and increases rapidly with increasing hydrogen content.

VII. REFERENCES

1. C. A. McAuliffe, Hydrogen and Energy (Macmillan Press, New York, 1980).

2. J. Bockris, Energy Options (Halsted Press, Stroudsburg, Pa., 1980).

3. L. Williams, Hydrogen Power (Pergamon Press, Oxford, England, 1980).

4. P. Hoffmann, The Forever Fuel (Westview Press, Boulder, Colo., 1981).

5. R. G. Barnes, in Nuclear and Electron Spectroscopics Applied to Materials Science, edited by E. N. Kaufmann and G. Shenoy (Elsevier, North Holland, 1981).

6. R. M. Cotts, Ber. Bunsenges. Phys. Chem. 76, 760 (1972).

7. R. M. Cotts, in Hydrogen in Metals I. Basic Properties, edited by G. Alefeld and J. Völkl (Spring Verlag, Berlin, 1978).

8. R. M. Cotts, in Proceedings of the International Symposium on the Electronic Structure and Properties of Hydrogen in Metals, 4-6 March 1982, Richmond, Virginia.

9. E. P. Apgar, Ph.D. Thesis, Rutgers University, 1957.

10. H. T. Weaver, Phys. Rev. B5, 1663 (1972).

11. H. C. Torrey, Nuovo Cimento, Suppl. 9, 95 (1958).

12. R. S. Kashaev, E. F. Guduidullin, A. N. Gilmanov and M. E. Kost, Sov. Phys. Solid State 22, 530 (1980).

13. D. A. Cornell and E. F. W. Seymour, J. Less-Common Met. 39, 43 (1975).

14. C. Korn and D. Zamir, J. Phys. Chem. Solids 31, 489 (1970).

15. C. A. Sholl, J. Phys. C: Solid State Phys. 14, 447 (1981).

16. C. A. Sholl, J. Phys. C: Solid State Phys. 14, 1479 (1981).

17. Y. Fukai and S. Kazama, Acta Metallurgica 25, 59 (1977).

18. W. M. Mueller, J. P. Blackledge, and G. G. Libowitz, Metal Hydrides (Academic Press, New York, 1968), p. 443.

19. D. L. Anderson, R. G. Barnes, T. Hwang, D. T. Peterson and D. R. Torgeson, J. Less-Common Met. 73, 243 (1980).

20. D. Khatamian, W. Kamitakahara, R. G. Barnes and D. T. Peterson, Phys. Rev. B21, 2622 (1980).

21. D. Halliday and R. Resnick, Fundamentals of Physics (Wiley, New York, 1970).

22. N. Bloembergen, Nuclear Magnetic Relaxation (W. A. Benjamin, New York, 1961).

23. A. Abragram, The Principles of Nuclear Magnetism (Oxford University Press, New York, 1961).

24. C. Slichter, Principles of Magnetic Resonance (Harper and Row, New York, 1963).

25. N. Bloembergen, E. M. Purcell and R. V. Pound, Phys. Rev. 73, 679 (1948).

26. H. Selbach, O. Kanert and D. Wolf, Phys. Rev. B19, 4435 (1979).

27. J. Korringa, Physica 16, 601 (1950).

28. A. Narath, in Hyperfine Interactions, edited by A. Freeman and R. Frankel (Academic Press, New York, 1967).

29. C. Korn, Phys. Rev. B17, 1707 (1978).

30. N. Bloembergen, Physica 15, 386 (1949).

31. W. Blumberg, Phys. Rev. 119, 79 (1960).

32. G. Khutsishvili, Soviet Physics JETP 15, 909 (1962).

33. P. de Gennes, Phys. Chem. Solids 7, 345 (1958).

34. H. Rorschach, Jr., Physica 30, 38 (1964).

35. For a tabulation of the function, see Tables of Bessel Functions of Fractional Order, Vol. II, National Bureau of Standards (Columbia Univ. Press, New York, 1949).

36. L. Shen, Phys. Rev. 172, 259 (1968).

37. P. M. Richards, Phys. Rev. B18, 6358 (1978).

38. L. Lu, M.S. Thesis, Iowa State University (1982).

39. D. Adduci, P. Hornung and D. R. Torgeson, Rev. Sci. Instrum. 47, 1503 (1976).

40. J. Conway and R. Cotts, Rev. Sci. Instrum. 48, 656 (1977).

41. D. Adduci, P. Hornung and D. R. Torgeson, Rev. Sci. Instrum. 48, 661 (1977).

42. I. Lowe and C. Tarr, J. Phys. E1, 320 (1968).

43. T. Farrar and E. Becker, Pulse and Fourier Transform NMR (Academic Press, New York, 1971).

44. E. Fukushima and S. Roeder, Experimental Pulse NMR (Addison-Wesley Publishing Company, Inc., Reading, Mass., 1981).

45. C. P. Slichter, Principles of Magnetic Resonance (Springer-Verlag, Berlin, 1978).

46. See for example, K. Symon, Mechanics (Addison-Wesley Publishing Company, Reading, Mass., 1971).

47. D. S. Schreiber and R. M. Cotts, Phys. Rev. 131, 1118 (1963).

48. T. Hwang, R. Schoenberger, D. R. Torgeson and R. G. Barnes, Phys. Rev. B (1982) (in press).

49. K. Doolan, P. Narang and J. Pope, Phys. F: Metal Phys. 10, 2073 (1980).

50. J. Pope, P. Narang and K. Doolan, J. Phys. Chem. Solids 42, 519 (1981).

51. P. Hornung, Ph.D. Thesis, Iowa State University (1978).

52. R. Göring, R. Lukas and K. Bohmhammel, J. Phys. C: Solid State Phys. 14, 5675 (1981).

53. C. Korn, Phys. Rev. B17, 1707 (1978).

54. T. Phua, Physics Department, Iowa State University, unpublished results.

55. S. Vernon, P. Thayamballi, R. Hogg, D. Hone and V. Jaccarino, Phys. Rev. B24, 3756 (1981).

56. M. Belhoul, G. A. Styles, E. F. W. Seymour, T. Phua, R. G. Barnes, D. R. Torgeson and D. T. Peterson, J. Phys. F: Metal Physics (1982) (in press).

57. H. Drulis, Arch. Sci. (Geneva), 27, 243 (1974).

58. R. Bierig, M. Weber and S. Warshaw, Phys. Rev. 134, A1504 (1964).

59. S. Day, E. Otsuka and B. Josephson, Phys. Rev. 137, A108 (1965).

60. C. Huang, Phys. Rev. 139, A241 (1965).

61. T. Guzzle and P. Mahendroo, Phys. Rev. 150, 361 (1966).

62. E. Fukushima and E. Uehling, Phys. Rev. 173, 366 (1968).

63. R. G. Barnes, B. Beaudry, R. Creel, D. R. Torgeson and D. de Groot, Solid State Commun. 36, 105 (1980).

64. D. L. Anderson, R. G. Barnes, T. Y. Hwang, D. T. Peterson and D. R. Torgeson, J. Less-Common Metals 73, 243 (1980).

VIII. ACKNOWLEDGMENTS

The author would like to express his gratitude to his thesis advisor, Professor R. G. Barnes, for his guidance and advice throughout the entire progress of this investigation. His counsel, always available, along with patience and encouragement, was invaluable. Without Professor Barnes' helpful suggestions, this work would not have been possible.

Thanks are extended to Mr. D. R. Torgeson for providing invaluable assistance during the experimental portion of this investigation; his humor, together with his friendship, have made this research rewarding.

Gratitude is also expressed to Professor E. F. W. Seymour of the University of Warwick, England, for informal discussions concerning this work, and critical reading of the manuscript.

It is also a pleasure to thank Mr. B. J. Beaudry and Dr. D. T. Peterson of the Metallurgy Division of the Ames Laboratory for the preparation and analysis of the hydride samples used in this study.

IX. APPENDIX

The spark source mass spectrometric analyses for various lanthanum and yttrium metals used in this investigation are presented here. They are listed in Tables A-1 through A-7.

Table A-1. Spark source mass spectrometric analysis for Ames Laboratory La-112078 which was used to prepare $LaH_{1.80}$ sample

ANALYSIS (ATOMIC PPM)

SPARK SOURCE MASS SPECTROMETRIC ANALYSIS- ID: LA-~~102877~~ 112078

MAJOR ELEMENT: LA

LI	.001	BE	<.002	B	<.07	NA	<1	MG	<.1	AL	.30	SI	<2	P	<.003
S	<.04	CL	10	K	<.1	CA	.60	TI	<.1	V	<.02	CR	<.2	MN	<.01
FE	2	CO	.10	NI	.60	CU	1.8	ZN	<.08	GA	<.08	GE	<.07	AS	<.02
SE	<.02	BR	<.04	RB	<.008	SR	<.02	ZR	<.2	NB	<.1	MO	<1	RU	<.3
RH	<.07	PD	<.01	AG	<.03	CD	<.08	IN	<.03	SN	<.08	SB	<.04	TE	<.07
I	<.04	CS	<.09	BA	<3	HF	<.8	TA	2	W	<2	RE	<1	OS	<1
IR	<.4	PT	<.6	AU	<.1	HG	<.1	TL	<.08	PB	<.2	BI	<.06	TH	<.7
														U	<.3

RARE EARTH IMPURITIES

SC	1	Y	.06	LA		CE	1	PR	.20	ND	<.8	SM	<.2	EU	<.1
GD	<.6	TB	<.2	DY	<.3	HO	<.2	ER	.57	TM	<.08	YB	<.1	LU	<.3

REMARKS: SEMIQUANTITATIVE SURVEY

Vacuum Fusion Results – Wt. ppm in ( )

O	321 (37)	N	158 (16	H	550 (4)		
Combustion				Absorption			
C	92 (8)			F	180 (26)	Fe	4 (1.7

Table A-2. Spark source mass spectrometric analysis for Ames Laboratory La-8679 which was used to prepare $LaH_{2.00}$ and $LaH_{2.38}$ samples

ANALYSIS (ATOMIC PPM)

SPARK SOURCE MASS SPECTROMETRIC ANALYSIS- ID: LA-8679

MAJOR ELEMENT: LA

LI	<.003	BE	<.004	B	.2	NA	<.1	MG	<.2	AL	.50	SI	1.0	P	<.04
S	<.4	CL	3	K	<.2	CA	1.8	TI	<.2	V	<.03	CR	<.3	MN	<.02
FE	10	CO	<.2	NI	2.0	CU	10	ZN	<.1	GA	<.1	GE	<.1	AS	<.02
SE	<.2	BR	<.04	RB	<.01	SR	<.03	ZR	<.5	NB	<3	MO	<.8	RU	<.4
RH	<.08	PD	<.2	AG	<.03	CD	<.06	IN	<.03	SN	<.1	SB	<.05	TE	<.04
I	<.1	CS	<.1	BA	<1	HF	<.9	TA	3.4	W	<1	RE	<.7	OS	<.9
IR	<.3	PT	<.3	AU	<.07	HG	.30	TL	<.06	PB	.40	BI	<.04	TH	<.5
														U	<.2

RARE EARTH IMPURITIES

SC	1.0	Y	1.4	LA		CE	<2	PR	<2	ND	<1	SM	<.8	EU	<.8
GD	<7	TB	.30	DY	.8	HO	<.2	ER	<.6	TM	<.1	YB	<.3	LU	<.5

REMARKS:

Vacuum Fusion Results - Wt. ppm in ( )

O	295 (34)	N	30 (3)	H	225 (2)		
Combustion				Absorption			
C	128 (11)			F	146 (20)	Fe	5 (2.0)

Table A-3. Spark source mass spectrometric analysis for Ames Laboratory La-102877 which had been used in preparing $LaH_{2.15}$, $LaH_{2.27}$ and $LaH_{2.46}$ samples

ANALYSIS (ATOMIC PPM)

SPARK SOURCE MASS SPECTROMETRIC ANALYSIS - ID: LA-102877

MAJOR ELEMENT: LA

LI	.001	BE	<.002	B	<.07	NA	<1	MG	<.1	AL	.30	SI	<2	P	<.003
S	<.04	CL	10	K	<.1	CA	.60	TI	<.1	V	<.02	CR	<.2	MN	<.01
FE	2	CO	.10	NI	.60	CU	1.8	ZN	<.03	GA	<.08	GE	<.07	AS	<.02
SE	<.02	BR	<.04	RB	<.008	SR	<.02	ZR	<.2	NB	<.1	MO	<1	RU	<.3
RH	<.07	PD	<.01	AG	<.03	CD	<.08	IN	<.03	SN	<.08	SB	<.04	TE	<.07
I	<.04	CS	<.09	BA	<3	HF	<.8	TA	2	W	<2	RE	<1	OS	<1
IR	<.4	PT	<.6	AU	<.1	HG	<.1	TL	<.08	PB	<.2	BI	<.06	TH	<.7
														U	<.3

RARE EARTH IMPURITIES

SC	1	Y	.06	LA		CE	1	PR	.20	ND	<.8	SM	<.2	EU	<.1
GD	<.6	TB	<.2	DY	<.3	HO	<.2	ER	.57	TM	<.08	YB	<.1	LU	<.3

REMARKS: SEMIQUANTITATIVE SURVEY

Vacuum Fusion Results - Wt. ppm in ( )

O	304 (35)	N	545 (55)	H	412 (3)

Combustion		Absorption			
C	92 (8)	F	180 (25)	Fe	4 (1.7)

Table A-4. Spark source mass spectrometric analysis for Ames Laboratory Y-12979-W which had been used in preparing $YH_{1.81}$, $YH_{1.91}$, $YH_{2.03}$ and $YH_{1.98}$ (old) samples

ANALYSIS (ATOMIC PPM)

SPARK SOURCE MASS SPECTROMETRIC ANALYSIS — ID: Y-12979-W								
MAJOR ELEMENT: Y								
LI .005	BE <.002	B <.08	NA <.1	MG <.04	AL 6	SI 1	P <.05	
S .5	CL 2	K <.09	CA .10	TI 2.1	V <.2	CR 1	MN .10	
FE 15	CO <.2	NI 2	CU 4	ZN .29	GA <.05	GE <.05	AS <.01	
SE <.1	BR <.04	RB <.009	SR <1	ZR <2	NB <.1	MO <.5	RU <.6	
RH <.3	PD <1	AG <.03	CD <.06	IN <.03	SN .70	SB <.04	TE <.05	
I <.04	CS <.003	BA <.07	HF <2	TA 2	W 40	RE <.3	OS <.5	
IR <.2	PT <.3	AU <.05	HG <.06	TL <.04	PB 1	BI <.03	TH <.4	
							U <.2	
RARE EARTH IMPURITIES								
SC <.1	Y	LA 1.5	CE 2.4	PR .52	ND <.5	SM <.3	EU <.1	
GD <20	TB 1	DY <.6	HO <.1	ER <.4	TM <.1	YB <4	LU 2	
REMARKS: SEMI QUANTITATIVE SURVEY								
INSTRUMENT MEMORY FOR GD AND DY.								

Vacuum Fusion Results - Wt. ppm in ( )

O	411 (64)	N	25 (4)	H	880 (10)		
Combustion				Absorption			
C	282 (38)	F	98 (21)	Fe	17 (11)		

Table A-5. Spark source mass spectrometric analysis for Ames Laboratory Y-12381B which had been used for preparing new "purest" $YH_{1.98}$ and $Y_{1-x}(RE)_xH_{1.98}$ samples with RE = Ce, Nd, Gd, Dy and Er.

ANALYSIS (ATOMIC PPM)

SPARK SOURCE MASS SPECTROMETRIC ANALYSIS - ID: Y-12381B

MAJOR ELEMENT: Y

LI	<.000	BE	<.002	B	.07	NA	<.1	MG	.10	AL	3	SI 3	P	<.03
S	<.1	CL	3	K	<.04	CA	.10	TI	.80	V	<.03	CR .5	MN	<.04
FE	10	CO	<.05	NI	3	CU	5	ZN	<.06	GA	<.06	GE <.08	AS	<.02
SE	<.1	BR	<.05	RB	<2000	SR	<.1	ZR	<.3	NB	<.8	MO <.8	RU	<.6
RH	<.1	PD	<.3	AG	<.04	CD	<.08	IN	<.03	SN	<.1	SB <.05	TE	<.06
I	<.04	CS	<.004	BA	<.08	HF	<.8	TA	<.6	W	20	RE <.4	OS	<.2
IR	<.09	PT	<.3	AU	<.07	HG	<.08	TL	<.06	PB	20	BI <.04	TH	<.5
													U	<.2

RARE EARTH IMPURITIES

SC	K1	Y		LA	3	CE	2	PR	4.0	ND	<.6	SM <.4	EU	<.2
GD	2.1	TB	4.5	DY	<.4	HO	<.2	ER	<.5	TM	<.1	YB <.3	LU	<.3

REMARKS: Semiquantitative Survey

Vacuum Fusion Results - Wt. ppm in ( )

O	834 (150)	N	25 (4)	H	704 (8)		
Combustion				Absorption			
C	141 (19)			F	<14 (<3)	Fe	8 (4.9)

Table A-6. Spark source mass spectrometric analysis for Ames Laboratory La-72280 which was used in preparing "pure" $LaH_{2.26}$ and $La_{1-x}Ce_xH_{2.25}$ samples

ANALYSIS (ATOMIC PPM)

SPARK SOURCE MASS SPECTROMETRIC ANALYSIS- ID: LA-72280

MAJOR ELEMENT: LA

LI	.02	BE	<.005	B	.1	NA	≤.5	MG	≤1	AL	≤.0	SI	≤3	P	<.2
S	<1	CL	4	K	<1	CA	<.3	TI	<.3	V	<.1	CR	2.0	MN	.20
FE	80	CO	<.03	NI	<1	CU	7.0	ZN	<.07	GA	<.1	GE	.16	AS	<.03
SE	<.05	BR	<.03	RB	<.007	SR	<.02	ZR	<.2	NB	<10	MO	<.5	RU	<.2
RH	<.06	PD	<.1	AG	<.03	CD	<.04	IN	<.02	SN	<.09	SB	<.04	TE	<.05
I	<.03	CS	<20	BA	<3	HF	<.6	TA	<.07	W	<1	RE	<.4	OS	<.5
IR	<.2	PT	.60	AU	<.05	HG	<.06	TL	<.04	PB	<.1	BI	<.03	TH	<.4
														U	<.1

RARE EARTH IMPURITIES

SC	<.09	Y	2	LA		CE	10	PR	1.0	ND	2.2	SM	<.1	EU	<.1
GD	15	TB	1.0	DY	<.5	HO	<.2	ER	<.4	TM	<.1	YB	<.08	LU	<.2

REMARKS: Semiquantitative Survey

Vacuum Fusion Results - Wt. ppm in ( )

O	573 (66)	N	89 (9)	H	1237 (9)

Combustion		Absorption			
C	139 (12)	F	102 (14)	Fe	9.4 (3.8)

Table A-7. Spark source mass spectrometric analysis for Ames Laboratory La-8681 which had been used in preparing "pure" $LaH_{2.27}$ and $La_{1-x}Gd_xH_{2.25}$ samples

ANALYSIS (ATOMIC PPM)

SPARK SOURCE MASS SPECTROMETRIC ANALYSIS - ID: LA-8681

MAJOR ELEMENT: LA

LI	.005	BE	<.001	B	.2	NA	<1	MG	<.05	AL	5	SI	30	P	.08
S	<.5	CL	4	K	<.3	CA	<.4	TI	.21	V	.56	CR	<.03	MN	<.02
FE	2	CO	<.06	NI	2.8	CU	<.06	ZN	<.03	GA	<.1	GE	<.06	AS	<.2
SE	<.04	BR	<.03	RB	<.006	SR	<.02	ZR	<.2	NB	<2	MO	<.4	RU	<.06
RH	<.06	PD	<.1	AG	<.02	CD	<.05	IN	<.03	SN	<.08	SB	<.03	TE	<.05
I	<.03	CS	<.1	BA	<.8	HF	<.7	TA	1.9	W	<1	RE	<.4	OS	<.5
IR	<.2	PT	.31	AU	<.06	HG	.20	TL	<.04	PB	.20	BI	<.03	TH	<.4
														U	<.2

RARE EARTH IMPURITIES

SC	<.02	Y	3.1	LA		CE	4	PR	1	ND	<1	SM	<.4	EU	<.2
GD	<.5	TB	<.1	DY	<.5	HO	<.2	ER	<.5	TM	<.1	YB	<.2	LU	<.3

REMARKS: Semiquantitative survey

Vacuum Fusion Results - Wt. ppm in ( )

O	243 (25)	N	59 (4)	H	137 (1)

Combustion		Absorption			
C	23 (2)	F	65 (9)	Fe	9 (3.9)